

Thermal Properties of Dysprosium-Titanate in the Spin Ice State

vorgelegt von
Diplom-Physiker
Bastian Klemke
aus Berlin

von der Fakultät II - Mathematik und Naturwissenschaften
der Technischen Universität Berlin
zur Erlangung des akademischen Grades

Doktor der Naturwissenschaften
Dr. rer. nat.

genehmigte Dissertation

Promotionsausschuss:

Vorsitzender: Prof. Dr. M. Dähne
Gutachter: Prof. Dr. D. A. Tennant
Gutachter: Prof. Dr. M. Meißner
Gutachter: Prof. Dr. J. P. Goff

Tag der wissenschaftlichen Aussprache: 21.01.2011

Berlin 2011
D 83

Thermal Properties of Dysprosium-Titanate in the Spin Ice State

Bastian Klemke

Abstract

Seit mehr als zehn Jahren dient das Seltene-Erden-Titanat $\text{Dy}_2\text{Ti}_2\text{O}_7$ als Beispiel für ein geometrisch frustriertes Spin-System (“Spin-Eis”) und ist Gegenstand intensiver Untersuchungen gewesen. Im Jahr 2008 haben C. Castelnovo et al. (*Nature* **451**, 42, 2008) die Existenz von magnetischen Quasiteilchen in Spin-Eis-Materialien wie $\text{Dy}_2\text{Ti}_2\text{O}_7$ postuliert. Diese durch die Dysprosium-Ionen Dy^{3+} verursachten magnetischen Anregungen haben die Eigenschaften von magnetischen Monopolen. In einer Reihe von Experimenten wurden mit den Methoden der Neutronenbeugung und der Myonen-Spin-Rotation an einkristallinem $\text{Dy}_2\text{Ti}_2\text{O}_7$ und $\text{Ho}_2\text{Ti}_2\text{O}_7$ im Jahr 2009 erste experimentelle Hinweise auf die Existenz von magnetischen Monopolen in Spin-Eis gefunden. Im Rahmen dieser Arbeit wurde ein Neutronenstreuexperiment durchgeführt, mit dem die Linien, die entgegengesetzte Monopolladungen verbinden (“Dirac-String”), erstmalig nachgewiesen werden konnten.

Der Hauptaspekt in dieser Arbeit liegt jedoch auf der Charakterisierung der thermischen Eigenschaften von $\text{Dy}_2\text{Ti}_2\text{O}_7$: Die spezifische Wärmekapazität, die Wärmeleitfähigkeit und die Temperaturleitfähigkeit wurden im Temperaturbereich von 0.3 K bis 30 K und magnetischen Feldern bis zu 1.5 T gemessen.

Seit Beginn der Untersuchungen an $\text{Dy}_2\text{Ti}_2\text{O}_7$ wurden zahlreiche Messungen der spezifischen Wärmekapazität veröffentlicht. Allerdings zeigen diese bei tiefen Temperaturen ($T < 1$ K) erhebliche Abweichungen voneinander. Daher führten wir neue Messungen der spezifischen Wärmekapazität im Temperaturbereich von 0.3 K bis 30 K mit besonderem Augenmerk auf den Tieftemperaturbereich durch. Es zeigte sich, dass für $T < 1$ K die Auswertung der gemessenen Temperatur-Zeit-Profile nicht mit den bisher bekannten Auswertalgorithmen möglich war. Daher adaptierten wir die von P. Strehlow 1994 entwickelte thermodynamische Feldtheorie, mit der schon erfolgreich thermische Relaxationen in Gläsern bei tiefen Temperaturen beschrieben wurden. Unter der Annahme, dass die Gitter-Phononen in $\text{Dy}_2\text{Ti}_2\text{O}_7$ mit einer Vielzahl von magnetischen Systemen wechselwirken, gelang es, die Temperatur-Zeit-Profile exakt zu beschreiben. Auf Grund der Frustration der Spinbewegungen im Spin-Eis-Zustand thermalisieren die magnetischen Systeme (Monopole) bei tiefen Temperaturen nur sehr langsam, wobei Relaxationszeiten bis zu 100 s nachgewiesen werden konnten. Die zwei identifizierten magnetischen Wärmekapazitäten, c_α und c_β , mit Relaxationszeiten $\tau_\alpha \approx 100$ s und $\tau_\beta \approx 5$ s stimmen mit vorherigen Messungen und Monte-Carlo-Simulationen überein. Mit der Methode der thermodynamischen Feldtheorie wurden c_α und c_β jedoch erstmalig direkt nachgewiesen.

Des Weiteren wurden erstmals Messungen der Wärmeleitfähigkeit im Temperaturbereich von 0.3 K bis 30 K an einem $\text{Dy}_2\text{Ti}_2\text{O}_7$ Einkristall durchgeführt. Diese Messungen ergaben, dass allein Wärmetransport durch Phononen, aber kein Transport über die magnetischen Systeme stattfindet. Wir konnten nachweisen, dass im Temperaturbereich von 0.3 K bis 3 K schnell relaxierende magnetische Systeme ($\tau_\gamma \approx 10^{-8}$ s) die Phononen resonant streuen. Diese γ -Systeme wurden insbesondere in abschließenden Wärmepulsexperimenten identifiziert, da die Temperaturprofile $\tilde{T}(x, t = 10^{-4} \text{ s} \dots 10^3 \text{ s})$ mit der thermodynamischen Feldtheorie exakt beschrieben werden konnten.

Thermal Properties of Dysprosium-Titanate in the Spin Ice State

Bastian Klemke

Abstract

For more than a decade, the rare earth titanate $\text{Dy}_2\text{Ti}_2\text{O}_7$ has attracted much interest as a model material for geometrically frustrated spin systems (“spin ice”) and was topic of intensive research. In 2008, C. Castelnovo et al. (*Nature* **451**, 42, 2008) proposed the existence of magnetic quasiparticles in spin ice materials like $\text{Dy}_2\text{Ti}_2\text{O}_7$. These magnetic excitation caused by the dysprosium ions Dy^{3+} have the properties of magnetic monopoles. In a series of neutron scattering and muon spin rotation experiments on single crystalline $\text{Dy}_2\text{Ti}_2\text{O}_7$ and $\text{Ho}_2\text{Ti}_2\text{O}_7$, respectively, signatures of magnetic monopoles in spin ice have been reported in the year 2009. Within this work a neutron scattering experiment was performed and the strings which connects the opposite monopole charges (“Dirac strings”) were detected for the first time.

However, this thesis focusses mainly on the characterization of the thermal properties on $\text{Dy}_2\text{Ti}_2\text{O}_7$: The specific heat, the thermal conductivity and the thermal diffusivity were measured in the temperature range from 0.3 K to 30 K and magnetic fields up to 1.5 T.

Since the early studies there were published several measurements on the specific heat of $\text{Dy}_2\text{Ti}_2\text{O}_7$. However, at low temperatures ($T < 1$ K) they exhibit obvious differences. Thus we have performed new measurements on the specific heat in the temperature range from 0.3 K to 30 K in particular at low temperatures. For $T < 1$ K, the analysis of the measured temperature-time-profiles was not successful with the so far known methods. Therefore, we have adapted the thermodynamic field theory, which was developed by P. Strehlow in 1994 and which was approved by describing the thermal relaxation in glasses at low temperature. Assuming that the lattice phonons in $\text{Dy}_2\text{Ti}_2\text{O}_7$ interact with a multitude of magnetic systems, we can precisely describe the temperature-time-profiles. Due to the frustration of the spin movement in the spin ice phase at low temperatures the magnetic systems (monopoles) thermalize very slow, whereat relaxation times up to 100 s were observed. The two identified magnetic heat capacities, c_α and c_β , which have relaxation times $\tau_\alpha \approx 100$ s and $\tau_\beta \approx 5$ s are in agreement with previously published measurements and Monte-Carlo simulations. However, with the analysis according to thermodynamic field theory c_α and c_β were verified directly for the first time.

Furthermore, the thermal conductivity of a $\text{Dy}_2\text{Ti}_2\text{O}_7$ single crystal was measured in the temperature range from 0.3 K to 30 K for the first time. These measurements exhibits that solely the phonons but not the magnetic systems are transporting the heat. We were able to demonstrate that the fast relaxing magnetic systems ($\tau_\gamma \approx 10^{-8}$ s) scatter the phonons resonantly. Finally, these γ -systems have been identified in heat pulse experiments in particular, since the temperature profiles $\tilde{T}(x, t = 10^{-4} \text{ s} \dots 10^3 \text{ s})$ were accurately described by the thermodynamic field theory.

Contents

1	Introduction	3
2	Frustrated Spin Systems	7
2.1	Magnetic frustration	7
2.2	Geometric frustration in spin ice systems	8
2.3	Zero point entropy	12
2.4	Monopole-like excitations in spin ice	14
2.4.1	Signature of magnetic monopoles in specific heat measurements	18
2.4.2	Signature of Dirac strings in neutron scattering experiments	19
3	Recent Magnetic Monopole Studies Using Scattering Techniques	22
3.1	Neutron measurements at HZB	22
3.1.1	Neutrons and flat cone technique	22
3.1.2	Experimental set up for E2	23
3.1.3	Results of neutron measurements at HZB	25
3.2	Recent results from other research groups	32
4	Thermal Transport and Relaxation in Dielectric Crystals	36
4.1	Basic concepts of thermal measurements	36
4.2	Thermodynamic Field Theory (TFT)	39
5	Measurements of Thermal Properties based on TFT Concept	45
5.1	Measurement of specific heat	49
5.1.1	Set-up and data evaluation	49
5.1.2	Results on specific heat	54
5.2	Measurement of thermal conductivity	59
5.2.1	Set-up and data evaluation	59

5.2.2	Results on thermal conductivity	61
5.3	Measurement of heat pulse transport	63
6	Discussion of Results and Comparison to Magnetic Models	68
6.1	Heat capacity at $T = 0.3 - 30$ K and $B = 0 - 1.5$ T	69
6.1.1	Paramagnetic spin contribution from α -excitations	71
6.1.2	Schottky-type spin contribution from β -excitations	74
6.1.3	Thermal relaxation times τ_{α}^R and τ_{β}^R ($T < 1$ K, $B < 0.5$ T)	75
6.1.4	Fast-relaxing magnetic specific heat ($T < 1$ K, $B < 0.5$ T)	80
6.1.5	Heat capacity in the magnetic ordered phase ($B \geq 0.5$ T)	82
6.2	Thermal conductivity at $T = 0.3 - 30$ K and $B = 0 - 1.5$ T	85
6.2.1	Phonon scattering theory of $\text{Dy}_2\text{Ti}_2\text{O}_7$ lattice	86
6.2.2	Scattering by magnetic excitations	87
7	Conclusion and Summary	91
	Bibliography	93
	List of Figures	101
	List of Tables	103

Chapter 1

Introduction

For more than a decade, the dipolar spin ice compound $\text{Dy}_2\text{Ti}_2\text{O}_7$ has attracted much interest as a model material for geometrically frustrated spin systems. Forming a pyrochlore lattice of cubic symmetry, the strong magnetic moments of the rare-earth ion Dy^{3+} occupy a 3-dimensional network of corner sharing tetrahedra. Among the four dysprosium spins in a tetrahedron the ferromagnetic nearest neighbour interactions force geometrical frustration: each spin is aligned parallel to the local $[111]$ axes, however, two spins point inward and two spins outward on each tetrahedron. This is called the “2-in & 2-out” rule or – in analogy to the disordered protons in hexagonal water ice – the “spin ice” state [Har97].

In 2008, Castelnovo et al. [Cas08] proposed the existence of magnetic quasiparticles in spin ice materials like $\text{Dy}_2\text{Ti}_2\text{O}_7$: in the constraint of a “2-in & 2-out” situation, the flipping of one spin breaks the constraint leaving neighbouring tetrahedra with “1-in & 3-out” and “3-in & 1-out” which constitute a pair of topological defects. Continuation of the spin flips over consecutive tetrahedra separates the defects and creates a string of dipoles with a monopole and an anti-monopole at its ends. In a series of neutron scattering and muon spectroscopy experiments on $\text{Dy}_2\text{Ti}_2\text{O}_7$ and $\text{Ho}_2\text{Ti}_2\text{O}_7$, respectively, signatures of magnetic monopoles have been reported: the density and orientation of Dirac strings by diffuse neutron scattering [Mor09], the existence of a magnetic Coulomb phase by polarized neutron scattering [Fen09] and by muon spin rotation [Bra09]. From these experimental results it was proposed that magnetic charges exist in a spin ice material and that they interact by Coulomb’s law.

The magnetic heat capacity $C(T)$ of a gas of weakly interacting monopoles has been calculated using the Debye-Hückel theory [Mor09]. This theory is appropriate to low temperatures where the monopoles are sparse: below 0.6 K, it captures a dramatic decrease of $C(T) \propto T^{\approx 10}$. To our first set of specific heat measurements [Czt08] the model calculation (using no fitting parameters) yielded fair agreement where in the temperature range from 0.6 K to 0.3 K the heat capacity diminished by three orders of magnitude. At higher temperatures, $T \gtrsim 1$ K, spin ice turns into a more conventional paramagnet and the monopole description breaks down.

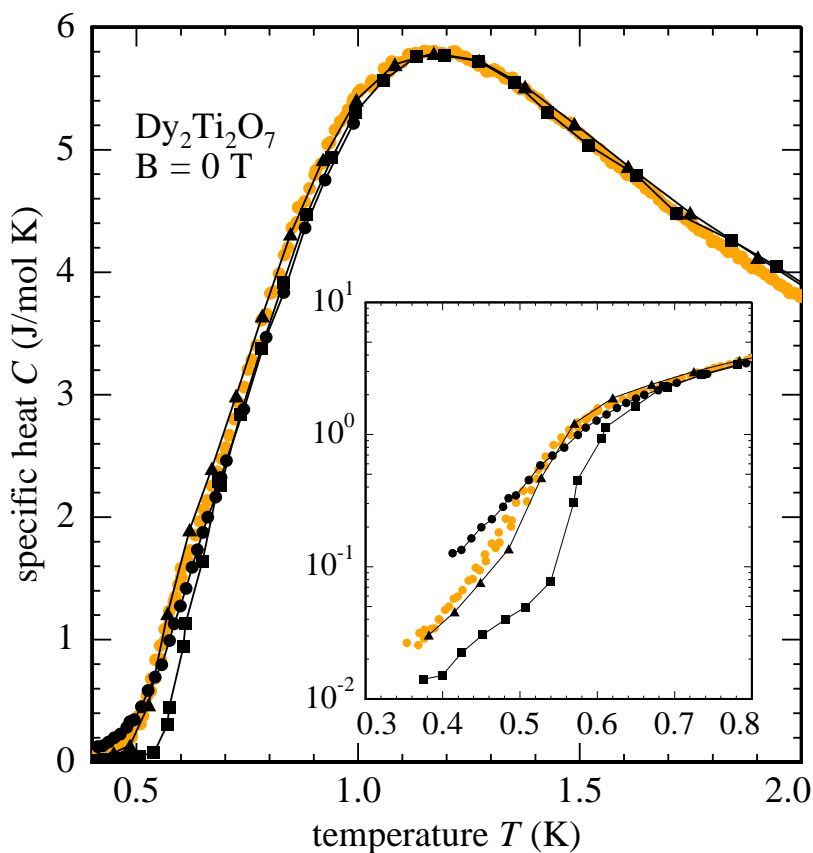


Figure 1.1: Specific heat of $\text{Dy}_2\text{Ti}_2\text{O}_7$ in the spin ice state (at zero magnetic field) as published by various research groups: full squares (Higashinaka et al. [Hig02]), full triangles (Hiroi et al. [Hir03]), full circles (Kadowaki et al. [Kad09]) and full orange circles (Morris et al. [Mor09]). For temperatures $T \gtrsim 0.7$ K all specific heat data agree by $\Delta C/C = \pm 5\%$. The inset displays the same data on a half logarithmic scale: Below 0.7 K, differences in the published specific heat values vary by almost up to one order of magnitude (see text).

Since the early studies on the spin ice problem, bulk measurements such as the heat capacity of $\text{Dy}_2\text{Ti}_2\text{O}_7$ (as shown in figure 1.1) have revealed the various spin states in

this frustrated material with respect to temperature and to magnetic field parallel to the main crystallographic directions. In combination with Monte Carlo calculations [Yos04; Mel04; Ruf05], the different spin phases have been identified in the paramagnetic regime, $T > 1$ K, and in the spin ice phase, $T < 1$ K, with respect to magnetic field below and above 0.5 T [Mat02; Hig02; Hir03; Kad09]. However, in the diluted monopole regime, $T < 0.6$ K and $B \approx 0$ T (where magnetic field misalignment to crystallographic axis and demagnetization effects due to sample geometry can be excluded), the published data on $C(T, B)$ of $\text{Dy}_2\text{Ti}_2\text{O}_7$ exhibit obvious differences from those we have measured and published [Mor09] (see figure 1.1). Whereas for $T > 0.6$ K all data fairly agree by ± 5 %, at the lowest temperature, around 0.4 K, our data deviate by +50 % to -200 % from specific heat data by Kadowaki et al. and by Hiroi et al., respectively.

These discrepancies in the magnitude of the magnetic heat capacity measured in the spin ice regime at zero magnetic field, forced us to re-evaluate our thermal measurement techniques and theoretical analysis of the basic temperature responses as described later. Having a closer look on the experimental data (i. e. the temperature profiles), we see deviations from the common behaviour one would expect while measuring the specific heat. Also, in magnetic field measurements up to 1.5 T, these deviations below 1 K remained to be the dominant behaviour. With respect to the strong variation of the specific heat in the spin ice regime and the spin-ordered phase at low and high fields, respectively, we argued that this phenomenon is characteristic for the $\text{Dy}_2\text{Ti}_2\text{O}_7$ sample itself and should not originate from the calorimeter parameters. Given this argument, we were forced to analyse the experimental raw data on the basis of a thermal transport theory. With respect to the thermal boundary conditions of the calorimeter set-up, the temperature profiles have been analysed according to solutions of a set differential equations based on thermodynamic field theory (TFT) [Str94; Str97; Mei04]. Under the assumption that heat is propagated by phonon transport and that the phonons interact with a multitude of magnetic subsystems, using thermodynamic field theory analysis we can reproduce the non-exponential temperature profiles and subsequently calculate the underlying magnetic heat contributions. With this thermodynamic model, we find – on long time-scale – two different magnetic excitations, c_α and c_β , which thermally couple to the phonon bath with characteristic relaxation times $\tau_\alpha \approx 100$ s and $\tau_\beta \approx 5$ s. For the relaxation time of the α - and β -excitations we find a temperature variation down to 0.35 K very similar to the findings of Snyder et al. [Sny04] where the characteristic spin

relaxation time below 1 K was observed to rise sharply from the ms-range up to 1 s (at 0.8 K).

On a much shorter time-scale, below our experimental resolution of approximately 0.1 s for the recording of the temperature profile, we can identify a fast coupling, third magnetic excitation c_γ which we believe to interact directly with the propagating phonons according to a resonant phonon scattering process. This assumption is strongly supported by our measurements on the thermal conductivity $\kappa(T, B)$ of $\text{Dy}_2\text{Ti}_2\text{O}_7$ in the temperature range from 0.3 K to 30 K and in magnetic field up to 1.5 T. Adjusting the experimental set-up to the appropriate initial and boundary conditions in the thermodynamic field theory, the thermal conductivity has been calculated on the basis of Callaway's relaxation ansatz for phonons [Cal59]. Below 1 K, the γ -excitations dominantly scale the low-temperature thermal conductivity exhibiting a small plateau-like region around 0.5 K. This plateau in $\kappa(T)$ is weakly dependent on the magnetic field: with increasing magnetic field the number density of resonant magnetic excitations decreases (about linearly with field). It should be noted that above 1 K the thermal conductivity does not depend on the magnetic field. In addition to the stationary heat flow experiment (and complementary analysis according to the thermodynamic field theory) we also have studied the non-stationary transport case, i. e. heat pulse propagation and heat diffusive transport. Again, adjusting the experimental initial and boundary conditions to our TFT model, we were able to reproduce the measured temperature profiles $\tilde{T}(x, t)$ on the basis of the heat capacity data and the thermal conductivity data without additional parameters. Thus, all three thermal experiments can be described by the thermodynamic field theory where thermal phonons transport heat and the interaction with relaxation processes command the evolution of temperature in a $\text{Dy}_2\text{Ti}_2\text{O}_7$ sample below 1 K.

Chapter 2

Frustrated Spin Systems

This chapter contains an overview of the main aspects of frustrated spin systems. It starts with a brief discussion of the historic problem of water ice and its relation to spin ice systems. It follows a description of the important properties of geometric frustrated spin ice systems. At the end of this chapter it will be discussed how monopole-like excitations can be identified in spin ice systems.

2.1 Magnetic frustration

Frustration is defined as the competition between the next neighbour interactions in an atomic system such that not all of them can be minimized simultaneously, due to local constraints. To depict this, let us have a look to a triangular spin lattice (see figure 2.1a) as an example for geometrical frustration. In such systems, frustration arises without disorder, only from the incompatibility of local interactions with global symmetry imposed by the crystalline lattice structure. Assuming, that two spins can only point either in the same direction (parallel) or in opposite direction (antiparallel) only two magnetic states can be described (Ising model): ferromagnetic order (FM) and antiferromagnetic order (AFM) [Zim72]. If two Ising spins in a triangle arrangement order antiferromagnetically the third spin can only orientate antiparallel to one of the others but not to the other one. Hence, the system is frustrated.

There is of course a similar analogue in three dimensions. Four Ising spins sitting at the edges of a tetrahedron may experience geometric frustration. In contrast to the 2D example we define that the spins are pointing along an axis which connects the corner of the tetrahedron with its centre (“easy axis”, see figure 2.1b). This means each

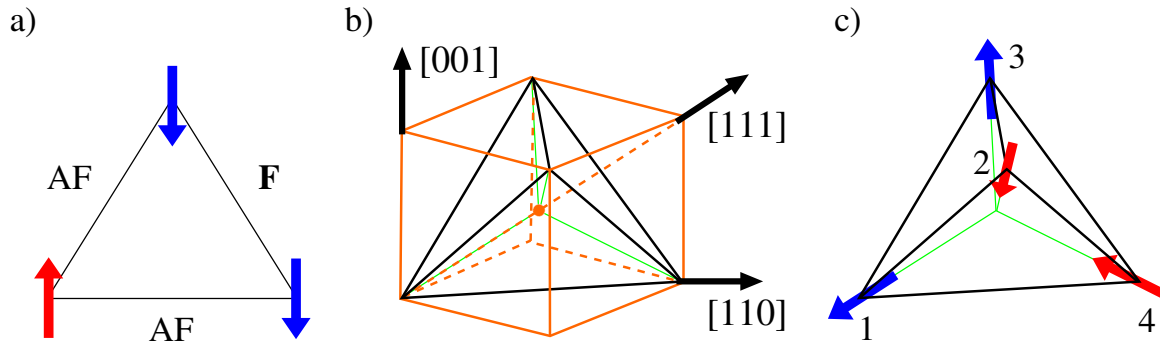


Figure 2.1: (a) Frustrated antiferromagnetic triangular lattice. Two interactions can order antiferromagnetic (AF), the third interaction remains ferromagnetic (F). (b) Tetrahedron in a cubic lattice symmetry. The $[111]$ axis coincides with an easy axis (green line) of the tetrahedron. (c) Frustrated Ising spin ferromagnetic tetrahedron lattice. Four interactions can order ferromagnetic (spins $1 \leftrightarrow 2$, $2 \leftrightarrow 3$, $3 \leftrightarrow 4$ and $4 \leftrightarrow 1$ are parallel) the two residual interactions remain antiferromagnetic (spins $1 \leftrightarrow 3$ and $2 \leftrightarrow 4$ are antiparallel).

spin points either into or out of the tetrahedron. If we consider an antiferromagnetic interaction, a configuration with all four spins pointing into or out of the tetrahedron will result in no frustration. But if there is a ferromagnetic interaction between the Ising spins, than it is not possible to fulfil this rule for all six next neighbour interactions (see figure 2.1c). If four interactions will be ferromagnetic (spins $1 \leftrightarrow 2$, $2 \leftrightarrow 3$, $3 \leftrightarrow 4$ and $4 \leftrightarrow 1$ are parallel) the two residual interactions will remain antiferromagnetic (spins $1 \leftrightarrow 3$ and $2 \leftrightarrow 4$ are antiparallel). A crystal which consists of such frustrated tetrahedrons is called spin ice.

2.2 Geometric frustration in spin ice systems

To get a better understanding of the frustration in spin ice systems, at first we look at the strictly periodical structure of water ice. This structure is made of Hydrogen and Oxygen atoms. The H_2O molecules in the crystal are ordered in such a way, that each oxide ion O^{2-} is surrounded by four other oxide ions. In each of these $\text{O}-\text{O}$ “bonds” one proton is located due to a minimized energy state. The minimum energy position for placing the protons there is not in the middle of the oxide ions. Instead, there are two positions where the protons can be located. These positions are $\pm 15\%$ away from the middle position between the oxide ions ($\text{O}-\text{O}$ distance: 0.276 nm). The constraint of

H₂O molecular integrity therefore leads to the “ice rule” for a ground state configuration (see figure 2.2a): for each oxygen two protons must be in the near position and two in the far position [Ber33]. From an electrostatic point of view the protons would like to be as far apart as possible. The ice rule therefore frustrate the effective proton-proton interaction.

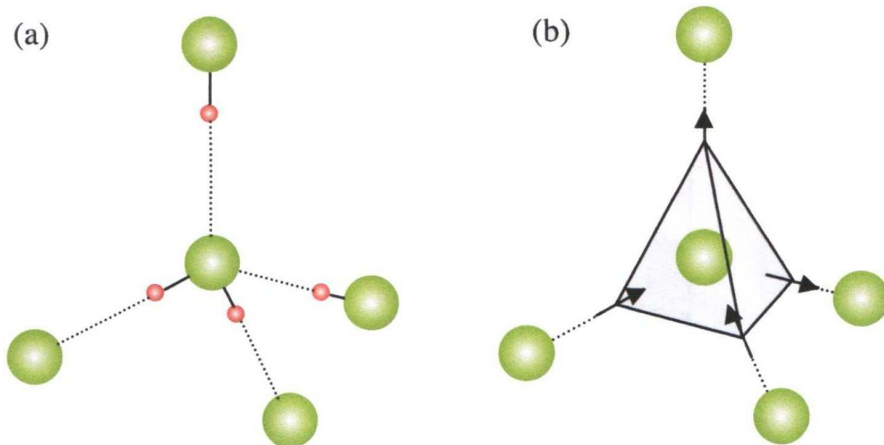


Figure 2.2: Illustration of the equivalence of the water ice rule “two protons near, two protons far” and the spin ice rule “two spins in, two spins out”. Part (a) illustrates a water molecule in the tetrahedral coordination of the spin ice structure (oxides: green, protons: red). In spin ice (b) the rare earth moments (“spins”) occupy the pyrochlore lattice, which is the lattice formed by the mid-points of the bonds of the oxide lattice in cubic ice. (Reproduced from Wiebe et al. [Wie07].)

In the year 1935 Pauling proposed that the tetrahedral structure of water ice affords many equivalent ways of satisfying the ice rules [Pau35]. We assume that we have N oxide ions in one mole of ice. For each $O-O$ bond there are two positions for the protons possible which gives 2^{2N} possible configurations. Out of the 16 possible configurations associated with each oxygen six configurations satisfy the “two protons near, two protons far” condition. An upper bound for the number of ground state configurations is therefore estimated as $\Omega \leq 2^{2N}(6/16)^N = (3/2)^N$.

This gives the following ground state entropy S_0 for water ice:

$$S_0 = k_B \ln \Omega = N_A k_B \ln \left(\frac{3}{2} \right) = 3.37 \frac{\text{J}}{\text{mol K}} \quad . \quad (2.1)$$

The pyrochlore rare earth titanates with the structure $\text{RE}_2\text{Ti}_2\text{O}_7$ (e. g. $\text{Dy}_2\text{Ti}_2\text{O}_7$ or $\text{Ho}_2\text{Ti}_2\text{O}_7$) have an analogous structure to that of water ice, but at this time with the rare earth atoms sitting in the corners of the tetrahedron (see figure 2.2b). The rare

earth sites form what is called a pyrochlore lattice, or a sublattice of corner-shared tetrahedra (see figure 2.3).

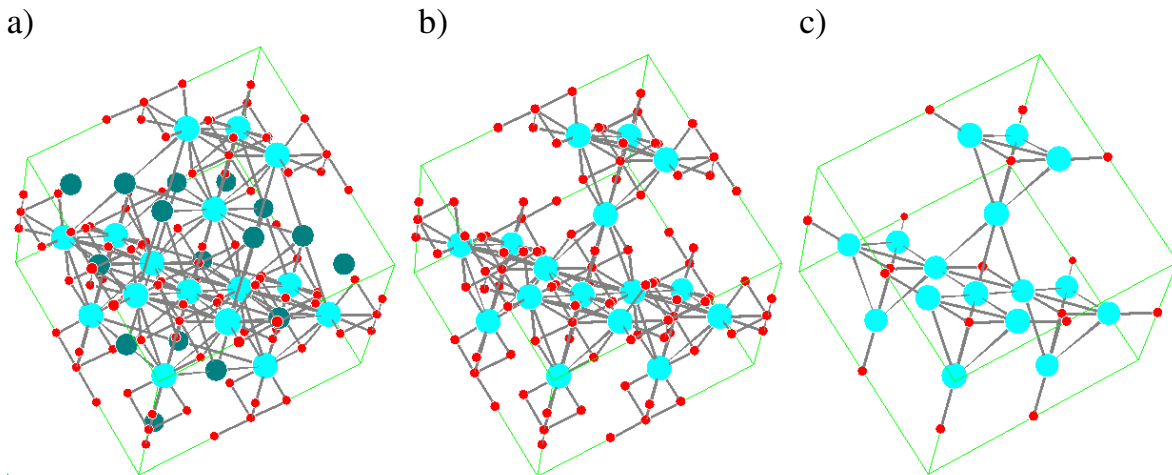


Figure 2.3: Crystal structure of $\text{Dy}_2\text{Ti}_2\text{O}_7$.

(a) Crystal structure of $\text{Dy}_2\text{Ti}_2\text{O}_7$, which contains two interlaced pyrochlore sublattices, one consists of titanium (dark cyan spheres) the other one consists of dysprosium (cyan spheres). The oxygen is represented by the red spheres. Shown is one cubic lattice cell of $\text{Dy}_2\text{Ti}_2\text{O}_7$ (cubic lattice parameter is 1.0123 nm) depicted by the green cube.

(b) Crystal structure of the dysprosium pyrochlore sublattice with the surrounding oxygen ions. The titanium ions are removed

(c) The dysprosium pyrochlore sublattice in spin ice, with the centred oxygen ions. This is a convenient illustration to show the magnetic relevant part of the $\text{Dy}_2\text{Ti}_2\text{O}_7$ structure.

Due to the partially filled atomic shells the rare earth atoms have large magnetic moments (for Dy: $\mu \approx 10\mu_B$). As a result of a very strong single ion anisotropy, the dysprosium spins are forced to point along the easy axes of the tetrahedrons. The two possible directions of these Ising spins are analogous to the directions of the displacement vectors in water ice (see figure 2.2). The spins are correlated, but competing interactions prevent long range order, so the system fluctuates, exploring its many degenerate ground states. Typically, there is some local rule that can be used to construct these ground states. For example, in spin ice the spin orientations have to satisfy the same “2-in & 2-out” rule. And as well there are six possible spin configurations to satisfy this rule. This macroscopically degenerate ground state is characteristic of frustrated systems.

By applying an external magnetic field one can modify the properties of the frustrated system, depending on the orientation of the crystal in the magnetic field. To describe this, we first take a closer look to the crystal structure of the rare earth titanates.

The spin ice materials adopt the cubic pyrochlore structure, space group $Fd\bar{3}m$. This structure consists of 16 rare earth ions, 16 titanium ions (forming another pyrochlore lattice) and 56 oxygen ions (see figure 2.3). The cubic lattice parameter is 1.0123 nm for $Dy_2Ti_2O_7$. One oxygen lies at the centre of each tetrahedron. Therefore each rare earth ion is coordinated by two such oxygen ions that lies along the trigonal axis and thus it is obvious that the Ising spin is pointing along that axis. The coordination shell is then completed by six more oxygen ions at a slightly greater distance from the central ion that form a puckered hexagon with its rotation axis along the local trigonal axis [Bra04].

If we apply a magnetic field along one of the main crystal axis e. g. the $[100]$ direction, the dysprosium spins are neither parallel nor perpendicular to the field, but all spins show equal components along the magnetic field (see figure 2.4a).

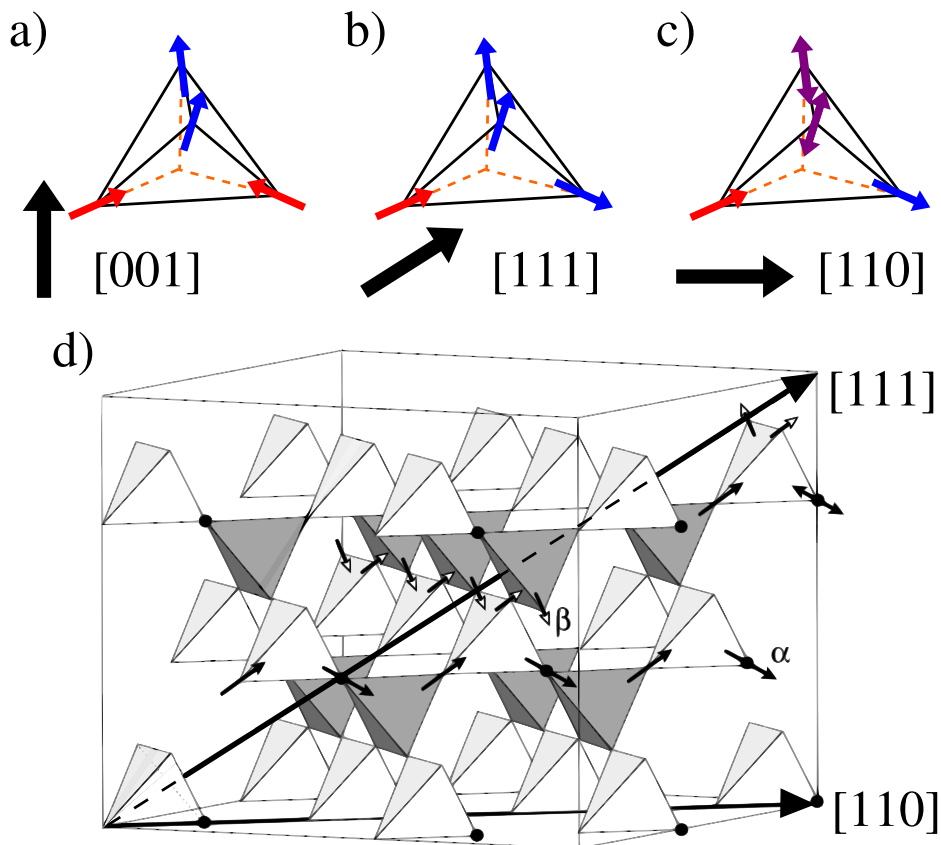


Figure 2.4: Spin configuration of $Dy_2Ti_2O_7$ with the magnetic field along the (a) $[001]$, (b) $[111]$ and (c) $[110]$ axes. For $[111]$ direction the figure depicts the state in which the ice rule breaks (shown as an “1-in & 3-out” configuration). For $[110]$ direction the purple arrows depict the decoupled spins in the β -chain, which are not effected by a $[110]$ magnetic field. (d) Pyrochlore lattice with dysprosium tetrahedrons oriented along $[111]$ and $[110]$ direction. ((d) is reproduced from Ruff et al. [Ruf05])

When the magnetic field is applied along the [111] direction it is parallel to one easy axis in each tetrahedron. Therefore one spin is parallel to the external field (see figure 2.4b). The other three spins have only a small component parallel to the field, which has the same absolute value for these three spins.

If we apply a magnetic field along the [110] direction two spins are orientated orthogonal to the external field and hence have no spin component parallel to the field. The two other spin have an spin component parallel to the field (see figure 2.4c). With a magnetic field parallel to the [110] direction one can separate the whole spin system in two parts. One consisting of the dysprosium ions with a spin component parallel to the field (α -chains), the other one with no component parallel to the field (β -chains) [Hir03]. The experimental outcome of this behaviour will be discussed in more detail in the introduction to chapter 5.

2.3 Zero point entropy

For the first time Ramirez et al. [Ram99] directly investigated the above mentioned non-zero Pauling entropy via experimental measurements of the heat capacity of $\text{Dy}_2\text{Ti}_2\text{O}_7$. In figure 2.5 we show the entropy calculated from the present specific heat measurements, which will be presented in chapter 5. At temperatures below 10 K the specific heat contribution from phonons in $\text{Dy}_2\text{Ti}_2\text{O}_7$ is sufficiently small. This allows to measure the magnetic contribution. The top panel of figure 2.5 shows the magnetic specific heat of $\text{Dy}_2\text{Ti}_2\text{O}_7$ from a temperature $T = 10$ K down to 0.3 K.

One observes a rise of the specific heat upon cooling with a broad maximum around $T_{\text{peak}} \approx 1.2$ K. This growth of the specific heat indicates the build-up of magnetic correlations and removal of magnetic entropy as the system is cooled. The broad maximum and the absence of a sharp feature in $c_{\text{mag}}(T)$ is a strong indication that the system does not develop long range magnetic order via a thermodynamic phase transition. The magnetic specific heat drops rapidly below T_{peak} , essentially vanishing below 0.5 K. This indicates that the spins freeze as the temperature is lowered below T_{peak} and all the thermal spin fluctuations have ceased for $T \ll T_{\text{peak}}$.

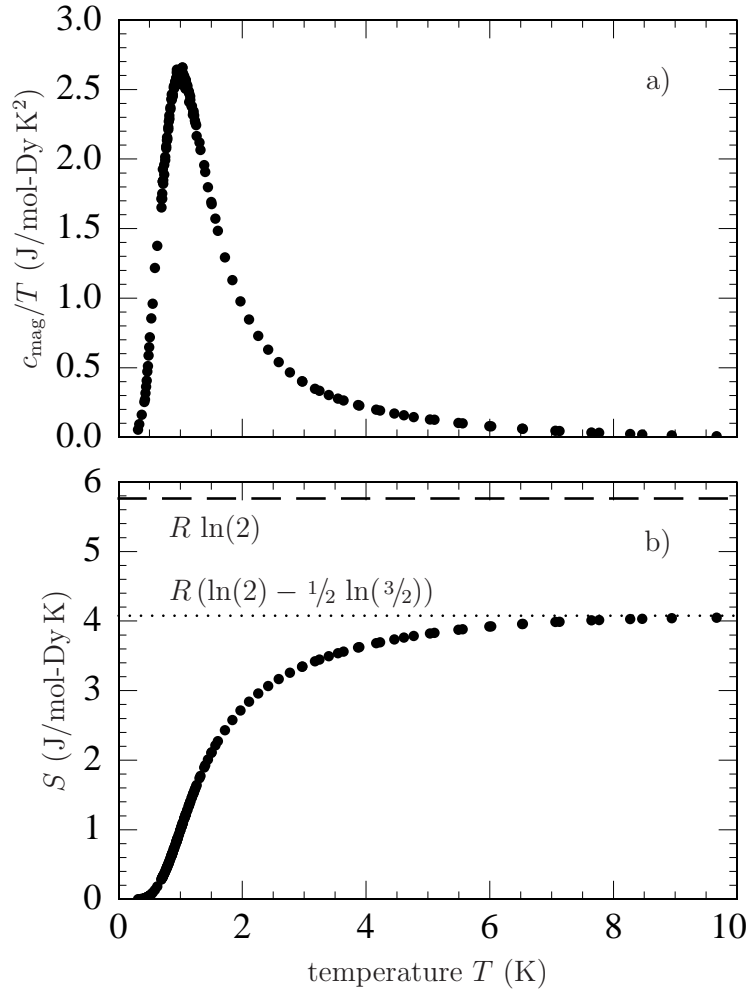


Figure 2.5: Specific heat c_{mag} (a) and entropy S (b) versus temperature at $B = 0$ T. This quantity corresponds to $\delta S(T)$ of equation (2.2) and shows evidence of the Pauling zero point entropy which is characteristic for magnetic frustrated spin ice systems. (Data are taken from specific heat results, which will be presented in chapter 5.)

The entropy removed from the system upon cooling can be determined from the specific heat measurements using the thermodynamic relationship:

$$\delta S(T) \equiv S(T) - S(T_0) = \int_{T_0}^T \frac{c_{\text{mag}}(T')}{T'} dT' \quad , \quad (2.2)$$

where $\delta S(T)$ is the entropy between temperatures T and T_0 . Since there are two possible spin orientations of the Ising spins per degree of freedom, the molar spin entropy in the high temperature regime is $R \ln(2)$. The lower part of figure 2.5 shows the temperature

dependence of δS as temperature is increased from 0.3 K to 10 K. One can read that the entropy recovered upon warming the system is about 4.05 J/mol-Dy K, a value that is considerably less than the value of $R \ln(2) \approx 5.76$ J/mol-Dy K. The difference, 1.71 J/mol-Dy K, is very close to the Pauling estimate for the ground state entropy associated with the extensive ground state degeneracy of spin ice: $S_0 = R/2 \ln(3/2) \approx 1.68$ J/mol-Dy K which includes a factor of 2 to account for the mapping of one mole of water ice onto two moles of spin ice (see (2.1)). This result, which is proofed by several groups [Ram99; Hig03; Hir03], is consistent with the interpretation that the state reached upon cooling down $\text{Dy}_2\text{Ti}_2\text{O}_7$ to $T \approx 0.3$ K carries extensive entropy close to S_0 and obeys the ice rules.

Furthermore spin ice offers a second test of the zero point entropy, unavailable in water ice: the application of a magnetic field should restore long range order. Repeating the experiment in a field, one would expect to recuperate the missing entropy [Har98]. Performing this experiment on a single crystal sample of $\text{Dy}_2\text{Ti}_2\text{O}_7$ this change in behaviour was confirmed by Higashinaka et al. [Hig03].

2.4 Monopole-like excitations in spin ice

The special spin arrangement in the spin ice state of $\text{Dy}_2\text{Ti}_2\text{O}_7$ leads to the theoretical description of “magnetic monopoles in spin ice” which was at first introduced by Castelnovo et al. [Cas08].

A fundamental reason for suggesting the existence of magnetic monopoles was found in 1931 by Paul Dirac [Dir31] when he attempted to reconcile magnetically charged particles with quantum mechanics. Dirac considered a single electron in the field of a magnetic charge and found that for the electron wavefunction to remain single-valued a quantization condition is required. Therefore the elementary electric charge e and magnetic charge q_D should be related by

$$e q_D = n(h/\mu_0) \tag{2.3}$$

where n is an integer, h is Planck’s constant and μ_0 the vacuum permeability. Thus, if even one magnetic charge exists, it would explain the observed quantization of all

electric charges. In Dirac's theory monopoles are assumed to exist in two magnetic charge states, $+q_D$ and $-q_D$, which are antiparticles of one another.

Monopoles may be observable in astronomical phenomena. However, cosmic rays seem to be the most probable source for the terrestrial study of monopoles. It was reported that a magnetic monopole passing through a closed conducting ring would induce a current in that ring [Tas65; VH68] and therefore an experimental proof could be performed. The value of the current would depend only on the magnetic charge and properties of the ring, and would be independent of all other properties of the monopole or its circumstances. Due to the fact that magnetic monopoles can be trapped microscopically on nuclei/atoms/molecules or macroscopically in bulk matter [Got58], there were several attempts to detect these magnetic monopoles in matter, e. g. moon rocks [Ebe71], deep ocean sediment [Fle69] and deeply buried rocks [Kov86] have been investigated.

Blas Cabrera [Cab82] used a 5 cm diameter superconducting ring set-up to detect moving monopoles in cosmic rays. The ring was connected to the superconducting input coil of a SQUID. The passage of a single Dirac charge through the ring would produce an $8\Phi_0$ flux change in the ring-SQUID circuit. An event was recorded with this experimental set-up in February 1982 which was consistent with the passage of a particle with magnetic charge q_D (see figure 2.6).

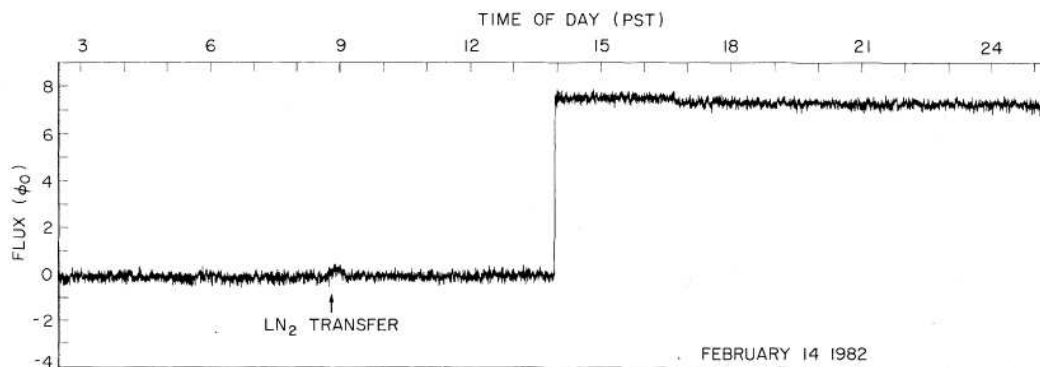


Figure 2.6: Candidate monopole event published by Blas Cabrera in 1982 (reproduced from [Cab82]).

The event is not easily attributable to any other probable cause. However, its possible origin from some internal release of stress in the apparatus cannot be ruled out with absolute certainty. Since then, a second event has not been seen and published.

So, there is no experimental proof of the existence of cosmic magnetic monopoles until today.

However, the special spin arrangement in the spin ice state of $\text{Dy}_2\text{Ti}_2\text{O}_7$ leads to the theoretical description of “magnetic monopoles in spin ice” [Cas08]. These “magnetic monopoles” are not free particles, but quasiparticle excitations in the spin ice material. To explain this, let us have a look to the spin ice ground state. The spins in each tetrahedron fulfil the “2-in & 2-out” ice rule (see figure 2.7a). Another way of describing that ground state is by replacing the interaction energy of the magnetic dipoles living on pyrochlore sites with the interaction energy of dumbbells consisting of equal and opposite magnetic charges that live at the ends of the diamond bonds (see figure 2.7c). Hence, one tetrahedron contains a net neutral magnetic charge.

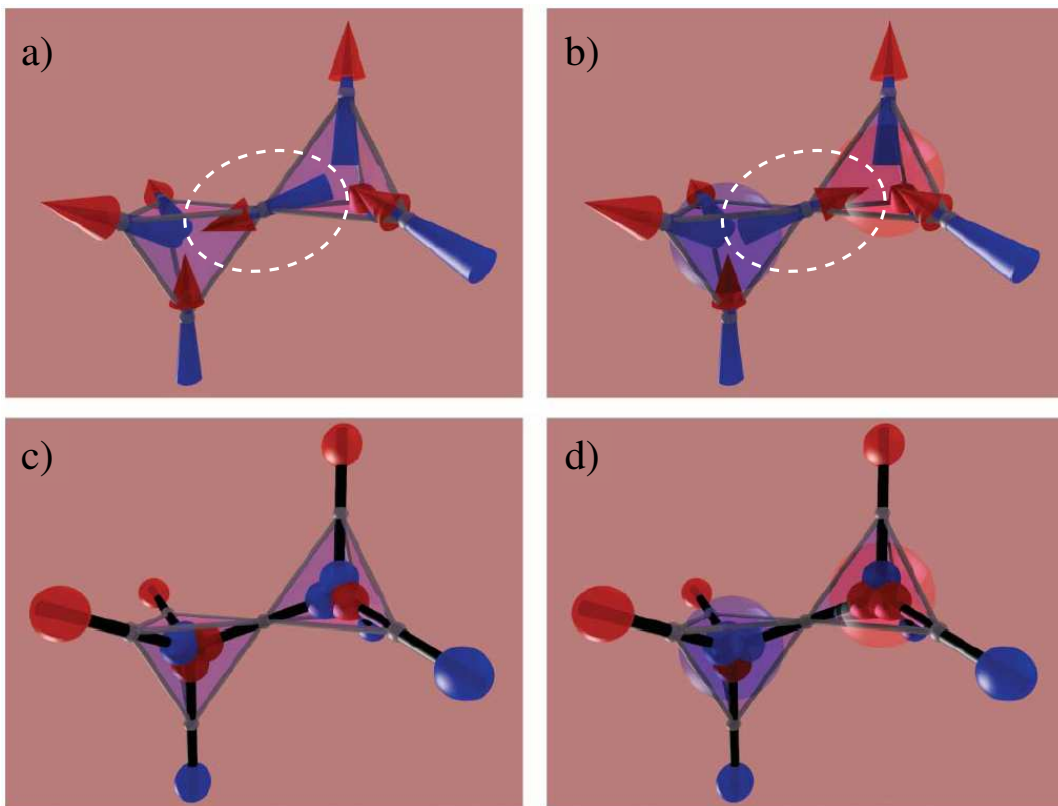


Figure 2.7: The dumbbell picture (c) and (d) is obtained by replacing each spin in (a) and (b) by a pair of opposite magnetic charges placed on the adjacent sites of the diamond lattice. In the left panels (a) and (c), two neighbouring tetrahedra obey the ice rule, with two spins pointing in and two out, giving zero net charge on each site. In the right panels (b) and (d), inverting the shared spin (see markers in (a) and (b)) generates a pair of magnetic monopoles. (Reproduced from Castelnovo et al. [Cas08].)

We now turn to the excited states. The most elementary excitation involves inverting a single dipole / dumbbell to generate a local net dipole moment (see figure 2.7b / 2.7d). The inverted dumbbell corresponds to two adjacent sites with net magnetic charge q_m – a nearest neighbour monopole-antimonopole pair. As shown in figure 2.8, the monopoles

can be separated from one another without further violations of local neutrality by flipping a chain of adjacent dumbbells.

A spin flip violates the ice rule in two tetrahedra, at an energy cost of about 2.8 K per tetrahedron in $\text{Dy}_2\text{Ti}_2\text{O}_7$. Crucially, these monopoles are deconfined, they can separate and move essentially independently. Thus, the equilibrium defect density is determined not by the cost of a spin flip but by the properties of the gas of interacting monopoles. It takes only a finite energy to separate the monopoles to infinity, and so they are the true elementary excitations of the system: the local dipolar excitation fractionalizes.

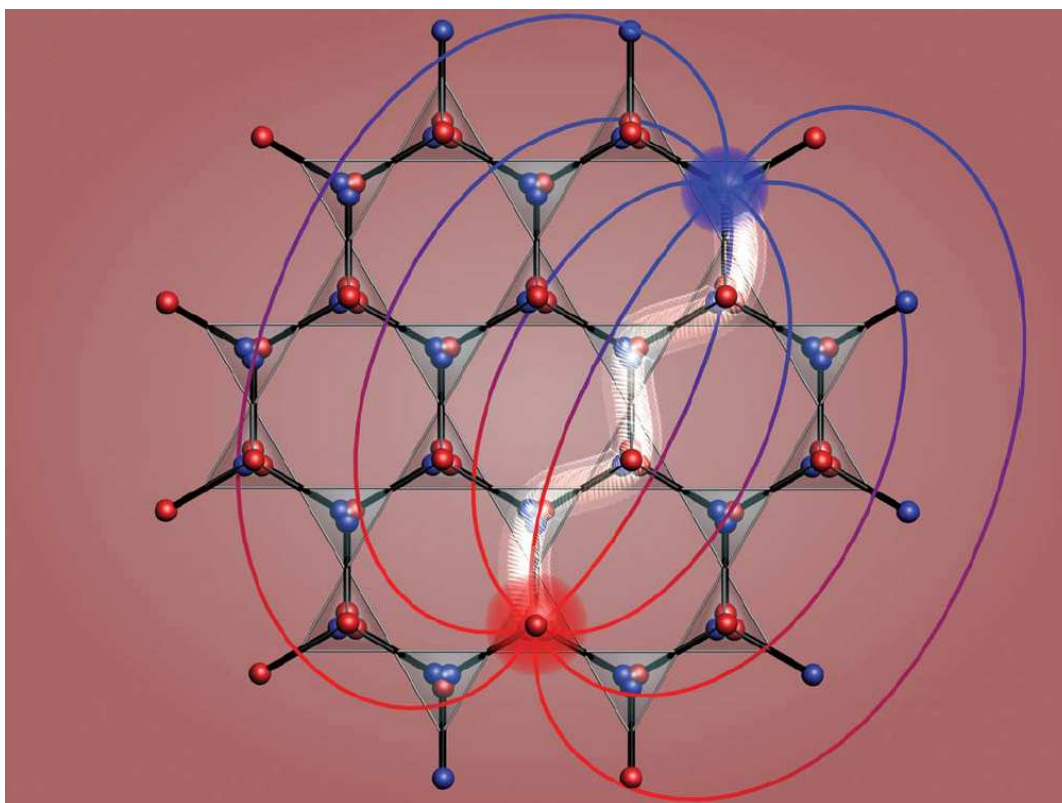


Figure 2.8: A pair of separated monopoles (large red and blue spheres). A chain of inverted dipoles (Dirac string) between them is highlighted in white, and the magnetic field lines are sketched. (Reproduced from Castelnovo et al. [Cas08].)

Monopole deconfinement is reflected in the spin configurations: as the two monopoles of opposite sign separate, they leave a tensionless string of reversed spins connecting them. These strings of reversed flux between the monopoles can be viewed as a classical analogue of a Dirac string: in the theory of Dirac [Dir31], these are infinitely narrow, unobservable solenoidal tubes carrying magnetic flux density (B -field) emanating from the monopoles. Here, the strings are real and observable thanks to the preformed dipoles

of the spins. Strings can change length and shape, at no cost in energy, other than the magnetic Coulomb interaction between their endpoints.

Compared to the monopole charge $q_D = h/\mu_0 e$ of an elementary magnetic monopole proposed by Dirac (derived from equation (2.3)), for the magnetic charge of monopoles in spin ice follows [Cas08]:

$$q_m = \frac{2\mu}{a_d} = \frac{q_D}{7700} \approx 4.3 \cdot 10^{-13} \frac{\text{J}}{\text{Tm}} \quad , \quad (2.4)$$

where $a_d = 0.434$ nm is the diamond lattice bond length in $\text{Dy}_2\text{Ti}_2\text{O}_7$.

In this work two possible ways of detecting these magnetic monopoles will be presented. Of course both of them are indirect methods. The first one is to identify the signature of the magnetic monopoles in the specific heat of $\text{Dy}_2\text{Ti}_2\text{O}_7$. The second one is to make the Dirac strings visible in a neutron scattering experiment.

2.4.1 Signature of magnetic monopoles in specific heat measurements ^{*}

In order to account to the fact that defective tetrahedra (monopoles) interact with each other via Coulomb coupling in dipolar spin ice, Castelnovo et al. [Cas09] propose to treat the monopoles as a two-component Coulomb plasma and use the Debye approximation to obtain the electrostatic contribution to the free energy [Lev02].

This model is described by the Debye-Hückel theory, a mean-field theory for mobile charges interacting via the Coulomb potential [Cha00]. It allows to obtain an approximate expression for the free energy of the system as a function of temperature, charge and chemical potential of the monopoles [Lev02], and from this one can calculate the specific heat using appropriate thermodynamic relations. The theory breaks down when typical length scales (screening length, monopole separation) become of the order of the lattice constant. This happens for temperatures above approximately 1 K, where the spin ice state in $\text{Dy}_2\text{Ti}_2\text{O}_7$ gives way to a more conventional paramagnet and monopoles cease to be suitable quasiparticles. For lower temperatures the specific heat of $\text{Dy}_2\text{Ti}_2\text{O}_7$ should be described by the Debye-Hückel theory (see section 6.1.4).

^{*}Results from the publication by Morris et al. [Mor09]

2.4.2 Signature of Dirac strings in neutron scattering experiments ^{*}

In the Dirac string picture, the spin ice ground state satisfying the ice rules can be considered as a dense network of inter-woven strings. If the applied field is zero, the strings have no privileged orientation and they describe isotropic, intertwined 3D random walks of arbitrary length. Excitations correspond to monopoles at the end of Dirac strings (broken loops) in the bulk. The cost of lengthening such Dirac strings is solely against the weak attractive force between the monopoles at their ends [Cas08]. Indeed, as the strings fluctuate between different configurations consistent with a given distribution of monopoles, there is not even a unique way of tracing their paths.

However, there exists an elegant remedy: the application of a large magnetic field along one of the principal axes (e. g. [001] direction) orients all spins. The resulting ground state is unique and free of monopoles – the “2-in & 2-out” ice rules are observed everywhere, and each tetrahedron is magnetized in the [001] direction as depicted in figure 2.9. Upon lowering the field, sparse strings of flipped spins appear against the background of this fully magnetized ground state. In the absence of monopoles, such strings must span the length of the sample and terminate on the surface; otherwise, they can terminate on magnetic monopoles in the bulk (as explained above).

When the density of these strings is small, interactions between them can be neglected to a first approximation, so that the spin correlations are those of a diffusion process. The string geometry

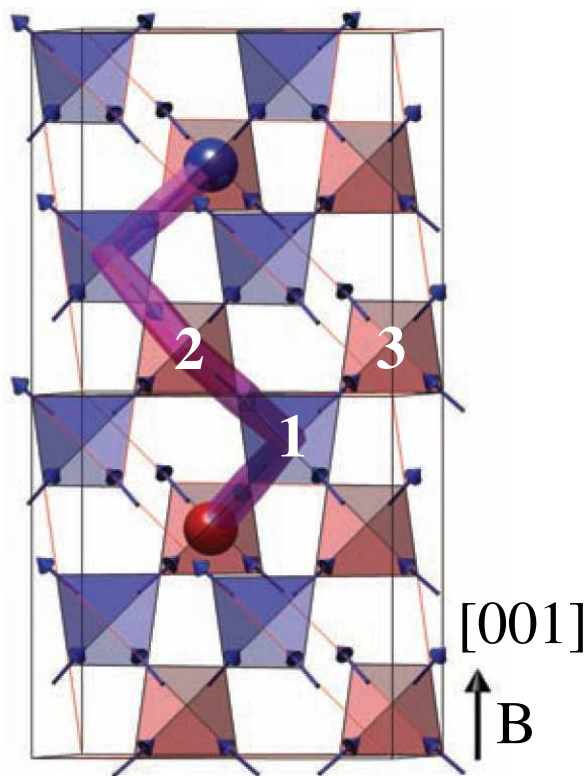


Figure 2.9: Dirac strings of flipped spins terminate on tetrahedra where magnetic monopoles reside (red and blue spheres). Applying a magnetic field, $B \parallel [001]$, results in a preference for aligning the tetrahedral magnetization with the applied field direction; see text. (Reproduced from Morris et al. [Mor09].)

^{*}Results from the publication by Morris et al. [Mor09]

can be modelled as the path of a random walk where the direction of the applied magnetic field assumes the role normally played by time (see figure 2.9): with every step in the positive field direction (e. g. from tetrahedron “1”), the walker chooses between one of the two possible sites in the next plane (“2” or “3”). Due to the cubic symmetry of the pyrochlore lattice, the displacements perpendicular to the magnetic field direction appear symmetrically.

The presence or absence of the strings at a given temperature and field is determined by a balance between the energy cost of producing them and the gain in entropy due to their presence. As pointed out in [Jau08] and [Jau09b], each link in the string will involve a spin being reversed against the field (note that this still maintains the “2-in & 2-out” ice rules along the string).

Each spin flip costs a Zeeman energy of μB , with B representing the strength of the field applied along [001] and $\mu = 10 \mu_B \cdot (2/\sqrt{3})$ being the magnetic moment per dysprosium ion along the [001] direction. As there are two possibilities to choose for the continuation of the string, there is an associated entropy per link of $s = k_B \ln 2$, where k_B is the Boltzmann constant. The free energy per link, as the string becomes large, is:

$$f = u - Ts = \mu B - k_B T \ln 2 \quad , \quad (2.5)$$

where u is the Zeeman energy and T is absolute temperature. We can define a magnetic field $B_{\text{Kas}}(T)$, where the free energy is equal to zero. Above this magnetic field, the number of strings goes to zero as the free energy of formation is macroscopic and positive. However, at the Kasteleyn field B_{Kas} , a transition occurs where strings spontaneously form as the free energy becomes favourable and the entropy of string formation wins. This transition is a three-dimensional example of a Kasteleyn transition [Jau08]. At a temperature of 0.7 K the Kasteleyn transition in $\text{Dy}_2\text{Ti}_2\text{O}_7$ should occur at $B_{\text{Kas}}(0.7 \text{ K}) = 0.7 \text{ K} \cdot (k_B \ln 2) / (20\mu_B/\sqrt{3}) \approx 0.06 \text{ T}$.

Evidence of this transition can be seen in the magnetization as a function of temperature and magnetic field parallel to the [001] crystal axis (figure 2.10). Whereas the magnetization in response to magnetic field, which is changed at constant temperature, only equilibrates above 0.6 K, in the spin ice state, below 0.6 K, the magnetization remains close to thermal equilibrium when cooled in zero magnetic field.

Above this temperature, the system shows a transition to saturation at a magnetic field consistent with that expected for the 3D Kasteleyn transition. Indeed, in the ergodic region of the phase diagram the saturation field coincides with the Kasteleyn field B_{Kas} , where a kink in the magnetization appears as it reaches its saturation value [Jau09b]. However, below approximately 0.6 K, equilibration times become so long that the system starts freezing [Jau09b], and the measured magnetization is no longer an equilibrium property.

The value of the Kasteleyn field determined from the magnetization data at 0.7 K is about 0.2 T. The difference to the theoretical calculated value can be explained due to a great demagnetization effect in the used $\text{Dy}_2\text{Ti}_2\text{O}_7$ sample.

By measuring close to the Kasteleyn transition, one should dial up a regime where the strings are sparse and oriented against the field direction. This gives the possibility to check the properties of these strings as described in section 3.1. The recent neutron scattering experiments published in 2009 have revealed the existence of magnetic monopoles as shown in the next chapter.

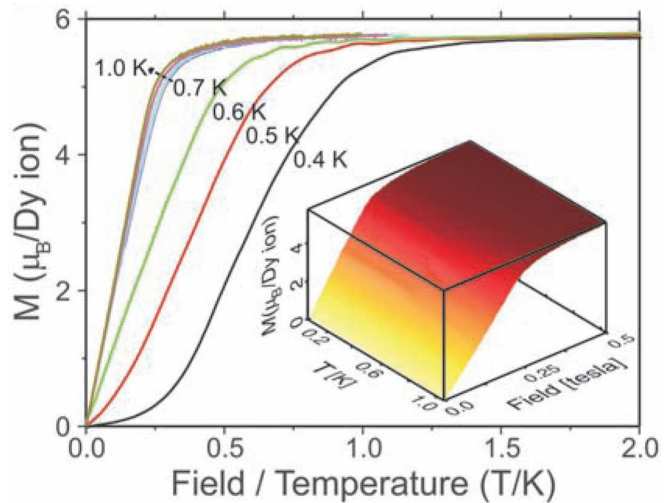


Figure 2.10: Main panel: Magnetization plotted versus magnetic field, $B \parallel [001]$, over temperature for several fixed temperatures, showing a clear departure from B/T scaling for $T < 0.7$ K. Inset: Surface of magnetization as a function of temperature and magnetic field. (Reproduced from Morris et al. [Mor09].)

Chapter 3

Recent Magnetic Monopole Studies Using Scattering Techniques

During the last two years in several publications on spin ice the existence of magnetic monopoles was experimentally evidenced. Different methods of finding the signatures of magnetic monopoles were used. In the first part of this chapter neutron measurements performed at HZB and their results are presented. At the end of this chapter a brief review on recent studies on spin ice by other groups is given.

3.1 Neutron measurements at HZB

At the BER II research reactor of the Helmholtz-Zentrum Berlin (HZB) we have undertaken neutron scattering measurements to verify the existence of Dirac strings in $\text{Dy}_2\text{Ti}_2\text{O}_7$ in the spin ice state. For this measurements the E2 flat cone diffractometer was used. In the next section a brief introduction to neutron scattering using the flat cone technique is given. The neutron measurements we have performed at HZB and their results are presented afterwards.

3.1.1 Neutrons and flat cone technique

Neutrons are particularly suited to study the structure of condensed matter. The neutron wavelength (in the order of 10^{-10} m) is comparable to atomic distances. Therefore, structures or in other words correlations can be investigated. As a result of their neu-

tral electric charge, neutrons interact rather weakly with matter and thus penetration depths are high and generally bulk properties can be studied. Neutrons interact with the atomic nucleus. Due to the fact that the scattering length varies strongly from element to element and also from isotope to isotope, neutrons can easily distinguish atoms of comparable atomic number. Neutrons carry a magnetic moment and can be polarized and are particularly suited to investigate magnetic structures and magnetic excitations. The flat cone technique is a special case of the Weissenberg technique which was developed for x-ray diffractometry [Bue42]. In this method a single crystal is rotated with respect to a specific crystal axis. Then, the reciprocal lattice planes normal to this axis will diffract in planes or cones.

By rotating the crystal around this axis all lattice points can be brought into a reflecting position with the exception of a blind region close to the axis. One main application of the flat cone technique is the observation of diffuse scattering between Bragg reflections.

3.1.2 Experimental set up for E2

The E2 instrument is located at the beam tube *R1* of the research reactor BER II of the Helmholtz-Zentrum Berlin (figure 3.1).

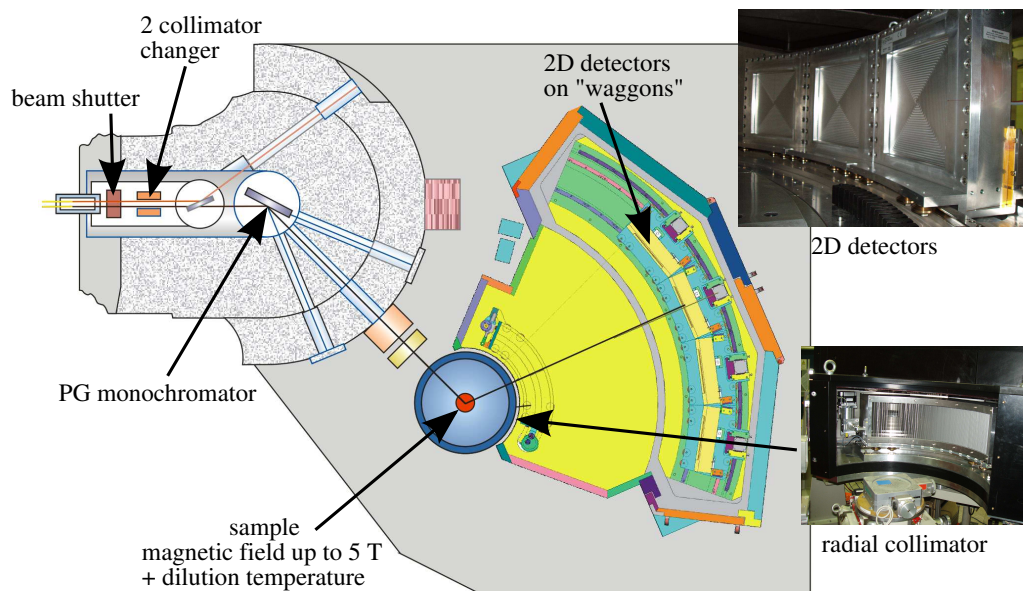


Figure 3.1: Instrument picture of the E2 flat cone diffractometer at the BER II research reactor [Hof10].

For the collimation of the primary beam a collimator of 30' divergence was chosen. The pyrolytic graphite (PG) monochromator provided a wavelength $\lambda = 2.39 \text{ \AA}$. For the measurement of the zero scattering plane of the crystal the sample is rotated around an axis ϕ which is vertical and perpendicular to the incident neutron beam.

The upper scattering layers are recorded with the ϕ axis tilted away from the vertical direction by an angle μ and with the detector inclined by the same angle with respect to the horizontal plane.

Due to the fact that the active areas of the detectors on the wagons covers only half of the 2θ angle space in the detector bank, two series of measurements are necessary with the four detectors at different positions.

To provide the necessary magnetic field for the experiment on E2 the cryomagnet VM-4, with a maximum magnetic field of 4 T was used. This magnet is particularly suitable for our experiment due to the large aperture angles, both in horizontal and vertical direction (see figure 3.2). The opening angle in the scattering plane allows us to map a wide region in Q-space ($0.75 \text{ r.l.u.} \lesssim \sqrt{h^2 + k^2} \lesssim 4 \text{ r.l.u.}$). The vertical opening angle of 35° allows us to use the whole area of the 2D-detector and therefore to measure an off-plane scattering. Using flat cone technique with a tilting angle of $\mu = 8^\circ$ (cryomagnet and detector) we were able to measure in total the planes from $l \approx -0.2 \text{ r.l.u.}$ to $l \approx 1 \text{ r.l.u.}$.

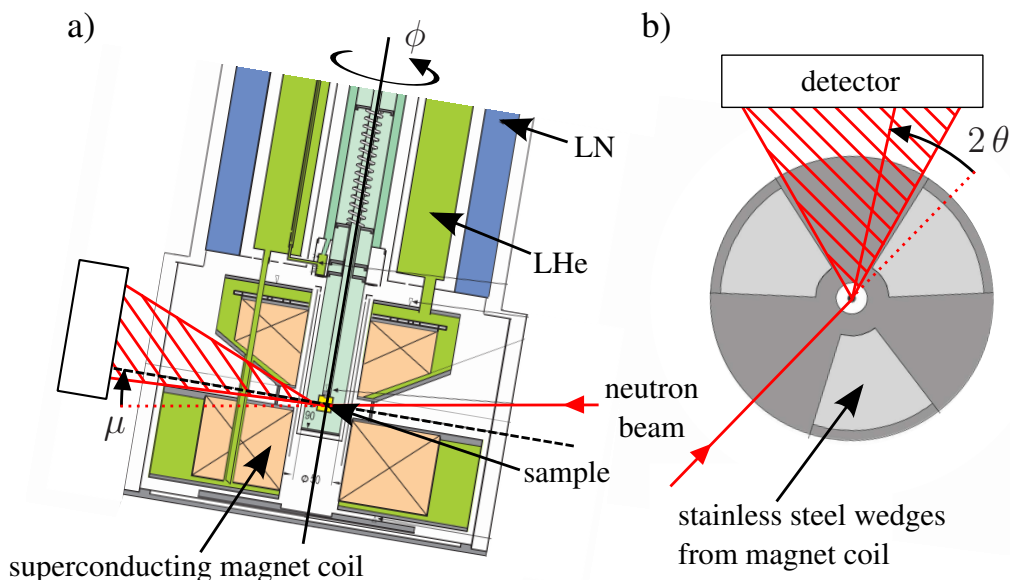


Figure 3.2: (a) Sketch of the cryomagnet VM-4. Liquid nitrogen (liquid helium) reservoir is coloured in blue (green). (b) Top view of the opening angles of the cryomagnet VM-4. Red lines depict the incoming neutrons and the dashed red sector the scattered neutrons. (Reproduced and modified from [Mei00].)

For all the experiments we used $\text{Dy}_2\text{Ti}_2\text{O}_7$ single crystal samples, which contains isotopically pure ^{162}Dy (95 - 98%) [Gri08]. The advantages of using pure ^{162}Dy on the one hand is a smaller absorption cross section for neutrons and on the other hand ^{162}Dy has no nuclear moment. The $\text{Dy}_2\text{Ti}_2\text{O}_7$ single crystal was aligned with the $[hkl] = [100]$ and $[010]$ directions in the horizontal scattering plane. Thus, the cryomagnet VM-4 provides a magnetic field along the $[001]$ crystal axis. Due to a possible spin freezing at temperatures below 0.65 K (see results from magnetization measurements presented in chapter 2.4.2) all neutron scattering measurements were performed at 0.7 K. To provide this temperatures a dilution inset (DS-2) for the cryomagnet was used. Data were collected and converted into 3D reciprocal space using the instruments *TVnexus* software. A measurement at saturated field ($B = 0.8$ T) was subtracted to reduce background contamination of the diffuse scattering.

3.1.3 Results of neutron measurements at HZB ^{*}

The ice-rules in spin ice are too weak to impose magnetic long-range order, but they do induce dipolar power-law correlations resulting in characteristic pinch-point features in neutron scattering [Isa04; Yav08; Fen07; Fen05; Fen04]. Figure 3.3 depict the pinch-point structure measured in $\text{Dy}_2\text{Ti}_2\text{O}_7$ at 0.1 K with an applied magnetic field of 0.72 T along the $[111]$ crystal axis. The long range correlation which causes the pinch-points occur in $\text{Dy}_2\text{Ti}_2\text{O}_7$ due to Dirac strings in zero field. As show in figure 3.4a this pinch-point structure is visible as 3D singularities in the zero field diffuse neutron scattering measurements, as well.

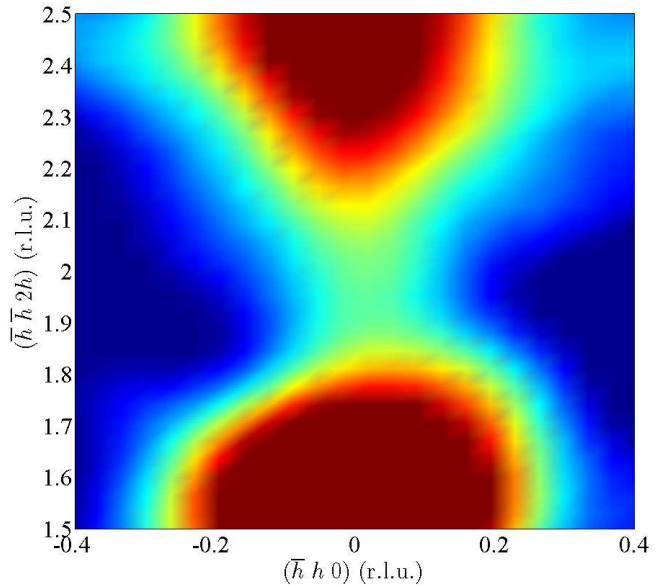


Figure 3.3: Pinch-point in E2 neutron diffraction data at 0.1 K with the magnetic field $B = 0.72$ T parallel to the $[111]$ direction.

^{*}The results have been published in *Science* **326**, 411, 2009 [Mor09]

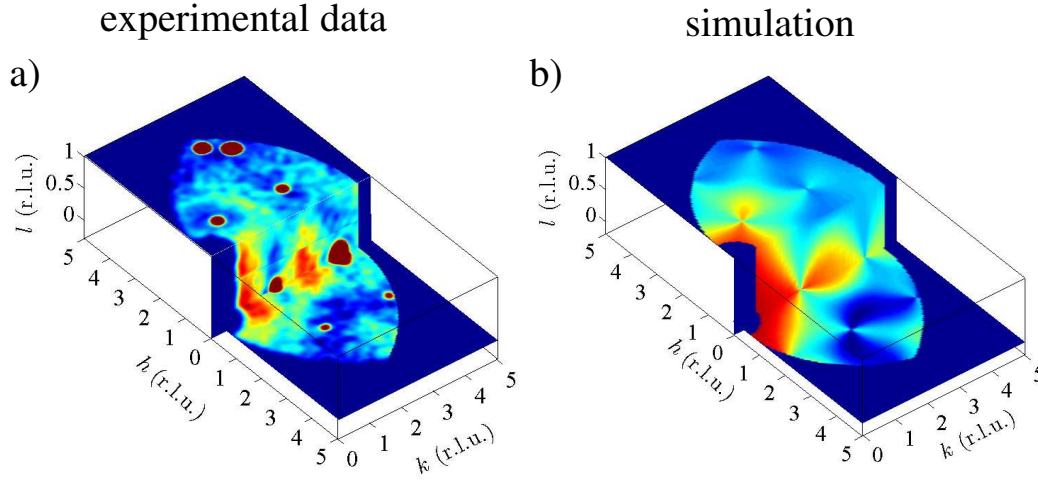


Figure 3.4: Three dimensional rendering of the dipolar correlations in reciprocal space (h, k, l) of spin ice at 0.7 K.

(a) experimental data: Neutron diffraction data taken at 0.7 K and $B = 0$ T on E2 with the diffuse peaks at $(0, 3, 0)$ and minima in $(3/2, 5/2, 0)$ positions. Bragg peaks (red spots) lie on top of the pinch points. A secondary Bragg peak is from a smaller crystallite.

(b) simulation: Pinch points are found in the correlation functions and these are three dimensional in nature with the diffuse scattering constricting at the reciprocal lattice point $(0, 2, 0)$ and its equivalents. Diffuse peak and scattering minima positions agree with the neutron data shown in (a).

Unfortunately, a few Bragg peaks (red spots) lie on top of the pinch-points. In the $\text{Dy}_2\text{Ti}_2\text{O}_7$ pyrochlore structure, the $(0, 2, 0)$ Bragg peaks should not appear. It is not understood why these peaks occur. One possible reason could be given by lattice deformation caused by magnetostriction [Sai05; Ruf10].

In order to compare with the neutron scattering measurements at zero field, we performed a large- N (self consistent mean-field) calculation [Isa04; Can01] supplemented with the relevant geometric factors for neutron scattering experiments and the magnetic form factor of dysprosium (figure 3.4b). Good agreement between theory and experiment (see also [Bra01a]) demonstrates that the correlations do indeed follow the predicted dipolar form.

Furthermore we wanted to investigate the existence of the Dirac strings in magnetic field. In the following, we first locate the Kasteleyn transition (see chapter 2.4.2) and hence the transition field B_{Kas} , then we discuss the neutron scattering data in detail by comparing it to a theoretical model.

To determine the Kasteleyn transition field B_{Kas} we have measured the field dependence of the $(0, 0, 2)$ Bragg peak intensity. In the saturated state where all spins are pointing

along the magnetic field direction the magnetic diffuse scattering vanished and a constant intensity of the magnetic Bragg peak is observable (see black dashed line in figure 3.5). For lower fields the intensity of the Bragg peak decreases due to the fact that the spins, as soon as they are not longer orientated by the magnetic field, contribute to the diffuse scattering intensity. By identifying the point where the Bragg peak intensity reaches the saturation value we can determine the Kasteleyn transition field (see figure 3.5).

In agreement with the magnetization

measurements (see figure 2.10) we determine the Kasteleyn transition field at $T = 0.7$ K to be $B_{\text{Kas}} = 0.7$ T. The difference to the theoretical calculated value (see section 2.4.2) can be explained due to a great demagnetization effect in the used $\text{Dy}_2\text{Ti}_2\text{O}_7$ sample. Measuring at a magnetic field which is lower than the Kasteleyn transition field we should be able to identify Dirac strings as an upcoming signature in neutron scattering data.

In figure 3.6a reciprocal space slices at a field near saturation of $B = \frac{5}{7} B_{\text{Kas}} = 0.5$ T are shown. Instead of the two lobes coming down to a pinch point in zero-field, cone-like scattering emanates from what was the position of the pinch point. As the field is decreased the diffuse scattering smoothly deforms back to the zero field form.

As described in section 2.4.2, the strings execute a random walk. In order to capture lattice effects, we simulate random walks on the pyrochlore lattice. Because there is a finite thermal population of monopoles and defects in the material, we expect the strings to be finite in length. For the field of $B = \frac{5}{7} B_{\text{Kas}} = 0.5$ T and temperature of 0.7 K a string length of the order 50 sites is required for agreement with the data. Indeed, for this temperature in zero field, the density of monopoles in numerical simulations according to the Debye-Hückel theory (see chapter 2.4.1 and 6.1.4) is found to be very low – well below 1 % of all tetrahedra – in agreement with a large

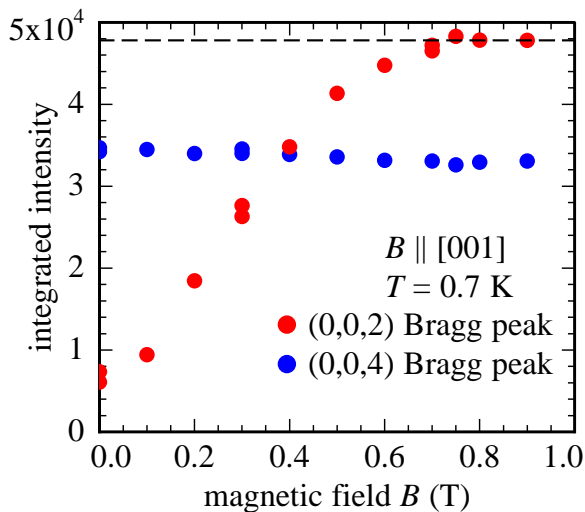


Figure 3.5: Integrated intensity of the (0,0,2) Bragg reflex (red dots) from neutron scattering data measured for various fields along the [001] crystal axis. For comparison, the (0,0,4) Bragg peak was measured and the integrated intensity (blue dots) was observed to be independent from magnetic field variations $B = 0 \dots 1$ T.

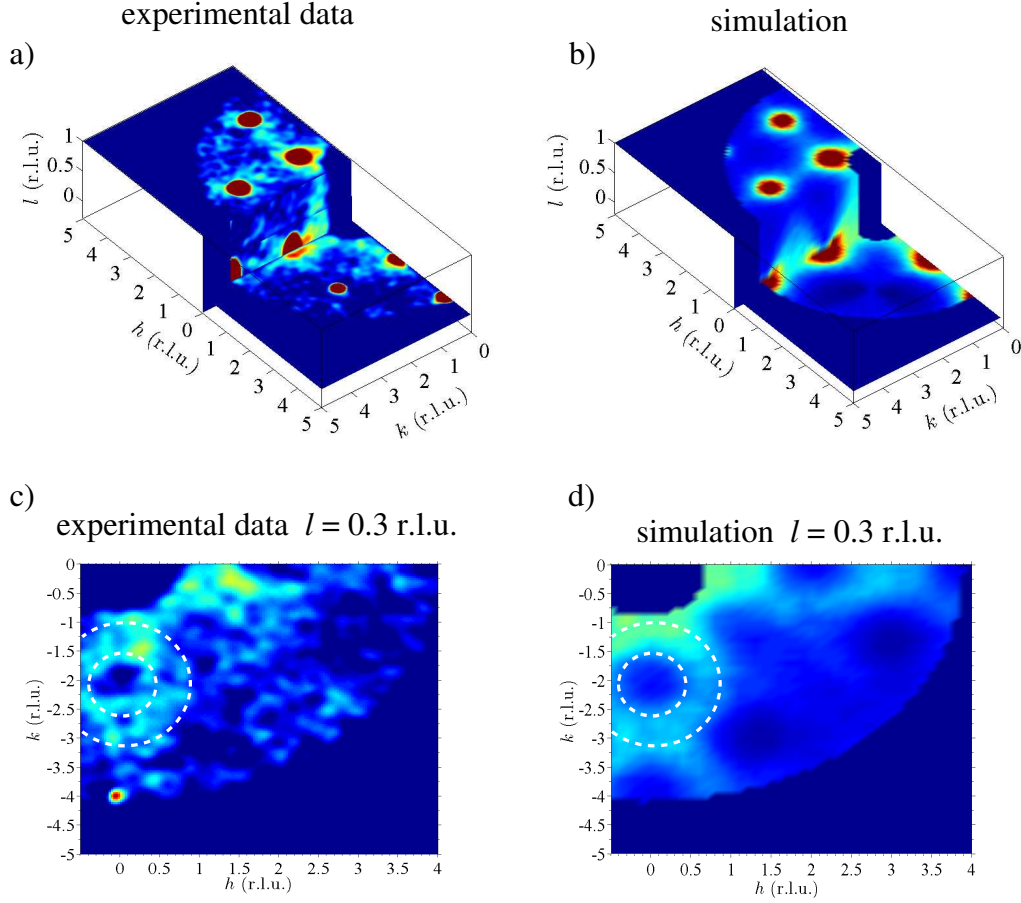


Figure 3.6: Diffuse neutron scattering with field applied along the $[001]$ direction.

(a) 3D representation of the single-crystal neutron diffraction data from E2, at $\frac{5}{7} B_{\text{Sat}} = 0.5$ T and 0.7 K showing a cone of scattering coming from $(0, 2, 0)$ Bragg peak.

(b) Calculation of diffuse scattering characteristic of the weakly biased random walk correlations with bias of $0.53 : 0.47$ and $B_{\text{int}} \parallel [001]$ (see text and equation (3.1)).

In the $l = 0.3$ r.l.u. plane the cone of scattering is clearly seen as a circular structure in the experimental data (c) and the simulation (d).

string length. The scattering from a large ensemble of such hard-core walks has been calculated including all the geometrical factors for the neutron scattering cross section (see figure 3.6b). As can be seen from the side-by-side comparison of the data and modelling, the string configurations account very well for the data and reproduce the cone of scattering observed. To get rid of the Bragg peak overlapping this feature, in the lower part of figure 3.6 the data set and the calculation for $l = 0.3$ r.l.u. is shown. Here, one can clearly see the cone like scattering as a ring of higher intensity (see markers).

To prove this behaviour under other conditions we repeated the experiment with an effective field tilted approximately 13° towards the $[011]$ direction, in order to induce a net tilt in the meandering of the strings. As depicted in figure 3.7a and 3.7b the cone of diffuse scattering collapses into sheets of scattering at an angle of 45° , matching the opening angle of the original cone in neutron scattering data.

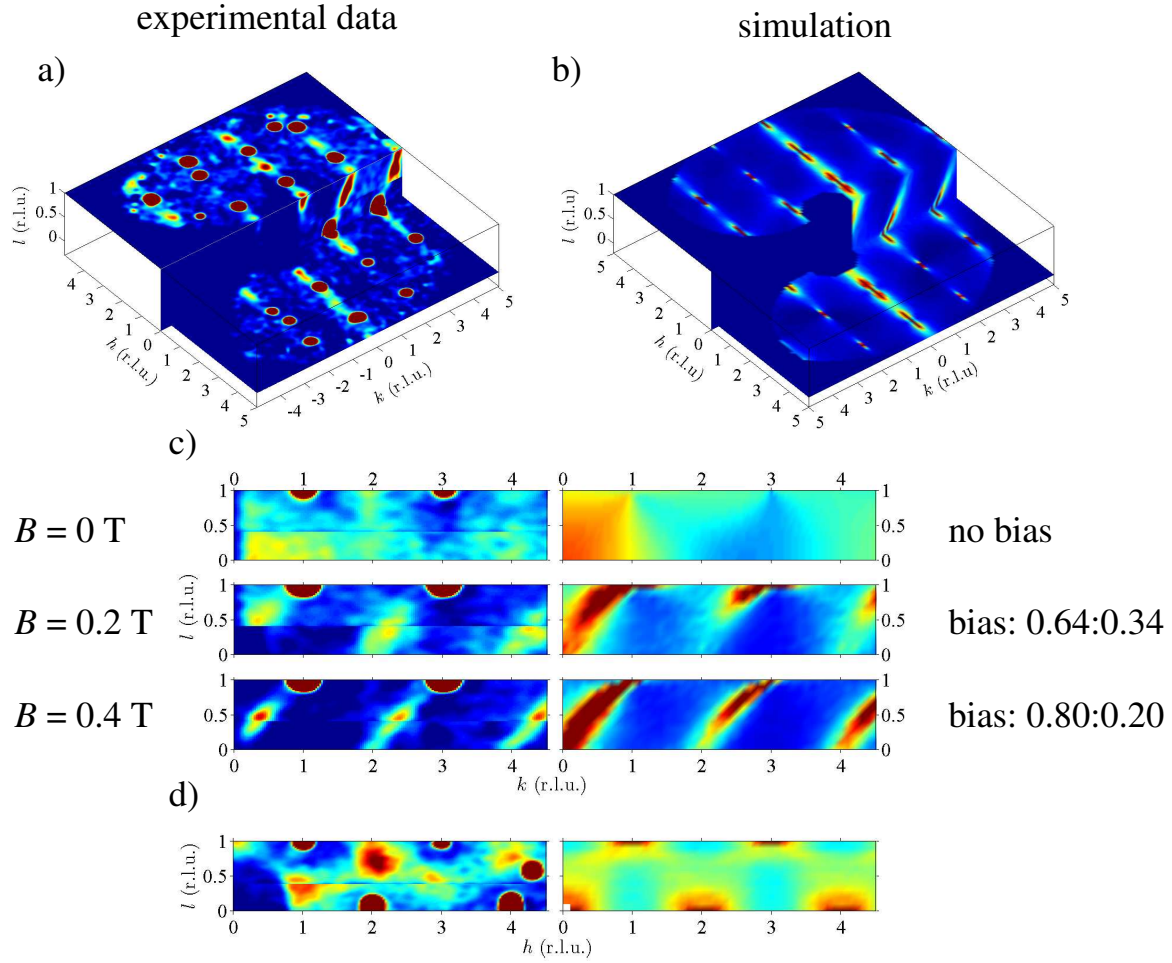


Figure 3.7: Biased random walks in tilted field.

(a) Neutron diffraction data from E2 showing the $(h, k, 0)$, $(h, k, 1)$ and $(0, k, l)$ planes taken at 0.7 K and a field of $4/7 B_{\text{sat}} = 0.4$ T. The red spots are Bragg peaks, with the peaks at $(2.7, -1.8, 0)$, $(1.3, -2.3, 1)$, $(3.8, -0.9, 1)$ and $(3.5, 2.5, 1)$ being from a smaller second crystallite.

(b) Random-walk string model with biasing 0.80 : 0.20.

(c) Field dependence of the diffuse scattering and calculations in the $(1, k, l)$ plane. Spin ice scattering collapses into walls of scattering at higher fields. Further understanding of the Dirac string and monopole physics may improve our modelling of the data.

(d) Data versus calculation for the (h, l, l) diffuse wall of scattering at $B = 0.4$ T (see text).

This sharp sheet in reciprocal space widens with decreasing field (figure 3.7c). Within the random walk model, tilting the applied magnetic field changes the relative probabilities of each step (thus generating an aligned (“biased”) random walk) as inequivalent spin flips require different energy costs. The field and temperature dependent Boltzmann factor for the ratio of probabilities of stepping from tetrahedral site 1 to site 2, or site 1 to site 3 (see figure 2.9) is

$$\frac{p(1 \rightarrow 2)}{p(1 \rightarrow 3)} = \exp\left(\frac{2\mu|B_{\text{int}}|(\cos\phi_1 - \cos\phi_2)}{k_{\text{B}}T}\right) . \quad (3.1)$$

Here, ϕ_1 and ϕ_2 are the angles between the magnetic moments on the two final sites and the magnetic field B_{int} .

Because of the ferromagnetism induced in spin ice, demagnetization effects must be carefully accounted for in the modelling. A bias of 0.80:0.20 at $4/7 B_{\text{sat}}$, and 0.64:0.36 at $2/7 B_{\text{sat}}$ is anticipated from equation (3.1). Using these weighting factors and modelling the new ensemble of Dirac strings, the tilts and widths of the scattering are reproduced. There still remains the issue of inter-string correlations. Comparison with the hard-core string model (figure 3.7c and 3.7d) shows that the simple random walk approach does not capture the intensity distribution so well. Figure 3.7d shows a cut through the walls of scattering in the (h, l, l) plane at $B = 0.4$ T. The discrepancies between the measured data and the calculations might be reduced if one includes in the model strings with different lengths. Another possibility could be that there are correlations between the strings, which can not be neglected. Further calculations are needed including interactions between strings to clarify this in detail.

Our study of the spin ice state in zero field and under an applied magnetic field along [001] lend support to the strongly correlated and degenerate nature of the ground state, and the resulting long range dipolar correlations. The low energy excitations of such a complex ground state are remarkable in their simplicity, and can be accounted for by weakly interacting pointlike quasiparticles, the magnetic monopoles connected by extended objects, the Dirac strings of reversed spins. Under fields applied along [001], the picture is that of Dirac strings of reversed spins meandering along the direction of the applied field and terminating on monopoles. This picture accounts very well for the spin correlations observed through neutron scattering. This description is rather robust,

and gives a simple picture of the spin configuration under tilted fields in terms of biases in the string direction.

Our main result consists in the experimental identification of these string-like spin excitations in a gas of magnetic monopoles. These constitute hardy and practical building blocks for the understanding of the low energy behaviour of spin ice. Perhaps, the most intriguing open issue is the precise connection between these building blocks and the low temperature freezing observed in the spin ice compounds [Jau09a; Sny01] and in the thermal relaxation measurements described in the next chapters.

3.2 Recent results from other research groups

During the last two years in several publications on spin ice the existence of magnetic monopoles was experimentally evidenced. Different methods of finding the signatures of magnetic monopoles were used: neutron scattering, muon spin rotation experiments and specific heat measurements were performed.

Unpolarised neutron scattering experiments by Harris et al. [Har97] and Bramwell et al. [Bra01b] on spin ices such as $\text{Ho}_2\text{Ti}_2\text{O}_7$, have established that the dipolar spin ice model, in which the rare earth ions are coupled by the dipole-dipole interaction and competing superexchange, gives an accurate description of bulk and microscopic properties [Bra01a; Yav08]. The underlying reason for the persistence of spin ice behaviour in this more complex model is that the dipolar Hamiltonian has been shown to have practically identical groundstates to the near neighbour (i. e. ice rules) model [Isa04; Isa05], a feature known as projective equivalence. The two groundstates differ by small corrections expected to vanish as r^{-5} . It is therefore strongly expected that the spin-spin correlations of $\text{Ho}_2\text{Ti}_2\text{O}_7$ should exhibit a pseudo-dipolar form.

Fennell et al. [Fen09] have measured the scattering of polarized neutrons from the prototypical spin ice $\text{Ho}_2\text{Ti}_2\text{O}_7$. By separation of different contributions to the magnetic correlations they were able to demonstrate the existence of a Coulomb phase in this material and they have confirmed the validity of projective equivalence [Isa05]. This and the zero field results on $\text{Dy}_2\text{Ti}_2\text{O}_7$ presented in section 3.1.3 were the first proof of a Coulomb phase in a real magnetic material. The temperature dependence of the scattering is consistent with the existence of deconfined magnetic monopoles connected by Dirac strings of divergent length. They were able to attribute the observed broadening of the pinch-points to the existence of unbound defects connected by Dirac strings with a length

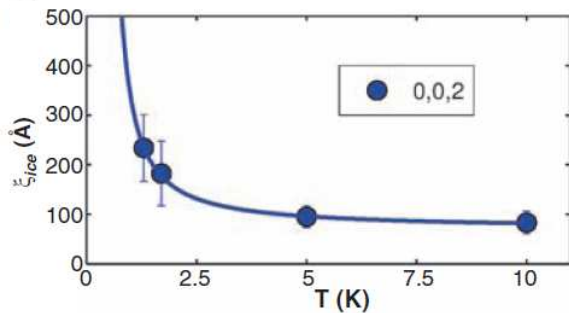


Figure 3.8: Correlation length ξ_{ice} for the spin ice $\text{Ho}_2\text{Ti}_2\text{O}_7$ which has a temperature variation that is consistent with an essential singularity $\propto \exp(E_0/T)$, see text. (Reproduced from Fennell et al. [Fen09].)

up to ξ_{ice} [Cas08; Jau09a]. At high temperatures, the proliferation of bound defects will both disrupt existing strings and reduce the mean free path for diffusing monopoles, reducing the maximum length in the Dirac string network. As the temperature is reduced, the thermal defect population decreases, and ξ_{ice} diverges as approximately $\exp(E_0/T)$ (see figure 3.8), with the observed value of E_0 close to the effective exchange $J_{\text{eff}} = 1.8$ K for $\text{Ho}_2\text{Ti}_2\text{O}_7$ [Bra01b]. Such a temperature variation of ξ_{ice} is the same as that of the correlation length of the one-dimensional Ising ferromagnet, which is indeed the maximum length of a ferromagnetic string in such a system. In other words: bound monopole pairs dominate at finite temperature, but unbound pairs become relatively more important at low temperatures. The length of the longest Dirac strings has been estimated to rise to macroscopic scales as the temperature passes below 1 K.

Bramwell et al. [Bra09] have investigated whether magnetic charges and their associated currents (‘magnetricity’) could

be directly measured in an experiment, without recourse to any material-specific theory. By mapping the problem onto Onsager’s theory of weak electrolytes [Ons34], they showed that this is possible, and devise an appropriate method. By using muon spin rotation method as a convenient local probe, the spin ice $\text{Dy}_2\text{Ti}_2\text{O}_7$ was investigated. The measured relaxation rate λ of muons implanted into $\text{Dy}_2\text{Ti}_2\text{O}_7$ mirrors for high temperatures the known behaviour of the magnetic relaxation time, decreasing with temperature as $\exp(\text{const}/T)$ [Jau09a] (see blue line in figure 3.9). At low temperatures λ increases with tem-

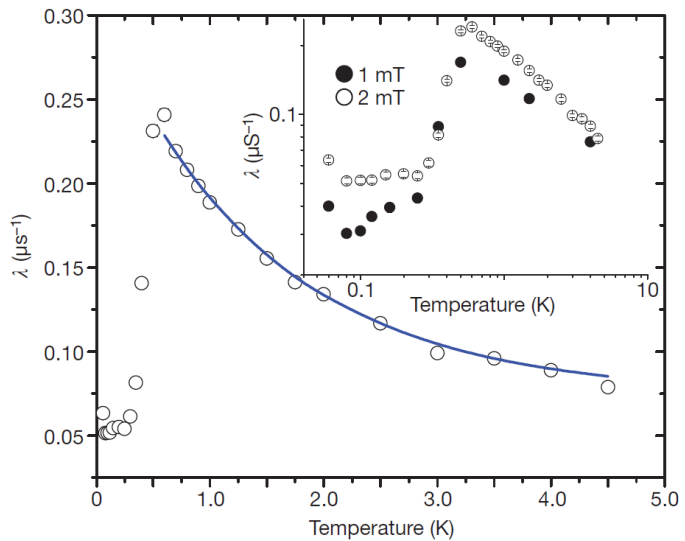


Figure 3.9: Temperature dependence of the muon relaxation rate λ in $\text{Dy}_2\text{Ti}_2\text{O}_7$.

Main panel: Data measured at an applied magnetic field of 2 mT. The high temperature regime follows the expected activated behaviour as described in the text (fit is shown as a solid line). At low temperature, λ is proportional to the monopole concentration. Its rapid increase above 0.3 K marks a crossover from the regime of weak screening to strong screening of the charges.

Inset: Data on a logarithmic scale along with data taken at 1 mT. The non-monotonic temperature dependence at low temperature is encompassed by Onsager’s theory.

(Reproduced from Bramwell et al. [Bra09].)

perature, with a crossover region above ≈ 0.3 K. Their experimental measurements have proved that magnetic charges exist in this material and have measurable currents. Bramwell et al. have as well measured relative changes in the magnetic conductivity and proved that monopole currents exist. They have shown that deconfined magnetic charges exist in a spin ice material, that they interact by Coulomb's law and are accelerated by an applied magnetic field. Their experimental results are consistent with those discussed by other groups [Cas08; Jau09a], but more directly probe the quantities of interest in the regime of temperature and magnetic field where a dilute gas of magnetic monopoles can be interrogated. Bramwell et al. [Bra09] characterized deviations from Ohm's Law and determine the elementary unit of magnetic charge to be $4.64 \cdot 10^{-13}$ J/Tm, which is in agreement to that predicted by Castelnovo et al. [Cas08] using the microscopic theory of spin ice (see equation (2.4)). New results presented by Uemura [Uem10] have shown, that a great amount of muons were not implanted in the $\text{Dy}_2\text{Ti}_2\text{O}_7$ sample material but in the silver sample holder. Therefore it might be possible that the interpretation of the measurement results related to magnetic monopole dynamics and monopole currents in $\text{Dy}_2\text{Ti}_2\text{O}_7$ have to be revised.

Kadowaki et al. [Kad09] performed both measurements of specific heat and neutron scattering with magnetic field parallel to the [111] direction. They assume that a straightforward signature of monopole-pair creation should be an Arrhenius law in the temperature dependence of the specific heat, $\propto \exp(-\Delta E/k_B T)$, where ΔE is a magnetic field dependent creation energy. One can simply expect $\Delta E = E_0 - \mu B$ owing to the Zeeman effect, with $E_0 \sim 5$ K as pair creation energy. Figure 3.10 shows their measured specific heat of $\text{Dy}_2\text{Ti}_2\text{O}_7$ under a [111] applied field as a function of $1/T$. The Arrhenius law is seen at low temperatures, indicating that monopole-antimonopole pairs are

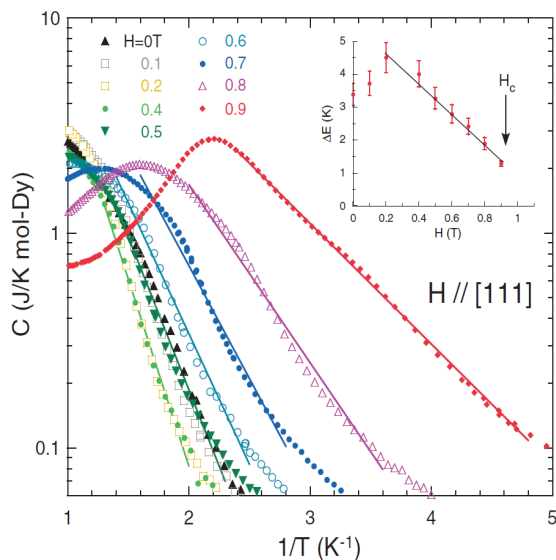


Figure 3.10: Specific heat measured with applied magnetic field along [111] axis is plotted as a function of $1/T$. In the intermediate temperature range these data are well represented by the Arrhenius law denoted by solid lines. The inset shows the field dependence of the activation energy ΔE .

(Reproduced from Kadowaki et al. [Kad09].)

thermally activated from the ground state. Therefore, the density of monopoles can be controlled by temperature and magnetic field.

Neutron scattering measurements of spin correlations performed by Kadowaki et al. [Kad09] show that close to the critical point the magnetic monopoles are fluctuating between high- and low-density states, supporting the fact that the magnetic Coulomb force acts between them. From their neutron scattering experiments they conclude that regions of low-density monopoles produce a typical Kagomé-ice scattering pattern, while those of the high-density monopoles produce the diffuse scattering around the Bragg reflections. These critical fluctuations between high- and low-density phases reinforce the proposed explanation [Cas08] of a liquid-gas type critical point [Sak03] using the similarity argument to phase transitions of ionic particle systems [Kob02]. Consequently, they conclude that these fluctuations strongly suggest the existence of magnetic monopoles interacting via the magnetic Coulomb force.

Chapter 4

Thermal Transport and Relaxation in Dielectric Crystals

4.1 Basic concepts of thermal measurements

There are two main material properties (thermophysical properties) associated with heat transfer in materials. These are the ability of a material to store heat and the ability to transfer heat by conduction.

If a specific amount of heat dQ is supplied to a thermally isolated specimen of mass m the relationship between heat and temperature increase dT is given by:

$$dQ = m c_p dT \quad . \quad (4.1)$$

Consequently the ability of a material to store heat is characterized by the specific heat capacity at constant pressure c_p . For gases and some liquids a distinction between the specific heat capacity at constant pressure c_p and at constant volume c_v is made. This is due to the work required for the thermal expansion of the gas or liquid. For solids this contribution is very small in comparison to the measurement uncertainty and can be neglected.

The thermal conductivity κ is the material property associated with heat conduction and is defined by Fourier's law:

$$q = -\kappa \frac{\partial T}{\partial x} = -\kappa \frac{\Delta T}{d} = \frac{\Delta T}{R_{\text{th}}} \quad . \quad (4.2)$$

Here, q is the heat flux, the heat conducted during a unit time through a unit area, driven by a temperature gradient $\partial T/\partial x$. In practice, for thermal conductivity measurements, the temperature difference ΔT between two opposite surfaces of a sample with a separation of d is determined. The quotient of distance and thermal conductivity is the thermal resistance R_{th} . In contrast to the storage of heat, conduction is considered as a steady-state process, i. e. the temperature field and the heat flux within heat-conducting materials are not a function of time.

But, in most cases both heat conduction and heat storage are simultaneously occurring processes. This is taken into account by the transient heat conduction equation. The temperature field $T(x, t)$ in one dimension is dependent on the location x and time t :

$$\frac{\partial T}{\partial t} = D \frac{\partial^2 T}{\partial x^2} \quad . \quad (4.3)$$

The thermal diffusivity D is given as the ratio of the thermal conductivity and the product of density and specific heat capacity:

$$D = \frac{\kappa}{\rho \cdot c_P} \quad . \quad (4.4)$$

From its physical meaning thermal diffusivity is associated with the speed of heat propagation.

Based on the fundamental laws of heat conduction and storage three different methods to measure these thermophysical properties can be distinguished. The first one is the steady-state approach using (4.2) in order to determine the thermal conductivity. Steady state conditions mean that the temperature at each point of the sample is constant, i. e. not a function of time. The determination of the thermal conductivity is based on the measurement of a heat flux and a temperature gradient, i. e. mostly a temperature difference between opposite surfaces of a sample. If the specific heat capacity is the property of interest, a calorimetric method based on (4.1) is used. In this case, heat is supplied to a sample that is isolated from the surroundings, and the change of the (mean) sample temperature is measured. The third approach is the simultaneous determination of both properties by a transient technique. For that purpose numerous solutions of the transient heat conduction equation based on one- (4.3), two-, or three-dimensional geometries have been derived. The main experimental problem for all methods for the determination of thermal properties is that ideal

thermal conductors or insulators do not exist. For most of the measurements one can neglect, that there are e. g. intrinsic relaxation effects in the sample material. Let us take the specific heat measurement on $\text{Dy}_2\text{Ti}_2\text{O}_7$ at low temperatures ($T < 2$ K) as an example where deviations from that simple behaviour occur.

At low temperatures, heat capacity measurements are mostly based on the relaxation type method. Here, the sample is thermally linked to the heat sink at constant reference temperature T_R . After applying a constant heating power \dot{Q}_S (at $t = 0$) the temperature increase $\tilde{T}(t) = T(t) - T_R$ is recorded. Based on the first law of thermodynamics the temperature increase can be calculated in linear approximation according to $\tilde{T} = \dot{Q}_S/K_R (1 - \exp(-t/\tau_{\text{SB}}))$, where K_R is the conductance of the thermal link at T_R . The sample heat capacity C_R at the reference temperature T_R then follows from the sample-to-bath time constant $\tau_{\text{SB}} = C_R/K_R$. For $t \gg 100$ s, the final temperature rise in our measurements saturates at a value of ≈ 1 % of the initial base temperature T_R . In figure 4.1 the temperature increase $\tilde{T}(t)$ is shown as recorded in a relaxation type calorimeter for a single crystalline $\text{Dy}_2\text{Ti}_2\text{O}_7$ sample at different reference temperatures. In the case that the relative temperature deviations $1 - \tilde{T}(t)/\tilde{T}_{\text{max}}$ from the maximal temperature increase $\tilde{T}_{\text{max}} = \dot{Q}_S/K_R$ is plotted on a logarithmic scale as function of time, one expects a straight line. As can be seen in figure 4.1, this is really true for a reference temperature of 1.029 K. Below 1 K, however, non-exponential temperature profiles become obvious. As we were able to expand the recording of the temperature profiles to a time resolution of 0.1 s, we find that in such thermal experiment non-exponential temperature responses are valid in a time-domain from 0.1 s up to 300 s and in a temperature range between 0.3 K and approximately 1 K (see also figure 5.4). A commonly applied solution to the problem of non-exponential temperature responses is a data fitting procedure based on the so-called 2- τ -analysis [She85; Hwa97]. With this thermal model, relaxation processes, intrinsic to the sample volume, of characteristic time τ_i and/or the existence of a finite thermal contact between sample and calorimeter chip have been accounted for. In case, it can be shown that for $\tau_i \ll \tau_0$, the so-called Shephard-correction results in a single exponential fitting procedure yielding in a sample heat capacity based on the long-time temperature response near to \tilde{T}_{max} . Using this technique of data analysis results not in a sufficient agreement between theory and measurements. Thus, we propose that in $\text{Dy}_2\text{Ti}_2\text{O}_7$ a multitude of subsystems should exist which couples on different time scales to the phonons.

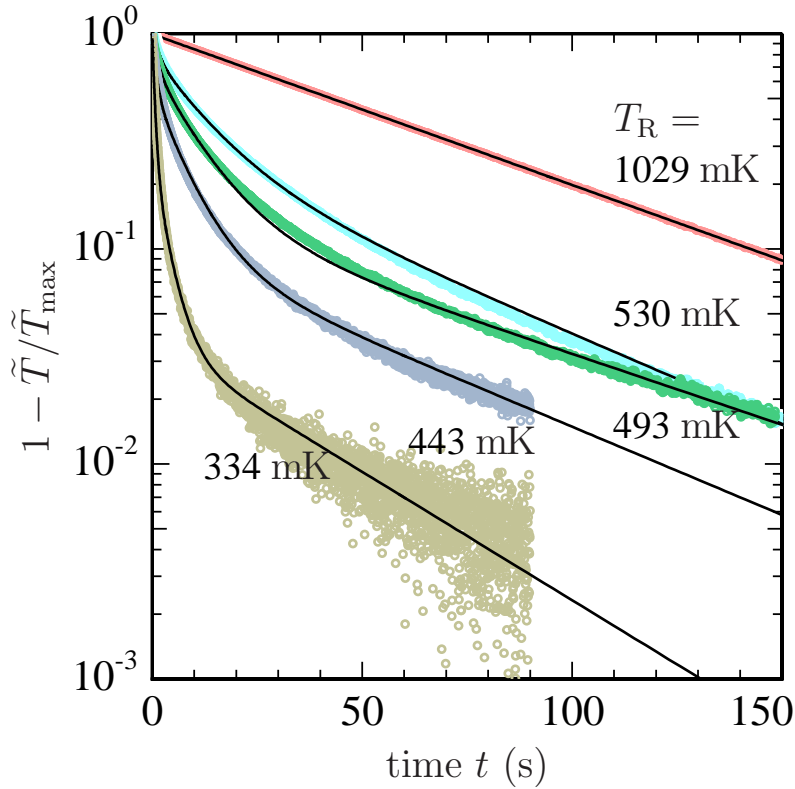


Figure 4.1: Temperature increase $\tilde{T}(t)$ as recorded in a relaxation type calorimeter for a single crystalline $\text{Dy}_2\text{Ti}_2\text{O}_7$ sample at different reference temperatures T_R . For a thermodynamically simple material the temperature increase is expected to vary in time according to $\tilde{T}(t) = \tilde{T}_{\max} \cdot (1 - \exp(-t/\tau_{\text{SB}}))$, so that the relative temperature deviation $1 - \tilde{T}(t)/\tilde{T}_{\max}$ from \tilde{T}_{\max} in the semi-logarithmic plot would follow a straight line. This is only valid for $T_R = 1.029$ K. For $T_R \leq 530$ mK, deviations from the exponential time dependence become obvious. The description of the non-exponential temperature profiles requires a suitable thermodynamic field theory. The full line graphs represent solutions of thermodynamic field equations, where the heat carrying phonons interact with three magnetic subsystems (see chapter 6).

The thermodynamic description of these multi component systems is possible by using the thermodynamic field theory, which will be introduced in the next section.

4.2 Thermodynamic field theory

With the thermodynamic field theory (TFT) Peter Strehlow and co-workers [Str94; Mei96; Mei04] have described the tunneling states in vitreous silica. They have shown that in silica glasses different subsystems (namely tunneling states, electronic spin and nuclear spin systems) can be identified in the temperature-time profiles measured with a relaxation type calorimeter (see figure 4.2).

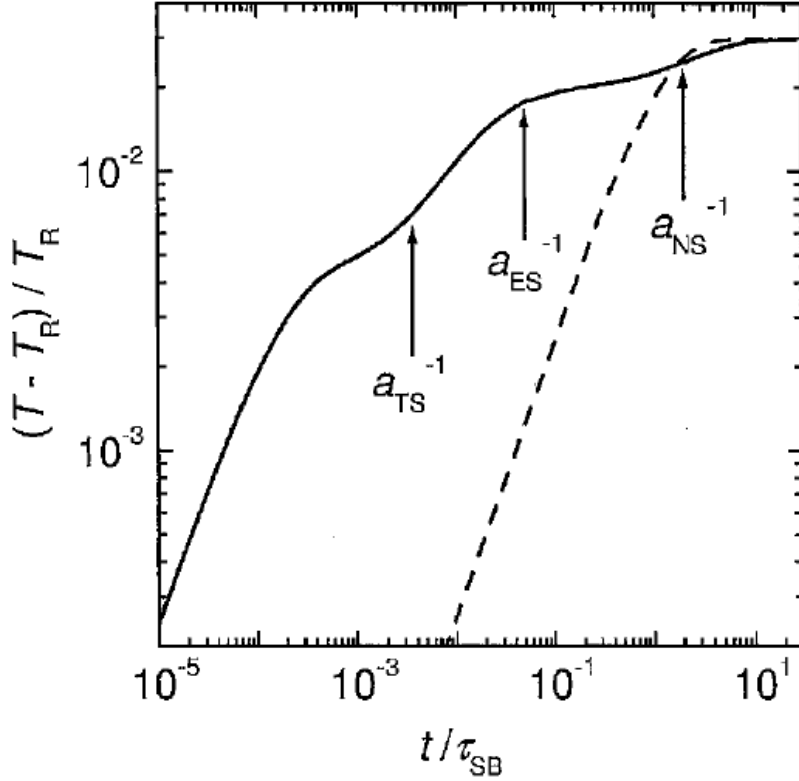


Figure 4.2: Typical temperature profile measured by heat-flow relaxation method as has been calculated from TFT for a model glass with heat carrying phonons and three separate thermal subsystems (at reference temperature $T_R < 1$ K). The thermal equilibration of tunneling states (TS), electronic spins (ES) and nuclear spins (NS) appears in a time domain from about 1 ms to 1 s and is described by TFT. The dashed line corresponds to a single relaxation function of a simple system, only. (Reproduced from Meißner et al. [Mei04].)

Using the thermodynamic field theory one can determine from these profiles the particular heat capacities of the subsystems and the associated coupling constants to the phonons. For $\text{Dy}_2\text{Ti}_2\text{O}_7$ using the thermodynamic field theory one has to implement three (magnetic) subsystems which are coupled to the phonon bath to describe the specific heat measurements.

The main objective of this concept is the determination of macroscopic field variables such as temperature and heat flux in all positions of the sample and for all times. In order to achieve this objective one needs field equations. For an insulating crystalline sample the suitable field equations can be derived from the kinetic theory of a phonon gas. In general, an infinite hierarchy of macroscopic equations based on the Boltzmann-Peierls equation is required to describe the entire spectrum of the time- and

space dependent behaviour of a phonon gas. The first set of equations in this hierarchy is the nine-momentum system which involves the phonon energy density, the heat flux vector and the deviatoric part of the pressure tensor. For this system, field equations can be obtained using Callaway's relaxation time approximation [Cal59]. It is expected that this nine-moment system covers all of the thermal transport phenomena to be observed in crystalline systems at low temperatures; namely ballistic propagation of phonons, second sound and thermal diffusion.

In most crystals, however, the thermodynamic variable space defined by the (nine) phonon state variables has to be extended by additional macroscopic field variables such as the energy densities of magnetic excitations. This is especially true for magnetic defects in geometrically frustrated magnets treated as noninteracting quasiparticles. In the following it is assumed that the magnetic excitations are localized, so that heat is transported by phonons, only.

In the kinetic theory, the state of a phonon gas is described by the phase density $f(\mathbf{k}, \mathbf{x}, t)$ which represents the number density of phonons of wave vector \mathbf{k} at a position \mathbf{x} and time t . For small values of k , the dispersion relation for all types of phonons has the form $\omega = c_D k$, where ω is the angular frequency and c_D is the Debye velocity of phonons. The phase density obeys the Boltzmann-Peierls equation

$$\frac{\partial f}{\partial t} + c_D \frac{k_i}{k} \frac{\partial f}{\partial x_i} = \xi \quad , \quad (4.5)$$

where ξ is the phase density of production. Multiplication of equation (4.5) with the phonon energy $\hbar \omega = \hbar c_D k$, the phonon momentum $\hbar k_i$ and the deviatoric part of the phonon momentum flux $\hbar c_D k_{\langle i} k_{j \rangle} / k$, respectively, and integration over all momentum space provide the macroscopic moment equations

$$\begin{aligned} \frac{\partial e_{\text{ph}}}{\partial t} + c_D^2 \frac{\partial p_i}{\partial x_i} &= \int \hbar c_D k \xi \, d^3 k \\ \frac{\partial p_i}{\partial t} + \frac{1}{3} \frac{\partial e_{\text{ph}}}{\partial x_i} + \frac{\partial N_{\langle ij \rangle}}{\partial x_j} &= \int \hbar k_i \xi \, d^3 k \\ \frac{\partial N_{\langle ij \rangle}}{\partial t} + \frac{c_D^2}{5} \left(\frac{\partial p_i}{\partial x_j} + \frac{\partial p_j}{\partial x_i} - \frac{2}{3} \frac{\partial p_k}{\partial x_k} \delta_{ij} \right) + \frac{\partial M_{\langle ijk \rangle}}{\partial x_k} &= \int \hbar c_D \frac{k_{\langle i} k_{j \rangle}}{k} \xi \, d^3 k \end{aligned} \quad (4.6)$$

The first equations in the hierarchy of momentum equations (4.6) contain the phonon energy density e_{ph} and the heat flux $q_i = c_{\text{D}}^2 p_i$, given by

$$e_{\text{ph}} = \int \hbar c_{\text{D}} k f d^3k \quad \text{and} \quad (4.7)$$

$$q_i = c_{\text{D}}^2 \int \hbar k_i f d^3k \quad . \quad (4.8)$$

The momentum flux $N_{ij} = e_{\text{ph}}/3 \delta_{ij} + N_{\langle ij \rangle}$ includes the phonon energy density e_{ph} , so that the components of the deviatoric part

$$N_{\langle ij \rangle} = \int \hbar c_{\text{D}} \frac{k_{\langle i} k_{j \rangle}}{k} f d^3k \quad (4.9)$$

extend the thermodynamic variable space $(e_{\text{ph}}, q_i, N_{\langle ij \rangle})$ of a pure phonon gas in a nine-field theory.

In order to close the system of momentum equations (4.6), we expand the phase density f around a non-equilibrium state which is defined through the nine momentum $(e_{\text{ph}}, q_i, N_{\langle ij \rangle})$. For small deviation from equilibrium, the phase density assumes the form

$$f = f_{\text{E}} - \left[\frac{3}{4} \frac{q_i}{c_{\text{D}} e_{\text{ph}}} k_i + \frac{15}{8} \frac{N_{\langle ij \rangle}}{e_{\text{ph}}} \frac{k_{\langle i} k_{j \rangle}}{k} \right] \frac{\partial f_{\text{E}}}{\partial k} \quad , \quad (4.10)$$

where the phase density in equilibrium is given by

$$f_{\text{E}} = \frac{3}{(2\pi)^3} \frac{1}{\exp\left(\frac{\hbar c_{\text{D}} k}{k_{\text{B}} T}\right) - 1} \quad . \quad (4.11)$$

Making use of the phase density (4.10), the highest momentum $M_{\langle ijk \rangle}$ appearing in the momentum equations vanishes as expected in a linear theory.

In Callaway's relaxation time approximation the collision term ξ is divided into two parts,

$$\xi = -\frac{1}{\tau_{\text{R}}}(f - f_{\text{E}}) - \frac{1}{\tau_{\text{N}}}(f - f_{\text{N}}) \quad , \quad (4.12)$$

where τ_R is the relaxation time of resistive scattering processes which do not conserve phonon momentum and which tend to push the phonon gas back to the equilibrium f_E . The relaxation time τ_N is the mean time of free flight of phonons in normal scattering processes. These momentum conservation processes attempt to force the phonon gas to a non-equilibrium state, in which the phase density f_N takes the form (4.10) with $N_{\langle ij \rangle} = 0$.

By using both the relaxation time approximation (4.12) and the linear phase density (4.10), the field equations for the phonon gas variables ($e_{\text{ph}}, q_i, N_{\langle ij \rangle}$) can be calculated from

$$\begin{aligned} \frac{\partial e_{\text{ph}}}{\partial t} + \frac{\partial q_i}{\partial x_i} &= 0 \\ \frac{\partial q_i}{\partial t} + \frac{c_D^2}{3} \frac{\partial e_{\text{ph}}}{\partial x_i} + c_D^2 \frac{\partial N_{\langle ij \rangle}}{\partial x_j} &= -\frac{1}{\tau_R} q_i \\ \frac{\partial N_{\langle ij \rangle}}{\partial t} + \frac{1}{5} \left(\frac{\partial q_i}{\partial x_j} + \frac{\partial q_j}{\partial x_i} - \frac{2}{3} \frac{\partial q_k}{\partial x_k} \delta_{ij} \right) &= -\left(\frac{1}{\tau_R} + \frac{1}{\tau_N} \right) N_{\langle ij \rangle} \quad . \end{aligned} \quad (4.13)$$

The first equation of (4.13) for the phonon energy density is a conservation law in a pure phonon gas. This follows from the conservation of the energy in normal and resistive scattering processes. As the non-equilibrium part of the phase density (4.10) does not contribute to the momentum (4.7), the phonon energy density is obtained directly from the phase density in equilibrium (4.11). Thus one finds the well known formula

$$e_{\text{ph}} = \frac{4\pi^5}{5} \frac{k_B^4}{h^3 c_D^3} T^4 \quad . \quad (4.14)$$

Consequently, the phonon energy density e_{ph} is expressed in terms of the measurable quantity temperature.

In consideration of n additional localized excitations in a crystal, the thermodynamic variable space of a phonon gas ($T, q_i, N_{\langle ij \rangle}$) has to be extended to the energy densities e_ν ($\nu = 1, 2, \dots, n$). In the relaxation time approximation the energy balance equations for these localized excitations reads

$$\frac{\partial e_\nu}{\partial t} = -\frac{1}{\tau_\nu^R} (e_\nu - e_\nu^E) \quad . \quad (4.15)$$

The relaxation time τ_ν^{R} characterizes the time needed for a system of excitation ν to reach equilibrium with the phonon gas. For small deviation $\tilde{T} = T - T_{\text{R}}$ from a reference temperature T_{R} , the energy density of excitation in equilibrium e_ν^{E} can be expanded,

$$e_\nu^{\text{E}}(T) = e_\nu^{\text{E}}(T_{\text{R}}) + c_\nu^{\text{R}} \tilde{T} \quad , \quad (4.16)$$

where the specific heat of excitation ν , c_ν^{R} , is defined as the temperature derivative of the energy density e_ν^{E} in equilibrium at T_{R} . For the deviation of the energy density e_ν^{E} from its equilibrium value at reference temperature, $\tilde{e}_\nu = e_\nu - e_\nu^{\text{E}}(T_{\text{R}})$, it follows from (4.15)

$$\frac{\partial \tilde{e}_\nu}{\partial t} = -\frac{1}{\tau_\nu^{\text{R}}} \left(\tilde{e}_\nu - c_\nu^{\text{R}} \tilde{T} \right) \quad . \quad (4.17)$$

The linear field equations for the 9 plus n variables (\tilde{T} , q_i , $N_{\langle ij \rangle}$, \tilde{e}_ν) describing the thermal transport in a dielectric crystal with localized (magnetic) excitations at low temperature are given by

$$\begin{aligned} c_{\text{ph}}^{\text{R}} \frac{\partial \tilde{T}}{\partial t} + \frac{\partial q_i}{\partial x_i} &= \sum_\nu \frac{1}{\tau_\nu^{\text{R}}} \left(\tilde{e}_\nu - c_\nu^{\text{R}} \tilde{T} \right) \\ \frac{\partial q_i}{\partial t} + \frac{c_{\text{D}}^2 c_{\text{ph}}^{\text{R}}}{3} \frac{\partial \tilde{T}}{\partial x_i} + c_{\text{D}}^2 \frac{\partial N_{\langle ij \rangle}}{\partial x_j} &= - \left(\frac{1}{\tau_{\text{R}}^{\text{R}}} + \sum_\nu \frac{1}{\tau_\nu^{\text{R}}} \right) q_i \\ \frac{\partial N_{\langle ij \rangle}}{\partial t} + \frac{1}{5} \left(\frac{\partial q_i}{\partial x_j} + \frac{\partial q_j}{\partial x_i} - \frac{2}{3} \frac{\partial q_k}{\partial x_k} \delta_{ij} \right) &= - \left(\frac{1}{\tau_{\text{R}}^{\text{R}}} + \frac{1}{\tau_{\text{N}}^{\text{R}}} + \sum_\nu \frac{1}{\tau_\nu^{\text{R}}} \right) N_{\langle ij \rangle} \\ \frac{\partial \tilde{e}_\nu}{\partial t} &= -\frac{1}{\tau_\nu^{\text{R}}} \left(\tilde{e}_\nu - c_\nu^{\text{R}} \tilde{T} \right) \quad . \end{aligned} \quad (4.18)$$

The system of field equations (4.18) provides the basis for the interpretation of our heat transport measurements on $\text{Dy}_2\text{Ti}_2\text{O}_7$ at low temperatures:

- non-stationary heat flow into (and out of) a thin plate \rightarrow specific heat $c(T)$,
- stationary heat flow along a long rod \rightarrow thermal conductivity $\kappa(T)$,
- non-stationary heat flow along a long rod \rightarrow ballistic and/or diffusive transport phenomena.

Chapter 5

Measurements of Thermal Properties based on TFT Concept

With our present work we have studied heat relaxation and transport by measurements of the heat capacity, the thermal conductivity and heat pulse propagation on an isotopic high purity and crystallographic high-quality single crystal of $\text{Dy}_2\text{Ti}_2\text{O}_7$. This crystal was grown as a 5 cm long slab along the crystallographic [110]-direction with cross-section of about (3×2.5) mm². The measurements have been performed in a temperature range from 0.3 K to 30 K and magnetic field from 0 T to 1.5 T at the Magnetic Laboratory within the HZB neutron scattering facility. The heat capacity (of a small cut-off sliced sample with mass $m = 4.24$ mg and orientation [110] parallel to magnetic field) was measured with an in-house developed apparatus designed for the relaxation method operating with heat flow and heat pulse technique as well [Kie04]. For the thermal transport measurements on the 5 cm long slab with orientation [110] parallel to magnetic field, short-time thermometry and heater technique has been developed using electronic data acquisition up to 100 μs time resolution. For both type of measurements, two liquid helium based cryomagnets have been used equipped with sorption pumped ^3He -cryostat inserts [Oxf].

With respect to the [111] direction, the pyrochlore lattice consists of stacked triangular and Kagomé sub-lattices. However, in a magnetic field $B < 0.4$ T, the dysprosium spins arrange to the disordered ice state in the Kagomé lattice, only. With a small magnetic field, the ice-rule-breaking tetrahedrons align along [111] representing the magnetic monopoles [Kad09].

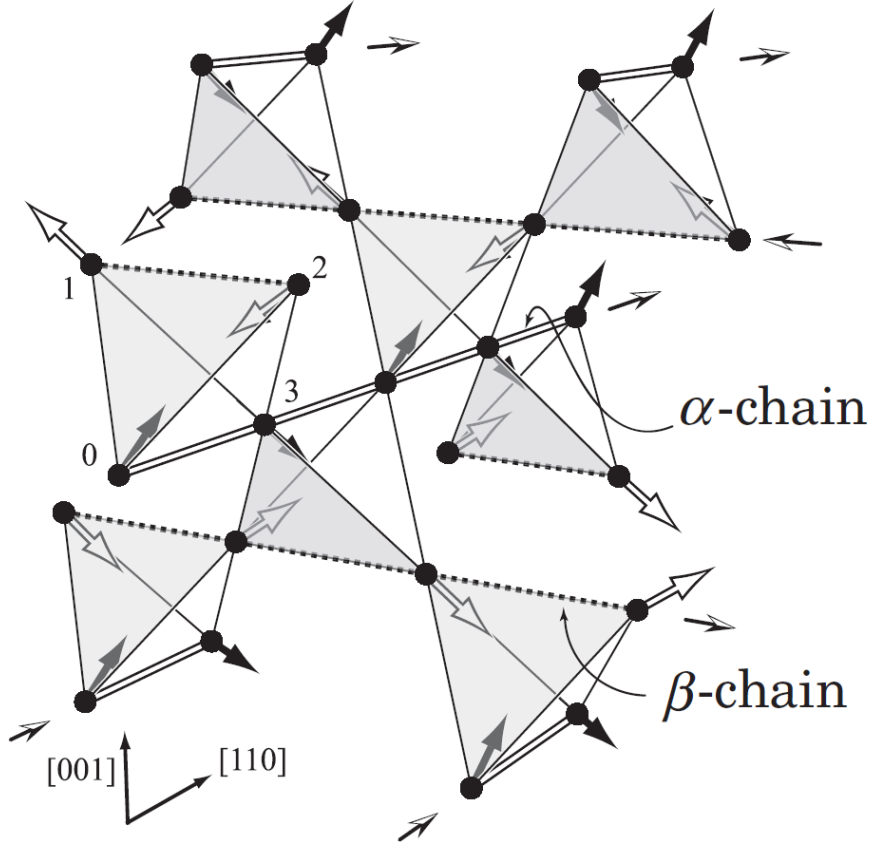


Figure 5.1: Schematic plot of the pyrochlore lattice. Magnetic dysprosium ions are located at each vertex of the tetrahedra. Under the [110] magnetic field, the system is divided into two sets of spin chains, namely, α -chain (double line) and β -chain (dotted line). The [110] magnetic field affects spins only on α -chains. (Reproduced from Yoshida et al. [Yos04].)

Due to the long rod-shaped geometry of our single crystalline sample, our study on thermal transport was restricted to the [110] direction where the density of magnetic monopoles cannot be controlled with magnetic field such as in perfect Kagomé lattice. The first heat capacity measurements on $\text{Dy}_2\text{Ti}_2\text{O}_7$ in magnetic field along [110] orientation [Hig02; Hir03] have revealed that the dysprosium spins can be considered to form two orthogonal sets of chains, parallel and perpendicular to the field direction, called α -chains and β -chains, respectively [Fen02] (see figure 5.1). Whereas the α -chains contribute to a Zeeman-shifted magnetic field dependent heat capacity, the β -chains exhibit a first-order transition at $B \approx 0.4$ T into a mixed α -ferromagnetic and β -antiferromagnetic (α -F & β -AF) ordered phase [Yos04; Ruf05].

In figure 5.2 we show the magnetic field - temperature phase diagram for $B \parallel [110]$ according to Yoshida et al. [Yos04] where $c_{\text{mag}}(T, B)$ data have been calculated

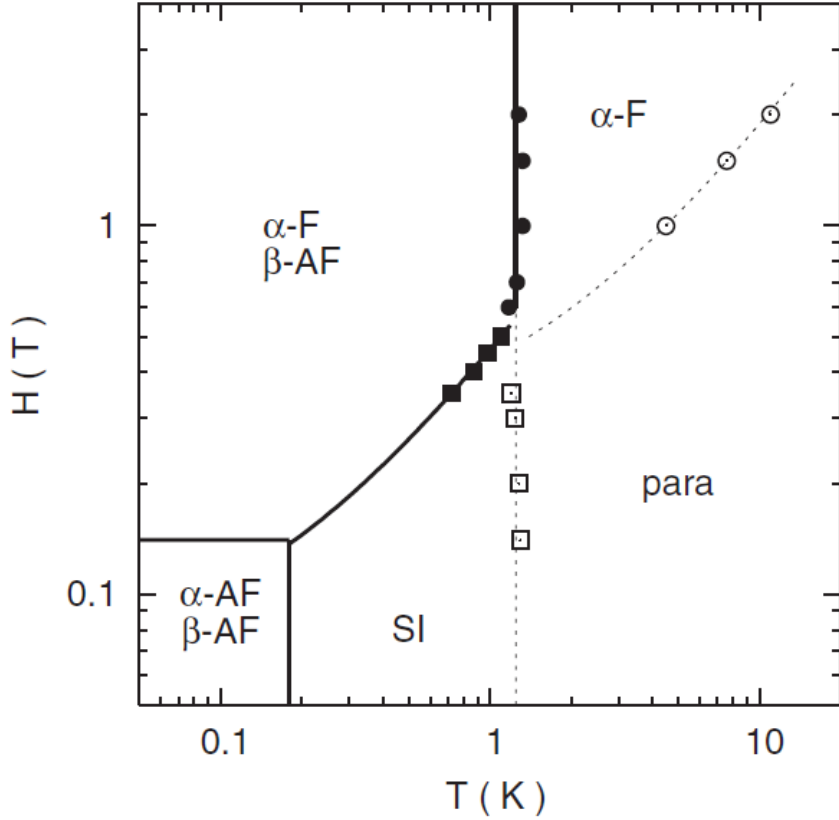


Figure 5.2: Magnetic field - temperature phase diagram for $B \parallel [110]$ according to $c_{\text{mag}}(T, B)$ data calculated with single spin flip Monte-Carlo simulations on system size of up to 5488 spins. Full data points and solid lines show first-order phase transitions into ferromagnetic (F) and anti-ferromagnetic (AF) spin structures. Open data points and dotted lines indicate crossover from paramagnetic (para) to spin ice (SI) and to field-ordered ferromagnetism (F), respectively. ‘ α ’ denote field coupled spin chains parallel to $[110]$ direction; ‘ β ’ denote field independent spin chains perpendicular to magnetic field [Hir03; Fen02]. (Reproduced from Yoshida et al. [Yos04].)

from Monte-Carlo simulations, in excellent agreement to the experimental data by Hiroi et al.. From the phase diagram it has been concluded that for small magnetic fields below 0.4 T, and in a temperature range $0.2 \text{ K} \lesssim T \lesssim 1.2 \text{ K}$, spin ice disorder exists. With stronger field, but still below $\sim 1.2 \text{ K}$, the spin ice state vanishes as, in a $[110]$ magnetic field, α - and β -chains arrange to ordered magnetic phases.

Given the so far published results on the heat capacity $c_{\text{mag}}(T, B \parallel [110])$ in the spin-ice regime we found it important to study the thermal properties of $\text{Dy}_2\text{Ti}_2\text{O}_7$ under a unique thermodynamic conception as presented previously in chapter 4. So it was necessary to arrange our measurement techniques accordingly to the various initial and

boundary conditions on the sample crystal which would allow us to solve the set of differential equations in terms of the temperature response $\tilde{T}(x, t)$ measured. In a thermal conductivity measurement, due to steady-state conditions, the resulting thermal conductivity $\kappa(T, B)$ can be directly analysed in terms of phonon scattering theory. However, heat relaxation and heat pulse propagation are transient measurements where the analysis is only possible by including a number of model parameters like addenda capacities and their thermal boundary resistances, defects and impurities in the sample, crystallographic alignment to magnetic field and demagnetization effects in the sample volume.

5.1 Measurement of specific heat

5.1.1 Set-up and data evaluation

The heat capacity C of a solid body in a magnetic field is defined as the derivative of its internal energy $U(T, \mathbf{F}, \mathbf{B})$ with respect to the temperature T at constant values of the deformation gradient \mathbf{F} (or volume $V \propto \det \mathbf{F}$) and the magnetic flux density \mathbf{B} . In measurements using the relaxation method, the heat capacity is derived from thermodynamic modelling of the whole thermal response to an applied heating power $\dot{Q}_s(t)$. In the case that the measurement time is long compared to the internal thermal diffusion time of the sample, the thermal relaxation can be described by uniform fields of the thermodynamic variables. This requirement can be satisfied by using thin samples and a proper conductance K_R of the thermal link between sample and bath at the constant reference temperature T_R . Neglecting spatial variations of the thermodynamic variables, the field equations (4.18) decouple into a set of partial energy equations (for e_{ph} and e_ν) and rate equations for both the heat flux \mathbf{q} and the deviatoric part of the momentum flux \mathbf{N} . The solution of the partial energy equations then describes the homogeneous thermodynamic process of thermal relaxation in insulating crystals including localized (magnetic) excitations. It must be pointed out, however, that in thermal relaxation experiments the temperature response $\tilde{T}_{\text{ch}} = T_{\text{ch}} - T_R$ is recorded by a chip thermometer. The chip thermometer and the heater generating the heat supply $\dot{Q}_s(t)$ are located on the sapphire calorimeter chip. In figure 5.3 the relaxation type calorimeter is sketched

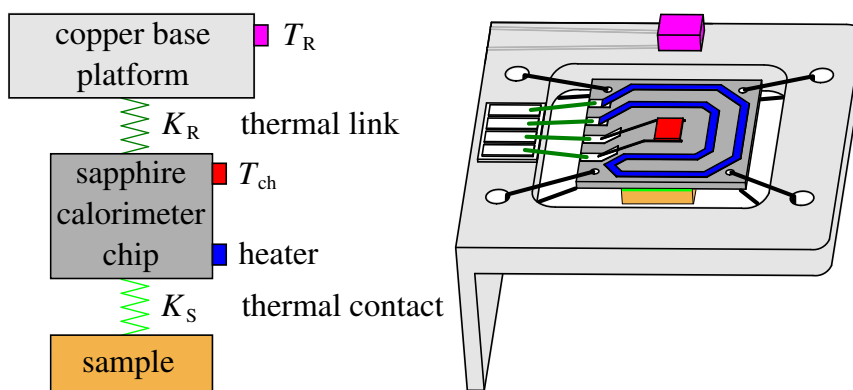


Figure 5.3: Schematic view onto the relaxation calorimeter (on right) used for the heat capacity measurements and the subsequent thermal model (on left) with the parameters (see colour code) used for the thermodynamic field theory calculations.

together with the thermal schematic model underlying the description of the heat flow in the calorimeter.

The home made calorimeter [Kie04] was mounted to the copper base of a ^3He sorption cryostat inserted in a 14.5 T cryomagnet [Oxf]. The copper base of the ^3He -cryostat could precisely be regulated providing the reference temperature in the range from 0.28 K to 30 K. A single crystalline sample of isotopically pure $\text{Dy}_2\text{Ti}_2\text{O}_7$ [Gri08] of slab size geometry (0.35 mm thickness, 2.55 mm length, 0.85 mm width and a mass of 4.24 mg) was attached onto the sapphire calorimeter chip using a small amount of Apiezon N grease of a mass less than 10 μg . The crystal's long slab axis (which is parallel to [110]) was aligned to the magnetic field axis by better than 1° . The calorimeter temperature T_{ch} is measured with a bare chip Cernox thermometer type BC 1030 [Lakb] which is glued onto the sapphire calorimeter chip. The calorimeter heater is a thin film heater made from sputtered gold. Due to the good thermal contact and the small masses, the thermal boundary resistance between thermometer and sapphire chip and heater and sapphire chip, respectively, has not been taken into account for the thermal model of the calorimeter. Thermometer and heater are electrically connected with four phosphor bronze wires [Laka] leading to four soldering pads thermally anchored at the copper mount. Four additional nylon strings give mechanical stability to the sapphire chip. The thermal model conductance $K_{\text{R}}(T_{\text{R}})$, i. e. the thermal link between sapphire chip and copper base, results from the metallic conductance of the four phosphor bronze wires only. As the sample is attached to the sapphire calorimeter chip, the thermal resistance provided by the grease layer and by the acoustic mismatch, as well, has been taken into account by the thermal model conductance $K_{\text{S}}(T_{\text{R}})$.

For $T_{\text{R}} < 0.5$ K the thermal resistance between the $\text{Dy}_2\text{Ti}_2\text{O}_7$ sample and the calorimeter chip, $R_{\text{S}} = 1/K_{\text{S}}$, increases rapidly and ends up with values which have a non-negligible influence on the analysis of the temperature profiles within the first seconds.

The temperature responses $\tilde{T}_{\text{ch}}(t)$, measured with the Cernox resistance thermometer, have been recorded by a lock-in electronic technique providing a minimum sampling time of 0.1 s and a rms-noise of 3 μK (at 0.3 K). The time response of the Cernox chip recorded with the electronic equipment was experimentally tested to be below 1 ms (for a temperature below 1 K) using pulsed laser light and glass fibre technique [Czt08].

With respect to the thermal model of the calorimeter as shown in figure 5.3, the linearized field equations, describing thermal relaxation of the uniform fields $(\tilde{T}(t), \tilde{T}_{\text{ch}}(t), \tilde{e}_\nu(t))$ in a relaxation calorimeter experiment, read now:

$$\begin{aligned}
c_{\text{ph}}^{\text{R}} \frac{d\tilde{T}}{dt} + \sum_{\nu} \frac{d\tilde{e}_\nu}{dt} + \frac{K_{\text{S}}}{V} (\tilde{T} - \tilde{T}_{\text{ch}}) &= 0 \\
C_{\text{ad}} \frac{d\tilde{T}_{\text{ch}}}{dt} + K_{\text{S}} (\tilde{T}_{\text{ch}} - \tilde{T}) + K_{\text{R}} \tilde{T} - \dot{Q}_{\text{S}} &= 0 \\
\frac{d\tilde{e}_\nu}{dt} + \frac{1}{\tau_\nu^{\text{R}}} (\tilde{e}_\nu - c_\nu^{\text{R}} \tilde{T}) &= 0 \quad .
\end{aligned} \tag{5.1}$$

Here, C_{ad} denotes the heat capacity of the calorimeter chip including the thin film heater, the thermometer and the amount of Apiezon N grease fixing the sample. The set of coupled ordinary differential equations (5.1) for the variables $\tilde{T}_{\text{ch}}(t)$, $\tilde{T}(t)$ and $\tilde{e}_\nu(t)$ can be solved numerically with the initial values $\tilde{T}_{\text{ch}}(0) = \tilde{T}(0) = \tilde{e}_\nu(0) = 0$.

For temperatures below 1.5 K the heat flow method was used for which the heating power $\dot{Q}_{\text{S}}(t)$ is a step function. The quasi-adiabatic heat pulse method was applied for temperatures above 1.2 K. In this calorimetric technique $\dot{Q}_{\text{S}}(t)$ is given by an rectangular pulse with a typical width of several seconds. In the temperature region between 1.2 K and 1.5 K the comparison between the results for the specific heat from both methods are in very good agreement. The relative deviation is smaller than approximately 1 %.

In figure 5.4 we present the measured temperature response $\tilde{T}_{\text{ch}}(t)$ at $T_{\text{R}} = 530$ mK where the non-exponential behaviour becomes obvious. Plotted on a log-time scale, the recorded data (open circles) exhibit no exponential saturation at $T_{\text{ch}}^{\text{max}}$ up to 300 s. Just for reference, the green line provides a comparison according to a single exponential temperature rise. The red line is a best fit to data calculated from equations (5.1) and taking into account only one magnetic subsystem ($n = 1$) with a relaxation time of about 4 s. It is obvious that additional magnetic subsystems with particularly shorter relaxation times (< 4 s) are required to describe the data at the outset of the temperature response. Best agreement between theory and experiment is gained assuming a number of three ($\nu = \alpha, \beta, \gamma$) magnetic excitations (see black line) with contributions c_α^{R} , c_β^{R} and c_γ^{R} to the magnetic heat capacity $C_{\text{mag}} = V(c_\alpha^{\text{R}} + c_\beta^{\text{R}} + c_\gamma^{\text{R}})$ and relaxation times τ_α^{R} , τ_β^{R} and τ_γ^{R} . The quality of the modelling according to the thermodynamic field theory is demonstrated in the upper section of figure 5.4 where the deviation of fit to data has

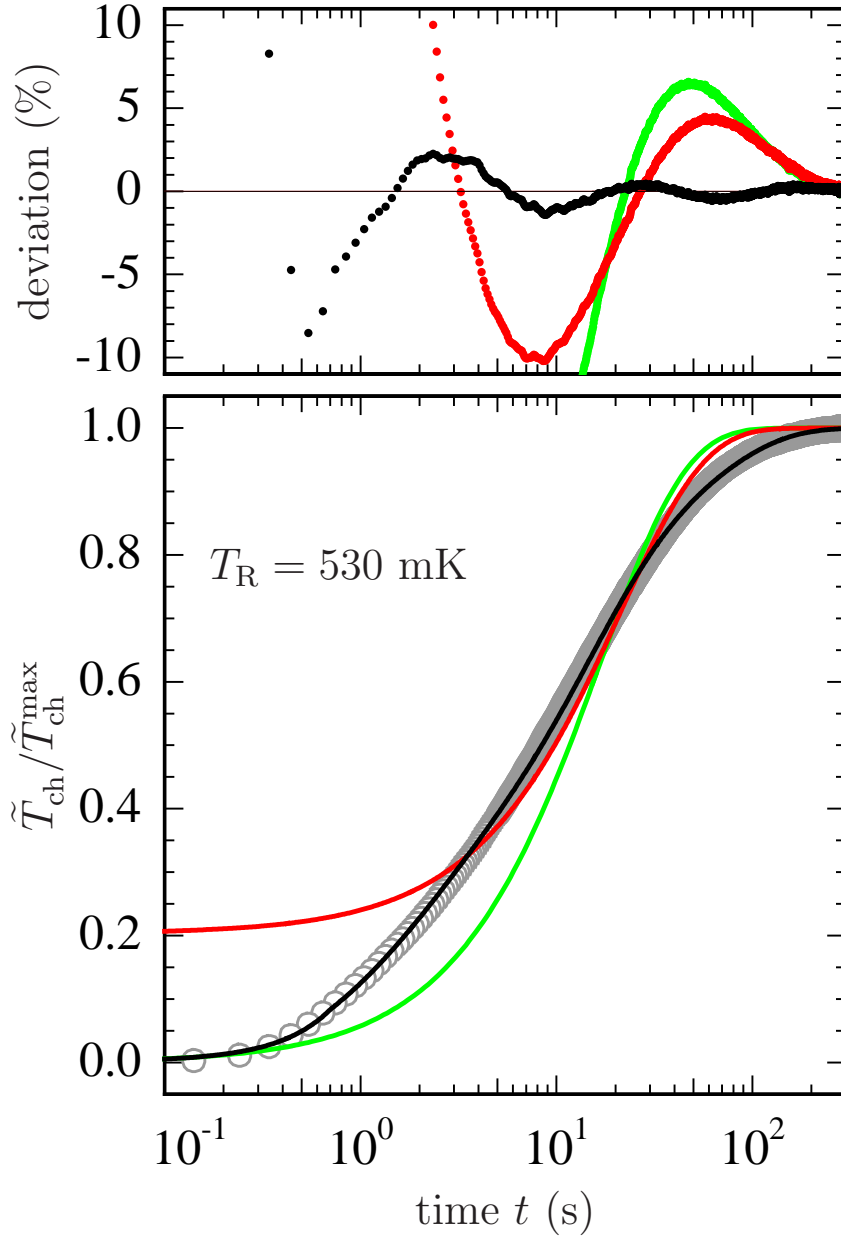


Figure 5.4: On log-time-scale, the temperature profile at $T_{\text{R}} = 530 \text{ mK}$ (as shown in figure 4.1) has been plotted with its initially recorded time resolution of 0.1 s (main panel, open circles). The green line denotes a fit to data according to a single exponential behaviour. The red line exhibits a fit to data according to thermodynamic field theory assuming one magnetic subsystem which couple to the heat carrying phonon bath with a relaxation time of about 4 s. The black line has been calculated according to the thermodynamic field theory (i. e. best fit to data) assuming three magnetic subsystems which individually couple to the heat carrying phonon bath. On top, the deviation fit to data has been plotted accordingly to the red, green and black lines in the main panel.

been plotted accordingly. For the temperature profile recorded in the time domain from 1 s to 300 s the agreement of theory and experiment is better than $\pm 2\%$. As has been pointed out earlier this experimental result has been observed at all temperatures from 0.3 K to about 1 K and for magnetic field up to 1.5 T (see figure 5.5).

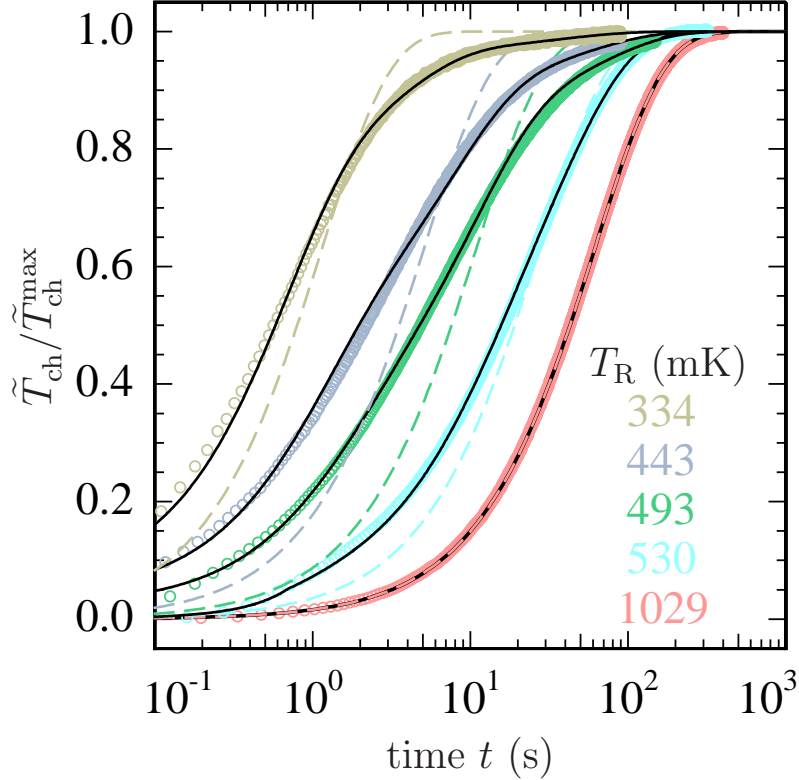


Figure 5.5: On log-time-scale, same temperature profiles as shown in figure 4.1 are plotted with their initially recorded time resolution of 0.1 s. Dashed lines are fits to data according to a single exponential behaviour. Full black lines are fits to data according to the thermodynamic field theory assuming a multitude of excitations which individually couple to the heat carrying phonon bath.

Because of the above mentioned time resolution of 0.1 s and the high thermal resistance between the $\text{Dy}_2\text{Ti}_2\text{O}_7$ sample and the calorimeter chip at temperatures below 0.4 K one can hardly distinguish whether the shape of the temperature profile is governed by a high thermal resistance or by a fast relaxation process. By having a finer time resolution one could directly measure the thermal resistance and due to that minimize the error of the measured values (specific heat and relaxation time) of the fast and the medium system. Better time resolution beyond 0.1 s is needed for a more accurate analysis of the recorded temperature profiles. By this reason we had to accept a relative high error

of 50% to 100% for evaluation of the faster relaxation time processes (τ_β^R , τ_γ^R) and the corresponding heat capacity values (c_β^R , c_γ^R).

For temperatures above 1 K, the deviations of $\tilde{T}_{\text{ch}}(t)$ from a single exponential behaviour is decreased due to the considerable shortening of relaxation times as temperature is increased.

By presenting our results on the heat capacity of $\text{Dy}_2\text{Ti}_2\text{O}_7$ below approximately 1 K, we are forced to distinguish between the three magnetic heat capacities c_α^R , c_β^R and c_γ^R and their related relaxation times τ_α^R , τ_β^R and τ_γ^R , respectively. For temperatures above approximately 1 K, we cannot distinguish between the different contributions, and thus, we present the classical unique heat capacity, only. However, due to the characteristic temperature and magnetic field dependences at low temperature we can identify the heat capacities in the overall temperature range from 0.3 K to 30 K. This will be presented and discussed in chapter 6.

5.1.2 Results on specific heat

In figure 5.6 we present the low magnetic field specific heat $c_{\text{m}\alpha} = V_{\text{mol}} c_\alpha^R$ (open yellow circles), $c_{\text{m}\beta} = V_{\text{mol}} c_\beta^R$ (open violet squares) and $c_{\text{m}\gamma} = V_{\text{mol}} c_\gamma^R$ (open magenta triangles) measured at magnetic field $B = 0$ T (top) and $B = 0.2$ T (bottom). V_{mol} here denotes the molar volume which is $78.14 \text{ cm}^3/\text{mol}$ for $\text{Dy}_2\text{Ti}_2\text{O}_7$. The insets show the related relaxation times τ_α^R and τ_β^R calculated according to thermodynamic field theory. The fast relaxation time τ_γ^R has been assumed to be much faster than the time resolution of our thermometry recording electronics. The full black circles depict the total specific heat c_{total} as determined from standard calorimeter technique. Below 2 K the lattice specific heat is negligible as $c_{\text{ph}} \lesssim 10^{-3} \cdot c_{\text{total}}$. Therefore for low temperatures the magnetic specific heat c_{mag} is almost equal to c_{total} . The open black circles denote $c_{\text{total}} \approx c_{\text{mag}} = c_{\text{m}\alpha} + c_{\text{m}\beta} + c_{\text{m}\gamma}$ where the three contributions are derived from thermodynamic field theory analysis of non-exponential temperature responses. As can be seen from the insets in figure 5.6, at temperatures above 0.7 K ($B = 0$ T) and above 0.9 K ($B = 0.2$ T) respectively, it is no more possible to distinguish between the three magnetic contributions.

In figure 5.7, we present the heat capacities $c_{\text{m}\beta}$ (open violet squares), $c_{\text{m}\gamma}$ (open magenta triangles) and c_{total} (black circles) for the higher magnetic fields $B = 0.5$ T – 1.5 T where

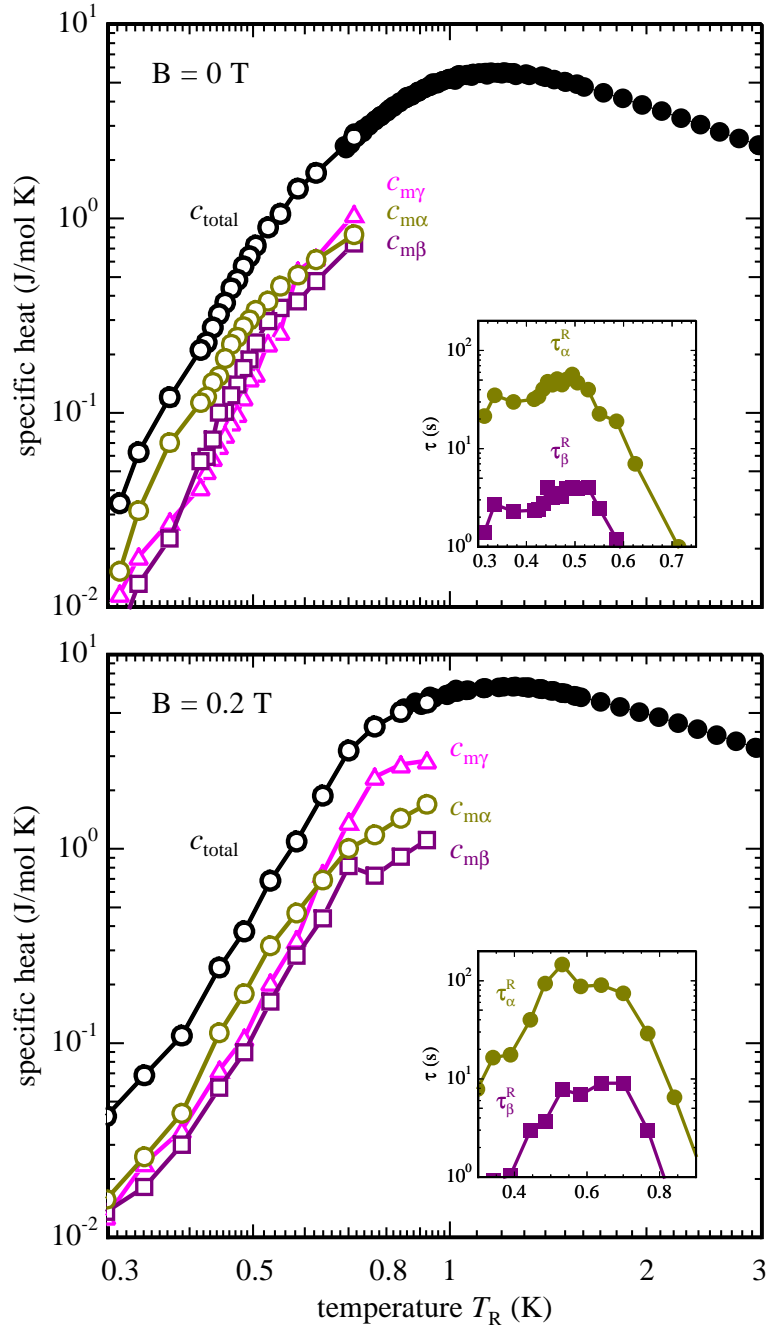


Figure 5.6: Specific heat for magnetic fields $B = 0 - 0.2$ T. Below approximately 0.8 K, open symbols show the individual magnetic specific heat contributions $c_{m\alpha}$, $c_{m\beta}$ and $c_{m\gamma}$ and their linear superposition $c_{\text{total}} \approx c_{\text{mag}} = c_{m\alpha} + c_{m\beta} + c_{m\gamma}$. The full black circles depict the total specific heat c_{total} as determined from standard calorimeter technique.

The insets show the related relaxation times according to thermodynamic field theory using equation (5.1). For $T \gtrsim 0.8$ K black full circles show the cross-over to a single magnetic subsystem behaviour as τ_{α}^R and τ_{β}^R decrease below the experimental time resolution of 0.1 s.

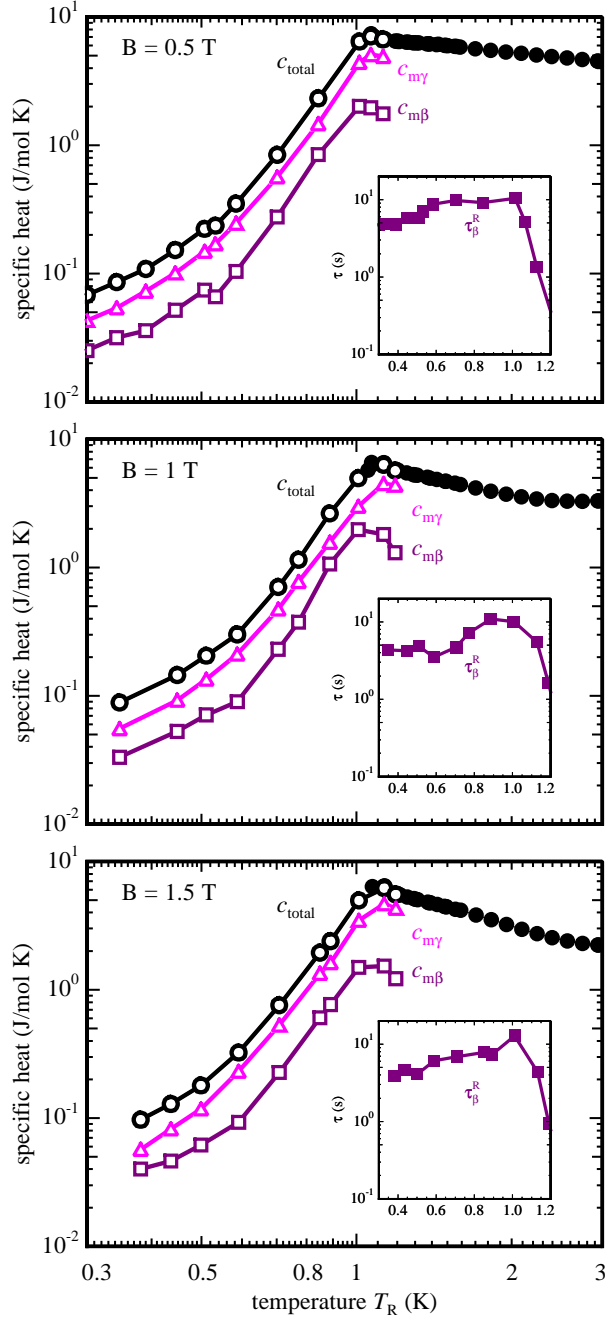


Figure 5.7: Specific heat for magnetic fields $B = 0.5 - 1.5$ T. Below approximately 1.2 K, open symbols show the individual magnetic specific heat contributions $c_{m\beta}$ and $c_{m\gamma}$ and their linear superposition $c_{\text{total}} \approx c_{\text{mag}} \approx c_{m\beta} + c_{m\gamma}$. The $c_{m\alpha}$ specific heat is Zeeman-shifted to higher temperatures by the magnetic field and therefore does not impact on our analysis.

The insets show the related relaxation times according to thermodynamic field theory using equation (5.1). For $T \gtrsim 1.2$ K black full circles show the cross-over to a single magnetic subsystem behaviour as τ_{β}^R decrease below the experimental time resolution of 0.1 s. At $T_c = 1.05$ K the individual contribution $c_{m\beta}$ and $c_{m\gamma}$ exhibit the first order phase transition.

at $T_c = 1.05$ K a first order phase transition into a ferromagnetic state is observed (see figure 5.2). Due to the Zeeman energy $\sim \mu B$ the contribution $c_{m\alpha}$ is no more observable (for model calculation see chapter 6). This is confirmed in the insets of figure 5.7 where only τ_β^R marks the β -excitation with a fairly constant value around 5 s. Again, as in the insets of figure 5.6, the fast relaxation time τ_γ^R is beyond the experimental resolution. For temperatures $T > T_c$, the analysis of the temperature profiles result in the specific heat c_{total} as shown by the full black circles.

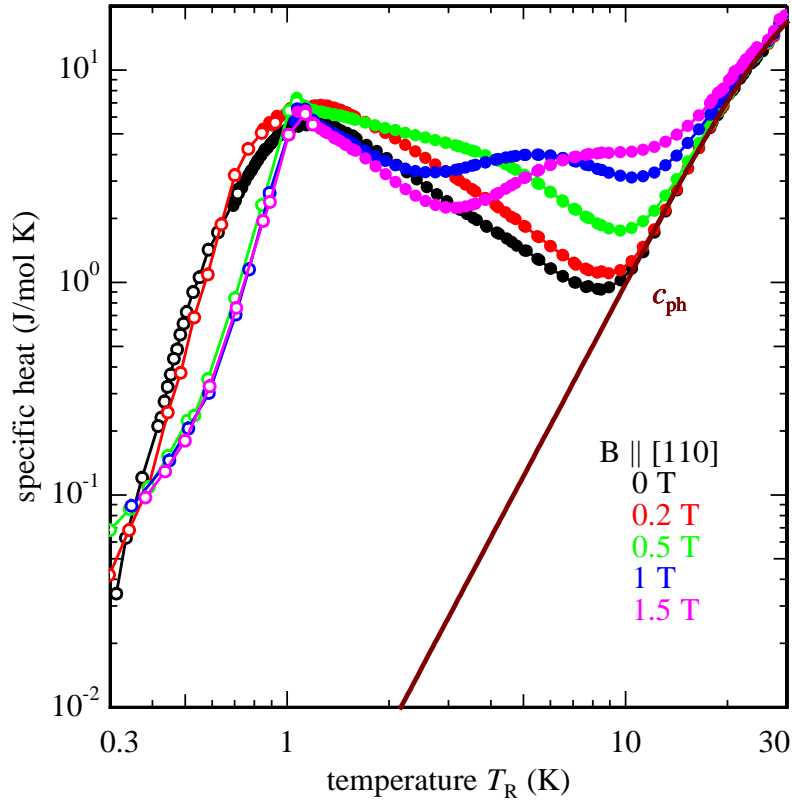


Figure 5.8: Specific heat of $\text{Dy}_2\text{Ti}_2\text{O}_7$ in the temperature range from 0.3 K to 30 K and for magnetic fields from 0 T to 1.5 T (parallel [110] axis). Full circles designate the data from (traditional) single-exponential temperature profile analysis. Open circles mark the calculated specific heat $c_{\text{total}} \approx c_{\text{mag}} = c_{m\alpha} + c_{m\beta} + c_{m\gamma}$ according to the thermodynamic field theory equation (5.1). The brown line denotes the phonon specific heat c_{ph} according to equation (6.2). The other full lines are guide for the eye, only. Note the different unique specific heat behaviour below 1 K for the spin ice phase ($0 \text{ T} \leq B \leq 0.2 \text{ T}$) and the ferromagnetic phase ($0.5 \text{ T} \leq B \leq 1.5 \text{ T}$, $T_R < T_c = 1.05 \text{ K}$)

In order to demonstrate the superposition principle $c_{\text{mag}} = c_{m\alpha} + c_{m\beta} + c_{m\gamma}$ which is a result from thermodynamic field theory calculation for $T \lesssim 1$ K, we show all specific heat data in figure 5.8. On a log-log scaling and in the overall measured temperature

range from 0.3 K to 30 K, the open circles mark $c_{\text{total}} \approx c_{\text{mag}}$ (calculated according to thermodynamic field theory using equation (5.1)); whereas the full circles result from the traditional analysis of genuine single-exponential temperature profiles. As can be seen, there is a perfect match of the specific heat data sets for all magnetic field measurements. Also, it is shown that there is a significant difference on the temperature dependence of $c_{\text{total}}(T)$ for $\text{Dy}_2\text{Ti}_2\text{O}_7$ in the spin ice state and the ordered ferromagnetic phase. In both phases there are only minor differences in $c_{\text{total}}(T, B)$ exhibiting different unique low temperature behaviour below 1 K. A more detailed discussion will be presented in chapter 6.

One difficulty is that one can interpret thermal drifts and instabilities of the thermal bath as slow internal relaxation processes. To prevent this the temperature of the thermal bath T_{R} should be monitored and taken into account for the analysis. In the present analysis the thermal drift of the bath was computationally eliminated by addition of the “up” and the “down” part of the temperature profile. Of course this could result in errors if not only a linear drift is present.

The heat flow method of the CM-14.5T specific heat apparatus is optimized to measure one time constant which has the same order of magnitude such as the measurement time. In the case of $\text{Dy}_2\text{Ti}_2\text{O}_7$ there exists slow relaxation processes (time constants between approximately 10 s and 100 s) in the system. Therefore it follows that one has to measure for long times ($\approx 100 \dots 600$ s). Because of this the time resolution during the measurement is only about 0.1 s, so for further measurements we plan to improve this time resolution by using another Lock-In Amplifier and then repeat some of the measurements presented here. If it is possible to extend the time resolution to 1 ms and below this could allow us to measure the internal relaxation time constants up to temperatures where we can directly compare our results with those of Snyder et al. [Sny04].

5.2 Measurement of thermal conductivity

5.2.1 Set-up and data evaluation

The thermal conductivity was measured using the set-up for a “one heater & two thermometer” method [Poh82]. Enforcing one-dimensional heat flow, a long slab geometry is appropriate where a constant heater power \dot{Q} is applied to the top face of the crystal (at $x = 0$). The lower end of the crystal (at $x = L$) is thermally fixed to the thermal bath at temperature T_R . With two thermometers T_1 (at position $x_1 < L/2$) and T_2 (at position $x_2 > L/2$) the temperature gradient $\Delta T/\Delta x = (T_1 - T_2)/(x_1 - x_2)$ has to be measured accurately. The thermal conductivity is then determined by:

$$\kappa = -\frac{\dot{Q}}{A} \cdot \frac{\Delta x}{\Delta T} \quad . \quad (5.2)$$

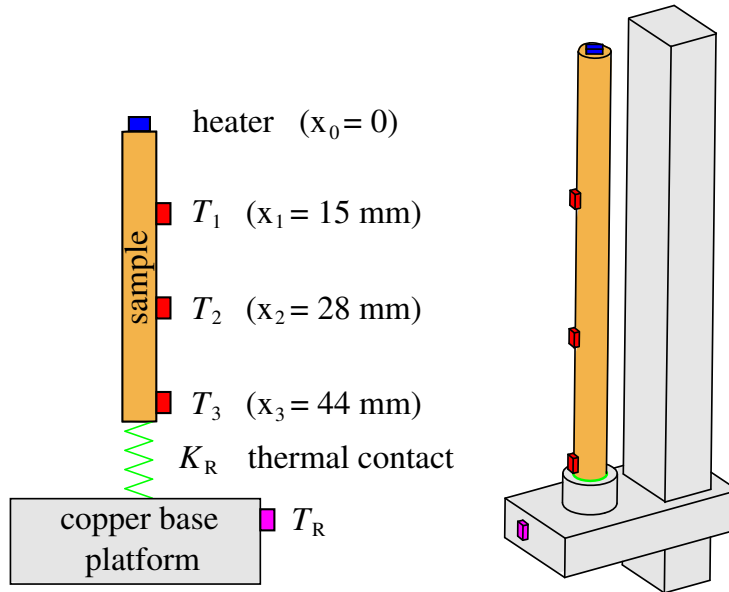


Figure 5.9: Schematic view of the set-up (on right) for the thermal conductivity measurements and the subsequent thermal model (on left) with the parameters (see colour code) used for the calculation of $\kappa(T_R)$ according to Fourier's law, equations (5.3) and (5.4).

In figure 5.9 our set-up for the measurement of the thermal conductivity $\kappa(T, B)$ is sketched together with the schematic thermal model. The sample was mounted to the copper base of a ^3He sorption cryostat inserted in a 8 T cryomagnet [Oxf]. The

copper base of the ^3He -cryostat could precisely be regulated providing the reference temperature $T_{\text{R}} = 0.3 \text{ K} \dots 30 \text{ K}$. The $\text{Dy}_2\text{Ti}_2\text{O}_7$ sample has been grown with enriched ^{162}Dy (with 95-98 % ^{162}Dy) to a rod shaped single crystal of a length of $L = 50 \text{ mm}$; it was grown along the $[110]$ direction shaped with an about circular cross section of diameter $\approx 3.1 \text{ mm}$ (cross section area $A = 7.6 \text{ mm}^2$) [Gri08]. The crystal's long $[110]$ axis was aligned to the magnetic field axis to better than 1° . The lower end of the crystal was glued into a matching hole of the copper base platform using GE-7031 varnish. The thermal resistance provided by the varnish layer and by the acoustic mismatch between the dielectric crystal and the copper metal, as well, has been taken into account by a thermal model conductance $K_{\text{R}}(T_{\text{R}})$. On top of the crystal, a small SMD resistor ($\approx 2 \text{ k}\Omega$ at 0.5 K) was mounted (using super glue) providing an electrical heater driven by a programmable precision voltage source.

The temperatures T_1 and T_2 resulting from the stationary heat flow by the heater were measured with bare chip Cernox type BC 1030 [Lakb] thermometers, again superglued to the outer wall side of crystal at defined positions x_1 and x_2 ($\Delta x = 13 \text{ mm}$). Typical temperature gradients were about 5 % of the reference temperature T_{R} . The thermometers and the heater were electrically wired with NbTi twisted pair wires to the copper base platform, each wire having a length of approximately 100 mm to ensure low thermal conductance between crystal and thermal bath.

In the steady state technique, the temperature within the sample does not change with time and, subsequently, for stationary processes the linearized field equations (4.18) are reduced to the heat conservation $\text{div } q = 0$ and Fourier's law:

$$q_i = -\frac{c_{\text{D}}^2 c_{\text{ph}}^{\text{R}}}{3} \left(\frac{1}{\tau_{\text{R}}} + \sum_{\nu} \frac{1}{\tau_{\nu}^{\text{R}}} \right)^{-1} \frac{\partial \tilde{T}}{\partial x_i} . \quad (5.3)$$

For temperatures well below the Debye temperature of a crystal, equation (4.14) can be used to determine the specific heat of the phonons $c_{\text{ph}}^{\text{R}}(T_{\text{R}})$ and the thermal conductivity $\kappa(T_{\text{R}})$ is expressed in the form:

$$\kappa(T_{\text{R}}) = \frac{16\pi^5}{15} \frac{k_{\text{B}}^4}{h^3 c_{\text{D}}} \frac{T_{\text{R}}^3}{\frac{1}{\tau_{\text{R}}} + \sum_{\nu} \frac{1}{\tau_{\nu}^{\text{R}}}} . \quad (5.4)$$

The relaxation rates τ_{R}^{-1} of resistive scattering processes can be represented in the Debye-Callaway model [Cal59] by frequency-dependent relaxation times. Phonon normal processes with relaxation rate $(\tau_{\text{N}})^{-1} \ll (\tau_{\text{R}})^{-1}$ have not been taken into account. The relaxation time analysis of the thermal conductivity measurements will be presented in the chapter 6.

Due to the finite size of the Cernox thermometers (1 mm width) an error for distance Δx of about 4 % had to be accepted. Also, the variance in the cross section geometry along the length of the crystal produced an error of about 6 %. In total, the error to the absolute values of our thermal conductivity measurement adds up to 10 %. A third Cernox thermometer T_3 was mounted to the crystal wall near to the thermal contact edge ($x_3 = 44$ mm) where the crystal was glued to the thermal bath. At stationary heat flow conditions, the residual temperature difference $\Delta T_{\text{R}} = T_3 - T_{\text{R}}$ was observed to be negligible as $\Delta T_{\text{R}}/T_{\text{R}}$ was smaller ≈ 1 % in the overall temperature range $T_{\text{R}} = 0.3 \text{ K} \dots 30 \text{ K}$. However, in our heat pulse experiments, the small temperature differences between crystal and copper base had to be taken into account as the thermal model conductance $K_{\text{R}}(T_{\text{R}})$ was needed for the analysis of the time-dependent temperature responses $\tilde{T}(x_1, t)$ and $\tilde{T}(x_2, t)$, respectively (see section 5.3).

5.2.2 Results on thermal conductivity

In figure 5.10 we present the first results from thermal conductivity measurements with heat flow and magnetic field parallel to the [110] axis. The temperature dependence of the thermal conductivity exhibits the typical signature of a high quality crystal with a high peak value of 0.1 W/cmK at $T_{\text{R}} = 12$ K. In the overall studied temperature range from 0.3 K to 30 K a surprisingly weak dependence on the magnetic field strength was observed. Within the experimental error of ± 10 % on the relative values of $\kappa(T_{\text{R}}, B)$ the thermal conductivity at 1 K decreased only about $(\kappa(0 \text{ T}) - \kappa(1.5 \text{ T}))/\kappa(0 \text{ T}) \approx 25$ %. At temperatures above 10 K no magnetic field dependency was observed. Below 2 K and for all magnetic fields measured, a temperature dependence $\kappa \propto T^2$ is dominant. A detailed discussion on likely relaxation scattering processes to the phonons will be presented in chapter 6.

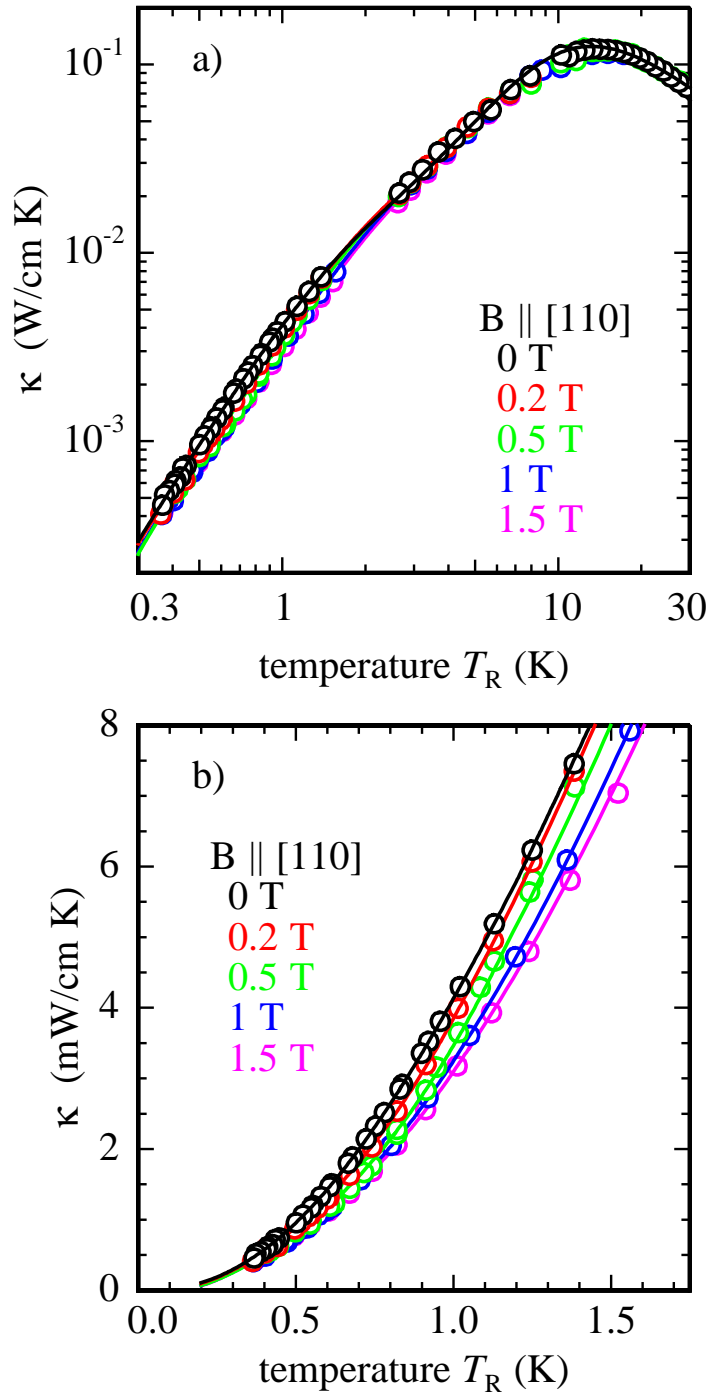


Figure 5.10: (a) Thermal conductivity of $\text{Dy}_2\text{Ti}_2\text{O}_7$ in the temperature range from 0.3 K to 30 K and for magnetic fields from 0 T to 1.5 T (magnetic field and heat flow parallel to [110] axis). Note a $\kappa \propto T^2$ dependence below 2 K where a weak dependence on the magnetic field up to 1.5 T is obvious. (b) Low temperature detail of the thermal conductivity of $\text{Dy}_2\text{Ti}_2\text{O}_7$.

5.3 Measurement of heat pulse transport

Heat pulse transport measurements have been performed using the same experimental set-up as for the thermal conductivity measurements (see figure 5.9). In a temperature range from 0.3 K to 4 K, short thermal pulses of width $\Delta t_H = 1$ ms up to 5 ms have been generated by energizing the SMD resistance heater with a programmable precision voltage source. On a time scale from 1 ms up to 1000 s, the subsequent temperature responses $\tilde{T}(x, t) = T(x, t) - T(x, t = 0)$ have been recorded by thermometer T_1 and T_2 using a DC – 100 kHz pre-amplifier and signal averaging electronics. As mentioned above, the conductance K_R of the thermal contact to the bath at $x = L$ was determined by measuring the sample base temperature T_3 with respect to the reference temperature T_R . In order to justify a linearized theoretical description of the experiments, the maximum temperature rise T_{\max} was limited to $(T_{\max} - T_R)/T_R \leq 5\%$ by adjusting the heat pulse energy $Q = \dot{Q}_S \cdot \Delta t_H$ appropriately.

On the basis of thermodynamic field theory equation (4.18) provide the complete description for non-stationary heat transport under inhomogeneous spatial conditions in a volume material. According to the experimental set-up (figure 5.9) one-dimensional heat flow can be assumed. In this one-dimensional, rotationally symmetric geometry, all thermodynamic variables are functions of time and a single spatial coordinate $x := x_1$. The symmetric traceless tensor $N_{\langle ij \rangle}$ specializes to $N_{11} = -2N_{22} = -2N_{33}$ and contains no off-diagonal components. Introducing the notation $N := N_{11}$ and $q := q_1$ the one-dimensional field equations (4.18) are reduced to the $3+\nu$ equations for $(\tilde{T}, q, N, \tilde{e}_\nu)$:

$$\begin{aligned}
 c_{\text{ph}}^{\text{R}} \frac{\partial \tilde{T}}{\partial t} + \frac{\partial q}{\partial x} &= \sum_{\nu} \frac{1}{\tau_{\nu}^{\text{R}}} (\tilde{e}_{\nu} - c_{\nu}^{\text{R}} \tilde{T}) \\
 \frac{\partial q}{\partial t} + \frac{c_{\text{D}}^2 c_{\text{ph}}^{\text{R}}}{3} \frac{\partial \tilde{T}}{\partial x} + c_{\text{D}}^2 \frac{\partial N}{\partial x} &= - \left(\frac{1}{\tau_{\text{R}}^{\text{R}}} + \sum_{\nu} \frac{1}{\tau_{\nu}^{\text{R}}} \right) q \\
 \frac{\partial N}{\partial t} + \frac{4}{15} c_{\text{D}}^2 \frac{\partial q}{\partial x} &= - \left(\frac{1}{\tau_{\text{R}}^{\text{R}}} + \frac{1}{\tau_{\text{N}}^{\text{R}}} + \sum_{\nu} \frac{1}{\tau_{\nu}^{\text{R}}} \right) N \\
 \frac{\partial \tilde{e}_{\nu}}{\partial t} &= - \frac{1}{\tau_{\nu}^{\text{R}}} (\tilde{e}_{\nu} - c_{\nu}^{\text{R}} \tilde{T}) \quad .
 \end{aligned} \tag{5.5}$$

The system (5.5) is a linear system of partial differential equations, which can be solved numerically for given initial and boundary conditions. For the solution of the problem we take into account the initial conditions $\tilde{T}(x, 0) = q(x, 0) = N(x, 0) = \tilde{e}_{\nu}(x, 0) = 0$ and

the boundary conditions $\tilde{T}(L, t) = N(L, t) = 0$. This problem, for which the additional boundary condition is given by, $q(0, t) = \dot{Q}_S/A$ for $0 \leq t \leq \Delta t_H$ and $q(0, t) = 0$ otherwise, is termed the heat pulse problem.

It could be assumed that the numerical solution of the heat pulse problem can be obtained with basically no other parameters, appearing in the field equations (5.5), than those we have already fixed from the analysis of specific heat and thermal conductivity experiments. From this point of view, the analysis of heat pulse propagation constitutes a check of both the thermodynamic modelling of heat transport in $\text{Dy}_2\text{Ti}_2\text{O}_7$ and the preassigned data of specific heat and thermal conductivity.

For sufficiently small values of relaxation times τ_ν^R the energy densities of magnetic excitations will depend on temperature according to the relationship $\tilde{e}_\nu = c_\nu^R \tilde{T}$. In this case, i. e. for $T \gtrsim 1$ K, our thermal model simplifies to a system of propagating phonons scattered by paramagnetic magnetic centres and equations (5.5) reduce to the well-known one-dimensional diffusion of heat according to Fourier theory [Car59; Kru73]. For a slab of certain length the temperature profiles $\tilde{T}(x, t)$ are therefore described by:

$$\tilde{T}(x, t) = \frac{Q}{\rho A c \sqrt{\pi D t}} e^{-\frac{x^2}{4Dt}} \cdot \left[1 + \sum_{n=-\infty}^{+\infty; n \neq 0} (-1)^n \exp\left(-\frac{n^2 L^2}{Dt} \left(1 - \frac{x}{nL}\right)\right) \right], \quad (5.6)$$

where ρ is the mass density, A the cross section area and L the length of the $\text{Dy}_2\text{Ti}_2\text{O}_7$ slab, respectively; D is the standard thermal diffusivity (see equation (4.4)) where the temperature dependence $D(T)$ is dominated solely by the competition between thermal conductivity and specific heat.

It must be pointed out, that the time resolution ($< 10^{-3}$ s) achieved in the heat pulse experiments is much better than that of the thermal relaxation experiments. Therefore, a comparison of the results obtained in both experiments is only valid on the same time scale. On the other hand, the better time resolution in heat pulse experiments permits us to investigate in detail the fast relaxation of magnetic excitations.

For $T_R = 1.1$ K, the measured temperature profile $\tilde{T}(x_1, t)$ has been plotted in figure 5.11 on linear (a) and logarithmic (b) time-scale, as well. The red line show the temperature profile calculated according to thermodynamic field theory, which is in time-domain from 1 ms to 100 s in perfect agreement with the measured temperature profile. As can be seen, the measured profile exhibits a complete agreement to standard

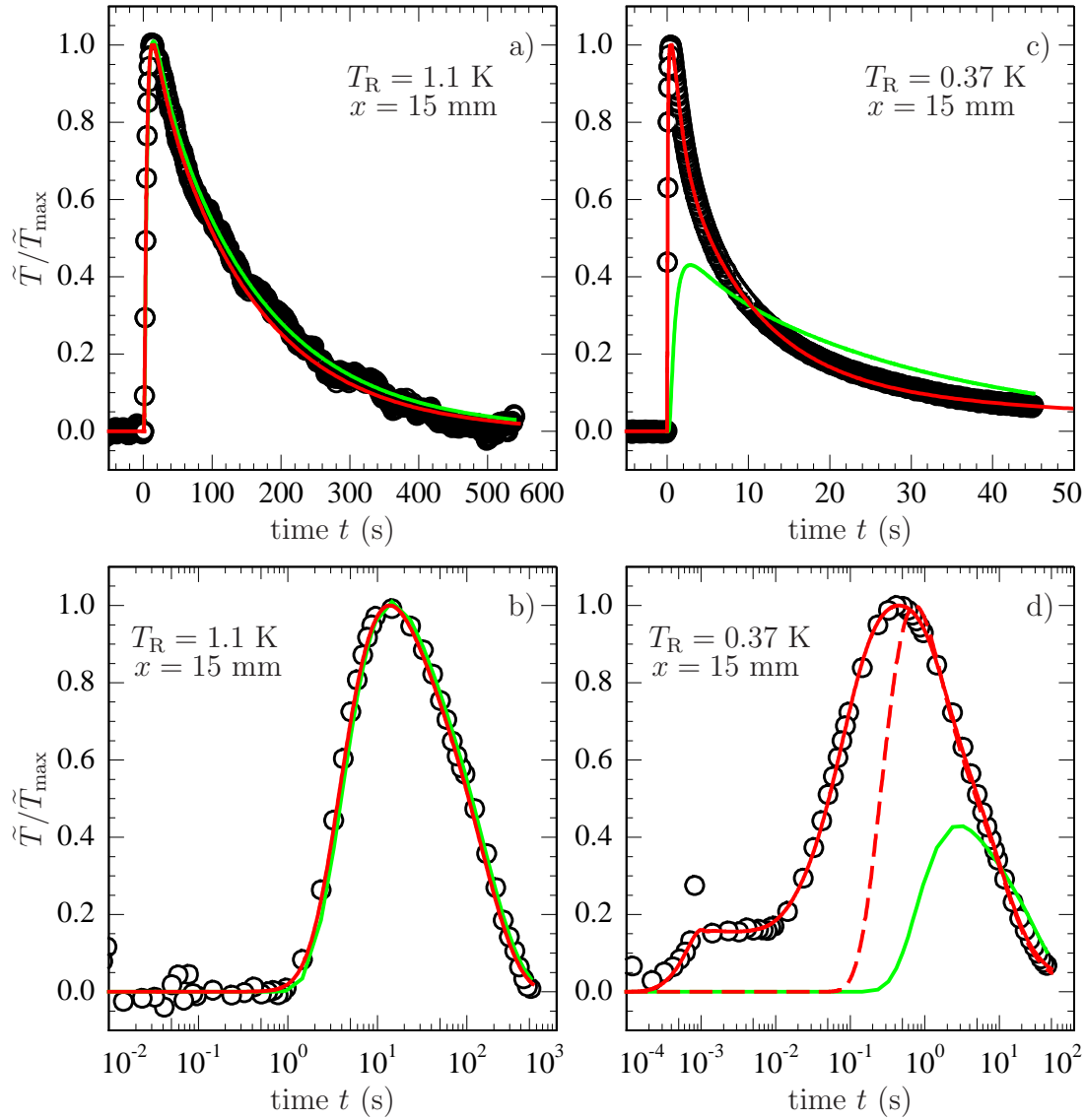


Figure 5.11: Temperature transients $\tilde{T}(x, t)$ after initial heat pulse of energy Q and width Δt_H at $t = 0$ for two different temperatures, $T_R = 1.1$ K (a),(b) and $T_R = 0.37$ K (c),(d).

The green lines show temperature profile calculated according to standard heat diffusion theory, equations (5.6) and (4.4). Parameters used for calculation are listed in table 5.1. The red lines show temperature profile calculated according to thermodynamic field theory.

(a), (b): At 1.1 K thermodynamic field theory and standard heat diffusion theory are in very good agreement with the measured temperature transients.

(c): At 0.37 K standard heat diffusion theory gives a completely wrong theoretical profile (green line).

(d): The temperature profile calculated according to thermodynamic field theory (α -, β - and γ -excitations) with the parameters from specific heat and thermal conductivity measurements (dashed red line) is correct for times greater than 1 s (see text). To describe the complete temperature profile with thermodynamic field theory in total 8 magnetic excitations are necessary with relaxation times in the range of 10^{-8} s to 50 s (full red line).

diffusion theory, according to equation (5.6) (green line), as well. $D(T_R)$ has been calculated from the heat capacity and thermal conductivity data at T_R (see chapter 6). Thus, the data of both the specific heat and the thermal conductivity which were obtained in the thermal relaxation and steady state heat transport measurements are in agreement with thermodynamic modelling of the heat pulse experiments. This is at least true for temperatures above 1 K.

With decreasing temperature, the measured temperature responses at short times more and more deviate from the exponential increase versus time. Below 1 K, in the spin ice regime, the non-stationary heat transport reflects the phonon scattering and the relaxation processes of the magnetic subsystems resulting in a balanced competition between a fast propagation and a slow transport of heat. In figure 5.11 the temperature profile $\tilde{T}(x_1, t)$ measured at $T_R = 0.37$ K has been plotted, again on linear (c) and logarithmic (d) time scale. For comparison the standard diffusion temperature response has been calculated from equation (5.6) (green line) using the data for $c_{\text{total}}(T_R)$ and $\kappa(T_R)$ (see chapter 6).

T_R (K)	\dot{Q}_S (mW)	Δt_H (ms)	Q (μJ)	κ (mW/cm K)	c_{total} (J/g K)	D (cm^2/s)
1.1	57	4.9	279	4.9	$10.13 \cdot 10^{-3}$	0.07
0.37	3.1	0.95	2.95	0.45	$0.22 \cdot 10^{-3}$	0.30

Table 5.1: Parameter of standard diffusion heat transport model (as displayed in figure 5.11) according to equations (5.6) and (4.4) with density of $\text{Dy}_2\text{Ti}_2\text{O}_7$ $\rho = 6.808$ g/cm^3 and cross section area of the sample $A = 7.6$ mm^2 .

For short times, i. e. $t < t_{\text{max}} = 5$ s, starting immediately after the initial heat pulse, the temperature rise is observed to be constant at about 4 mK up to 10 ms and is increasing much faster than expected from standard diffusion theory. For long diffusion times $t \gg t_{\text{max}}$ the recorded temperature response fairly approaches the calculated diffusive temperature profile.

This result was expected because three magnetic excitations had to be introduced to fit the thermal relaxation data on $\text{Dy}_2\text{Ti}_2\text{O}_7$ in the spin ice phase. With the individual contributions to the heat capacity per unit volume ($c_{\text{ph}}^R = 0.6$ $\mu\text{J cm}^{-3} \text{K}^{-1}$, $c_{\alpha}^R = 0.82$ $\text{mJ cm}^{-3} \text{K}^{-1}$, $c_{\beta}^R = 0.28$ $\text{mJ cm}^{-3} \text{K}^{-1}$ and $c_{\gamma}^R = 0.40$ $\text{mJ cm}^{-3} \text{K}^{-1}$) and the

corresponding relaxation times ($\tau_\alpha^R = 34$ s, $\tau_\beta^R = 1.9$ s and $\tau_\gamma^R = 4.9 \cdot 10^{-8}$ s) the numerical solution of the field equations (5.5) coincides with the recorded temperature profile.

But as can be seen in figure 5.11d, the temperature profile calculated according to the (3+3) field theory deviates from the recorded data for times shorter than 1 s (dashed red line). In order to describe the data on the whole time scale, the field equation system has to be extended by additional internal variables (i. e. magnetic excitations). It has been ascertained that the magnetic excitation \tilde{e}_γ is composed from a multitude of excitations $c_{\gamma j}^R$ ($j = 1, 2, \dots, n - 2$) with relaxation times $\tau_{\gamma j}^R$ in the range from 10^{-8} s to 0.25 s. Six magnetic γ -excitations in a (3 + 8) field theory are needed to describe completely the recorded temperature profile at $T_R = 368$ mK (see solid red line in figure 5.11d). A more detailed description of the heat pulse propagation analysis will be given by Peter Strehlow and co-worker [Neu10].

The number of additional internal variables \tilde{e}_γ , required to describe heat pulse propagation on a shorter time scale, increases continuously as the temperature is decreased from 1 K to 300 mK. This is due to the rise of relaxation times τ_γ^R as the temperature is lowered (see also figure 6.9).

The contributions $c_{\gamma j}^R$ and the corresponding relaxation times $\tau_{\gamma j}^R$ appearing in the field equations (5.5) are, however, not arbitrary. Summation over all $n - 2$ contributions $c_{\gamma j}^R$ yields the same heat capacity per unit volume c_γ^R as determined from thermal relaxation experiments. Similarly, the relaxation rates $(\tau_{\gamma j}^R)^{-1}$ add up to a value $(\tau_\gamma^R)^{-1}$ that agrees with the result of thermal conductivity measurement. Thus, the thermodynamic field theory turned out to be thermodynamically consistent.

It must be pointed out, that in particular these heat pulse experiments show the complex thermal processes in the spin ice $\text{Dy}_2\text{Ti}_2\text{O}_7$. As, on the basis of the thermodynamic field theory, we have analysed the homogeneous case (heat capacity) and the stationary case (thermal conductivity) we consequently receive from this theory the non-stationary inhomogeneous case, i. e. the heat pulse transport without no more additional assumptions. Vice versa, we can note that all three experimental studies on thermal relaxation and transport in $\text{Dy}_2\text{Ti}_2\text{O}_7$ can be described by an unique thermal model where phonons interact with a multitude of different magnetic subsystems, each system relaxing on individual time scales.

Chapter 6

Discussion of Results and Comparison to Magnetic Models

For magnetic fields along the [110] axis, the dysprosium spins can be considered to form two orthogonal sets of spin chains: parallel and perpendicular to the field direction, called α -chains and β -chains. This was primarily demonstrated by Fennell et al. [Fen02] using neutron diffraction studies, where the coexistence of long range ferromagnetic order (α -F) on field coupled spin chains and short range antiferromagnetic order (β -AF) on field independent spin chains was found (see figure 5.2). Following the concept of α -chains and β -chains [Hig02; Hir03; Yos04], we are able to identify a magnetic field dependent contribution $c_{m\alpha}$ and a magnetic field independent contribution $c_{m\beta}$. Beyond that, there are further magnetic contributions (in summary denoted by $c_{m\gamma}$) with considerably shorter relaxation times. The slowest contribution, the magnetic field dependent $c_{m\alpha}$ (with a relaxation time $\tau_{\alpha}^R \approx 100$ s at $T_R = 0.6$ K), shifts to higher temperatures as the field increases above 0.5 T. The field independent β -excitations (with relaxation times $\tau_{\beta}^R \approx 10$ s at $T_R = 0.6$ K) can be ascribed to Schottky-type excitations dominant in the spin ice phase, $T < 1.5$ K and $B < 0.5$ T. With stronger magnetic field, $B \geq 0.5$ T, magnetic order (α -F & β -AF) takes place and the specific heat $c_{m\beta}(T_R)$ exhibits signatures of a sharp transition at a critical temperature $T_c = 1.05$ K where the temperature dependencies below and above T_c do not change with increasing magnetic field.

The third observable contribution, $c_{m\gamma}$, to the total heat capacity, was regarded to couple on a fast time scale to the lattice phonon system as within the experimental limit of 0.1 s the temperature responses exhibited no evidence of a relaxational process. As argued

earlier [Mor09], for weak magnetic fields the Debye-Hückel model of a non-interacting dipolar gas of magnetic monopoles can be assigned to the $c_{m\gamma}$ -data. In the magnetic ordered phase, $B \geq 0.5$ T, the signature of $c_{m\gamma}(T_R)$ changes into the same behaviour as observed for $c_{m\beta}(T_R)$.

The thermal conductivity $\kappa(T_R, B)$ follows a single crystalline behaviour for $T \gtrsim 5$ K. At lower temperatures (between 0.3 K and 3 K) a pronounced dependency $\kappa \propto T^2$ is observed which we assign to a resonant phonon scattering process solely by the γ -excitations. Surprisingly, there is no significant change in $\kappa(B)$, for $T_R \gtrsim 3$ K. Only in the low temperature range with increasing magnetic fields from 0 T up to 1.5 T, the resonant scattering is about linearly attenuated by an amount of about 25 % as the magnetic field increases. We consider these findings as an indication that the γ -excitations are magnetic excitations which are strongly coupled to the thermal lattice modes, below 1 K.

6.1 Heat capacity at $T = 0.3 - 30$ K and $B = 0 - 1.5$ T

In order to visualize the general features of the specific heat for $\text{Dy}_2\text{Ti}_2\text{O}_7$, the total heat capacity is shown in figure 6.1 in the temperature range from 0.3 K to 30 K and for magnetic fields $B = 0$ T, 0.2 T, 0.5 T, 1 T and 1.5 T. Above approximately 1 K the full circles denote specific heat data calculated from the standard single-exponential calorimeter response. Contrary, below 1 K, the open circles denote $c_{\text{mag}} = (c_{m\alpha} + c_{m\beta} + c_{m\gamma})$ where the three contributions are derived from thermodynamic field theory analysis of non-exponential temperature responses. Around 1 K, it is evident that both datasets match smoothly as for $T \rightarrow 1$ K the related relaxation times decrease rapidly beyond 0.1 s (for more details, see section 6.1.1 to 6.1.5).

From figure 6.1 the significant difference between the weak field behaviour ($B = 0$ T and 0.2 T) and the strong field behaviour ($B = 0.5$ T, 1 T and 1.5 T) is clearly evident. More clearly, subtracting the lattice specific heat, c_{ph} , exhibits quantitative differences for $c_{\text{mag}}(T_R, B)$ in the spin ice regime and in the magnetically ordered phase, respectively.

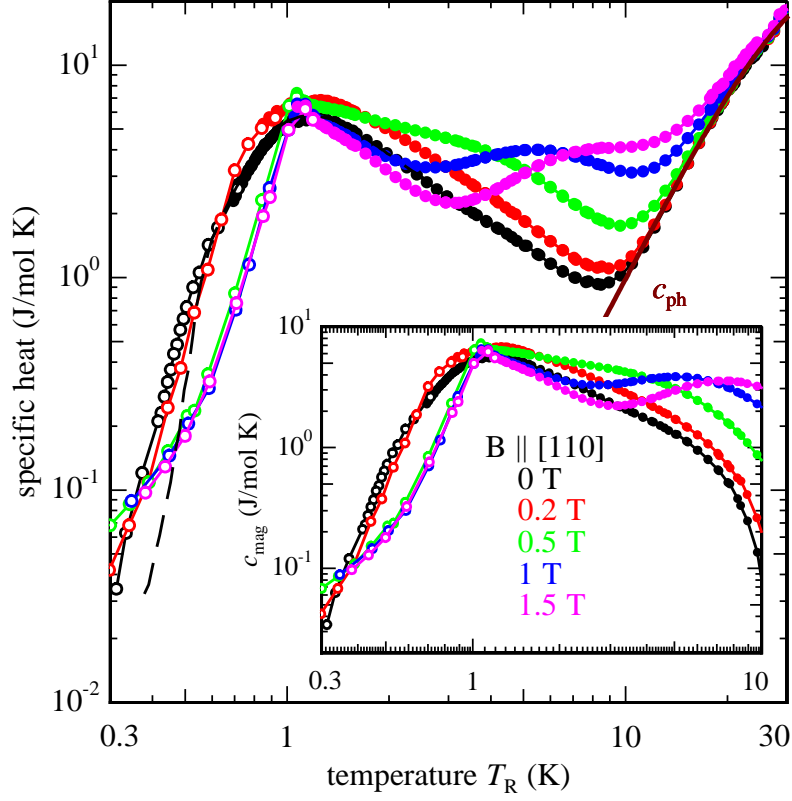


Figure 6.1: Total specific heat c_{total} as determined from standard calorimeter technique (full circles) and, below ca. 1 K, as analysed from thermodynamic field theory (open circles) according to Eqs. (5.1). The brown line denotes the phonon specific heat c_{ph} according to equation (6.2). The other full lines are guide for the eye, only. The dashed line, below 0.6 K, denote our specific heat data at zero field published in reference [Mor09] which have been calculated according to standard calorimeter algorithm. The inset shows the magnetic contribution c_{mag} , as c_{ph} has been subtracted from c_{total} .

According to the Debye model the lattice specific heat c_{ph} can be calculated from the density of states $D(\omega) \propto \omega^2$ and the occupation number of phonons $n(\omega, T)$ which follows the Bose-Einstein distribution. The internal energy $E(T)$ can be written as:

$$E(T) = \int_0^{\omega_D} D(\omega) \langle n(\omega, T) \rangle \hbar \omega d\omega \quad , \quad (6.1)$$

where ω_D is the maximum phonon frequency.

For the phonon specific heat c_{ph} follows from equation (6.1):

$$c_{\text{ph}}(T) = 9 n_{\text{Dy}} k_B N_A \cdot \left(\frac{T}{\theta_D} \right)^3 \cdot \int_0^{x_D} \frac{x^4 e^x}{(e^x - 1)^2} dx \quad , \quad (6.2)$$

where $n_{\text{Dy}} = 11$ denotes the number of oscillating atoms per molecule $\text{Dy}_2\text{Ti}_2\text{O}_7$, $\theta_{\text{D}} = \hbar\omega_{\text{D}}/k_{\text{B}}$ is the Debye temperature and $x_{\text{D}} = \theta_{\text{D}}/T$.

For low temperatures ($T \lesssim \theta_{\text{D}}/10$) the approximation of equation (6.2) results in Debye's classical T^3 dependence for the lattice specific heat (as already given by equation (4.14)). Using specific heat data between 10 K and 30 K, we have fitted the phonon specific heat according to equation (6.2) (see brown line in figure 6.1). The Debye temperature was calculated to $\theta_{\text{D}} = 283$ K corresponding to a Debye velocity $c_{\text{D}} = 2165$ m/s. Similar values have been reported by Hiroi et al. [Hir03]. The inset in figure 6.1 exhibits $c_{\text{mag}}(T, B)$, where c_{ph} (equation (6.2)) has been subtracted from the c_{total} data.

Due to the identification of the three magnetic subsystems, with specific heat $c_{\text{m}\alpha}$, $c_{\text{m}\beta}$ and $c_{\text{m}\gamma}$, and their individual relaxation times, τ_{α}^{R} , τ_{β}^{R} and τ_{γ}^{R} , we can discuss in more detail the possible origin of these excitations. In the next sections this will be presented – differenced for the weak field range (spin ice phase) and the strong field case (magnetically ordered phases).

6.1.1 Paramagnetic spin contribution from α -excitations

The early heat capacity measurements by Higashinaka et al. [Hig02] and Hiroi et al. [Hir03] have revealed that the α -chains can be described as a non interacting paramagnetic spin system which is field sensitive owing to the large Zeemann energy of external magnetic field. This feature is clearly visible as a broad peak in the specific heat data for magnetic fields $B \geq 0.5$ T (see figure 6.1): the peak $c_{\text{m}\alpha}^{\text{max}}$ shifts to higher temperatures with increasing magnetic field.

The specific heat of a paramagnetic spin system $c_{\text{m}\alpha}$ is given by [Mei04]:

$$c_{\text{m}\alpha}(T_{\text{R}}, B) = N_{\alpha} k_{\text{B}} \left[\left(\frac{x_{\text{PM}}}{2J} \right)^2 \text{cosech}^2 \left(\frac{x_{\text{PM}}}{2J} \right) - \left(\frac{(2J+1)x_{\text{PM}}}{2J} \right)^2 \text{cosech}^2 \left(\frac{(2J+1)x_{\text{PM}}}{2J} \right) \right] \quad (6.3)$$

$$\text{with } x_{\text{PM}} = g J \mu_{\text{B}} B / (k_{\text{B}} T_{\text{R}}) \quad ,$$

where N_{α} is the number of α -excitations per mol of $\text{Dy}_2\text{Ti}_2\text{O}_7$, J is the effective angular momentum quantum number and g is the Landé factor.

From a best-fit procedure on the specific heat data for $B = 1.5$ T, the number of α -excitations and the effective magnetic moment were determined to be $N_\alpha = 0.5N_A$ and $g J \mu_B = 10 \cdot \cos \theta \cdot \mu_B = 10 \sqrt{2/3} \mu_B$, respectively.

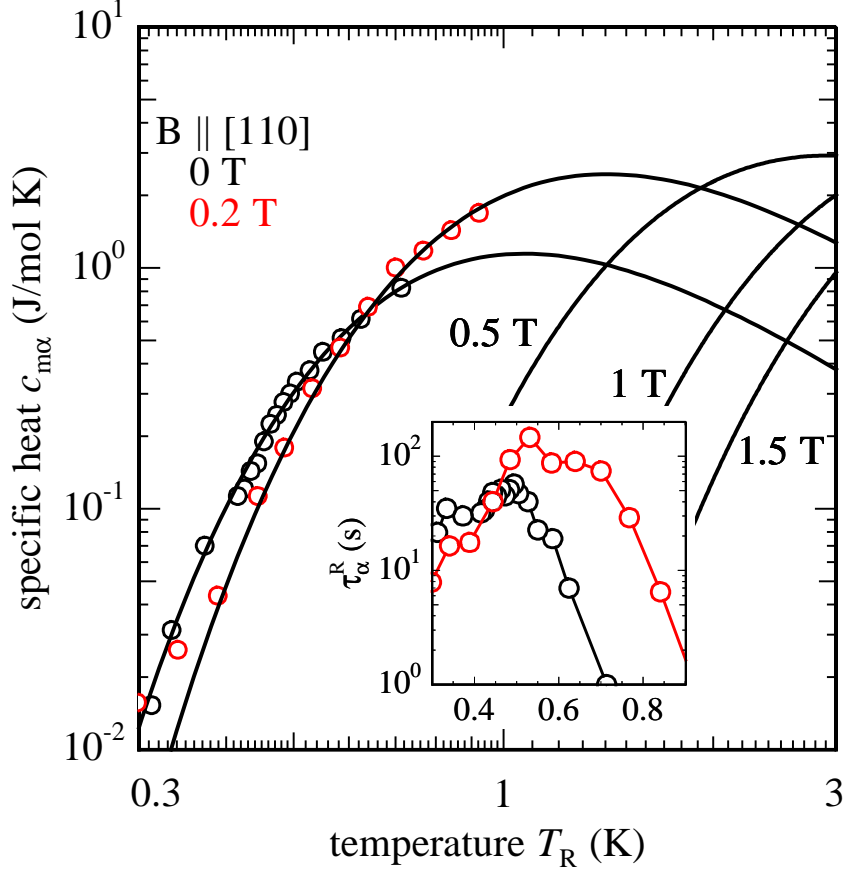


Figure 6.2: Specific heat $c_{m\alpha}$ of the α -excitations measured for $B = 0$ T and $B = 0.2$ T (open circles). The full lines are calculated according to the paramagnetic spin model, equation (6.3), for parameters see table 6.1. Note the Zeemann-shifted contribution $c_{m\alpha}$ as magnetic field increases $B = 0$ T, 0.2 T, 0.5 T, 1 T and 1.5 T. The inset shows the corresponding relaxation times τ_α^R according thermodynamic field theory analysis using equations (5.1).

The magnitude of the magnetic moment is here $10 \mu_B$ (corresponding to the value of the bare ion Dy^{3+} [Bra04]), and its direction forms an angle of $\theta = 35.26^\circ$ with the [110] magnetic field. The effective angular momentum was obtained to be $J \approx 1/2$ (so that $g \approx 20$) [Ram99]. Thus, for high magnetic fields $B \geq 1.5$ T along the [110] direction, the specific heat of the α -excitations can be described by a paramagnetic Ising spin system, where only half of the spins (namely two of four spins on a tetrahedron) couple to the field. This paramagnetic model should only be valid in the high-field limit,

where interspin coupling can be neglected. Nevertheless, we were able to fit well all measured data $c_{\text{m}\alpha}(T_{\text{R}}, B)$ to equation (6.3) using the same parameters as determined for $B = 1.5$ T (see figure 6.2). With decreasing field, however, the effective angular quantum number decreases and approaches, in the limit of the internal field $B = B_{\text{int}} = 0.070$ T, the value $J = 0.11$ which corresponds to a large Landé factor of $g = 88$ (for parameters see table 6.1).

Both, J and g , could be regarded as renormalized values due to dysprosium spin interactions between next-next nearest neighbours. This is different to the normal case for a non-interacting paramagnetic spin system where $g = 2$ and $J = 1/2$. It is no doubt interesting that in geometrically frustrated systems the strong coupling between the spins can lead to paramagnetic defects with a large magnetic moment $g \cdot J$ (in unit of the Bohr magneton μ_{B}) but vanishing small values of J (in the limit $J \rightarrow 0 \wedge g \rightarrow \infty$).

magnetic field	paramagnetic excitations		
B (T)	N_{α}/N_{A}	J	T_{α}^{max} (K)
0	0.5	0.114	1.07
0.2	0.5	0.283	1.5
0.5	0.5	0.36	2.9
1	0.5	0.43	5.0
1.5	0.5	0.49	7

Table 6.1: Parameters used for specific heat model calculations for $c_{\text{m}\alpha}(T, B)$ according to equation (6.3).

The paramagnetic behaviour of $c_{\text{m}\alpha}(T_{\text{R}}, B)$ is seen to dominate the high temperature and high field regimes, respectively, due to the Zeeman energy allocated by the dysprosium spins of the α -chains.

Below 1 K, the specific heat of the α -excitations decreases to very small values with increasing magnetic field. Hence, it is obvious that the specific heat of the α -excitations can not contribute in the thermodynamic field theory analysis for fields above 0.2 T. For $B \geq 0.5$ T the specific heat $c_{\text{m}\alpha}(T_{\text{R}} \approx 1$ K) is already smaller by a factor of nearly 50 than the total specific heat.

6.1.2 Schottky-type spin contribution from β -excitations

Following Hiroi et al. [Hir03], for the specific heat of the β -excitations we assume an unique Ising spin one dimensional system with the nearest-neighbour interaction ΔE_{Sch} . The specific heat from Schottky-type excitations $c_{m\beta}$ is given as:

$$c_{m\beta}(T_R) = N_\beta k_B \left(\frac{\Delta E_{\text{Sch}}}{k_B T_R} \right)^2 \frac{\exp\left(\frac{\Delta E_{\text{Sch}}}{k_B T_R}\right)}{\left(1 + \exp\left(\frac{\Delta E_{\text{Sch}}}{k_B T_R}\right)\right)^2} . \quad (6.4)$$

where N_β denotes the number of β -excitations per mol of $\text{Dy}_2\text{Ti}_2\text{O}_7$.

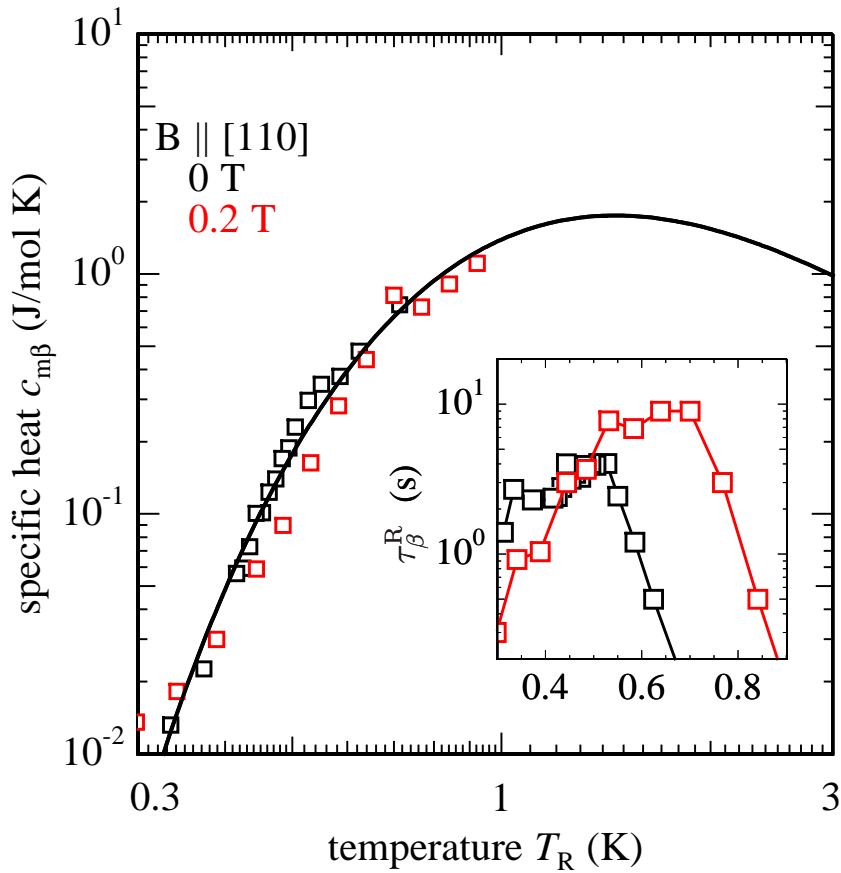


Figure 6.3: Specific heat $c_{m\beta}$ of the β -excitations measured for $B = 0 \text{ T}$ and $B = 0.2 \text{ T}$ (open squares). The full line is calculated according to the Schottky-type spin model, equation (6.4), for parameters see table 6.2. The inset shows the corresponding relaxation times τ_β^R according thermodynamic field theory analysis using equations (5.1).

With equation (6.4) we can fit the specific heat of the β -excitations for magnetic fields smaller than 0.5 T fairly well (see figure 6.3). For $B = 0$ T and 0.2 T, the best-fit value

magnetic field	Schottky-type excitations		
B (T)	N_β/N_A	ΔE_{Sch} (K)	T_β^{max} (K)
0	0.24	3.5	1.44
0.2	0.24	3.5	1.44

Table 6.2: Parameters used for specific heat model calculations for $c_{\text{m}\beta}(T_{\text{R}}, B)$ according to equation (6.4) for magnetic fields $B \leq 0.2$ T.

for ΔE_{Sch} is 3.5 K, which is a factor of three larger than the effective nearest neighbour energy $J_{\text{eff}}/k_{\text{B}} = 1.1$ K estimated by Bramwell et al. [Bra01b].

6.1.3 Thermal relaxation times τ_α^{R} and τ_β^{R} ($T < 1$ K, $B < 0.5$ T)

The thermal relaxation behaviour of the spin ice $\text{Dy}_2\text{Ti}_2\text{O}_7$ is illustrated in figure 6.4 by the magnetic relaxation times $\tau_\alpha^{\text{R}}(T_{\text{R}}, B = 0 \text{ T})$ and $\tau_\beta^{\text{R}}(T_{\text{R}}, B = 0 \text{ T})$ as function of temperature T_{R} . The data obtained by thermodynamic analysis of the thermal relaxation experiments are presented together with experimental data from susceptibility measurements by Snyder et al. [Sny04].

It is obvious to compare the thermal relaxation of $\text{Dy}_2\text{Ti}_2\text{O}_7$ to that of the spin-lattice relaxation in rare-earth salts. According to Orbach [Orb61] the spin-lattice relaxation rate in Kramers salts is determined by the Raman and the thermally activated processes, and given by:

$$(\tau_\nu^{\text{R}})^{-1} = a_\nu T_{\text{R}}^9 + b_\nu \exp\left(-\frac{E_\nu}{k_{\text{B}} T_{\text{R}}}\right) . \quad (6.5)$$

In fact, the temperature dependence of the relaxation time τ_α^{R} can be described by equation (6.5) for temperatures above 1.4 K (see blue line in figure 6.4). Below 20 K τ_α^{R} increases with decreasing temperature due to Raman process, entering a plateau region below 12 K, before passing through the Arrhenius temperature dependence with an activation energy E_α . By fitting the data to equation (6.5) the activation energy was determined to be $E_\alpha = 2.65$ K. This value corresponds to the creation energy of a

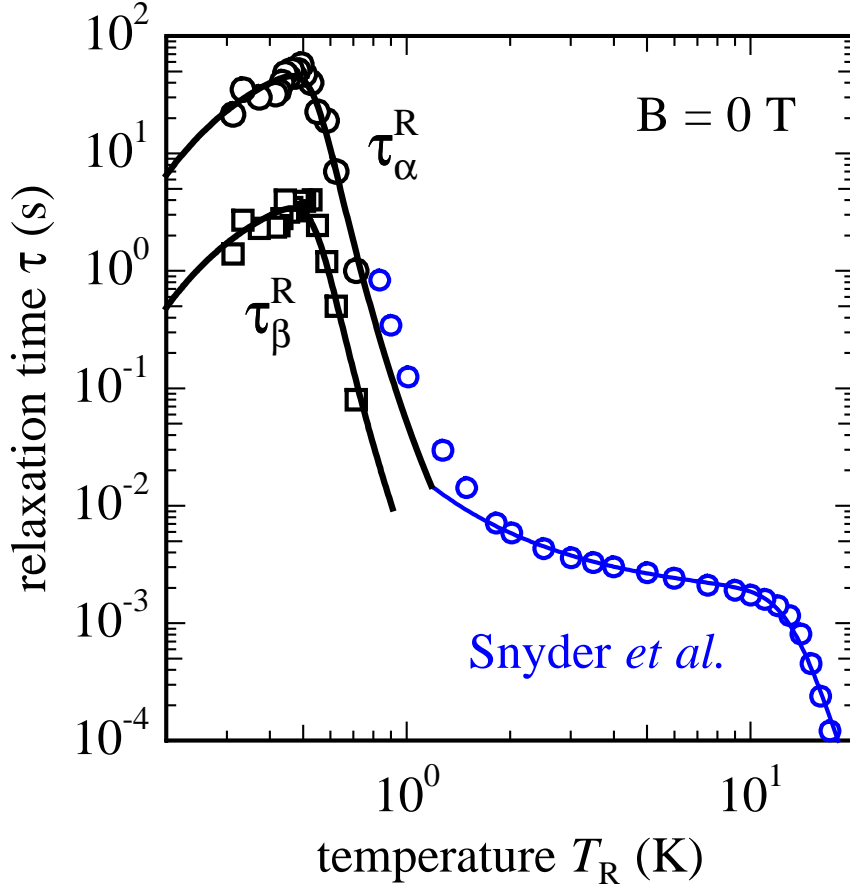


Figure 6.4: Relaxation times τ as function of temperature T_R for α -excitations (open circles) and β -excitations (open squares) as obtained by analysing the thermal relaxation experiments. For comparison relaxation data (blue circles) published by Snyder et al. [Sny04] are shown. The solid lines are best fits to the equations (6.5) and (6.6).

topological defect in the paramagnetic state of $\text{Dy}_2\text{Ti}_2\text{O}_7$ [Cas08; Cas09].

For $T > 1$ K, the calorimeter temperature responses exhibit single exponential behaviour resulting in a unique heat capacity c_{total} (full symbols in figure 6.1). However, this only means that an analysis of intrinsic relaxation time in the sample is limited due to the experimental range of time domain between 0.1 s and 100 s. Below 1 K, the existence of two narrow bounded relaxation processes becomes evident as can be seen from the insets in figure 6.2 and 6.3. For zero magnetic field, the relaxation times τ_α^R and τ_β^R emerge in the detectable limit of about 0.5 s and increase steeply to 50 s for τ_α^R and 5 s for τ_β^R , respectively, as the temperature decreases to 0.5 K. For small magnetic field

$B = 0.2$ T, these slow relaxation processes boost by a factor of two (up to 100 s for τ_α^R and 10 s for τ_β^R) and increase at higher temperatures by approximately 30%. With further decreasing temperature from 0.5 K down to 0.3 K, the slow relaxation times smoothly decrease for τ_α^R and τ_β^R in the case of $B = 0$ T and $B = 0.2$ T, as well. With respect to the concept of α -chains and β -chains, it appears surprising that the variations of $\tau_\alpha^R(T_R)$ and $\tau_\beta^R(T_R)$ with temperature are so similar.

Fennell et al. [Fen04] observed in their [110] magnetic diffraction studies on single crystalline $\text{Dy}_2\text{Ti}_2\text{O}_7$ similar slow dynamics and argued that metastable states and coexisting long and short range order could appear in both orientations for α -chains and β -chains. Moreover, Orendáč et al. [Ore07] have studied the magnetocaloric effect in polycrystalline $\text{Dy}_2\text{Ti}_2\text{O}_7$ in the spin ice regime down to 0.3 K. Using adiabatic demagnetization cooling they calculated relaxation times up to 1000 s from the observed temperature profiles. These demagnetization experiments on $\text{Dy}_2\text{Ti}_2\text{O}_7$ strongly suggested that down to 0.3 K the dynamics are dominated by thermally activated spin-lattice relaxation (see equation (6.5)).

The results of Orendáč et al. [Ore07] can be considered as a qualitative extension of the ac-susceptibility studies of Snyder et al. [Sny04] in the temperature range $T = 16$ K to 0.7 K. The rapid increase of $\tau(T)$ below 2 K (actually faster than would be expected for activated behaviour) was attributed to the increasingly strong correlations between the spins with decreasing temperature.

After Sondhi, Moessner and Castelnovo [Cas08] established the quasiparticle picture of magnetic monopoles in spin ice $\text{Dy}_2\text{Ti}_2\text{O}_7$, Jaubert and Holdsworth [Jau09a] presented a re-interpretation of the magnetic relaxation measurements of Snyder et al. [Sny04]. The authors showed that Coulomb interactions between the magnetic charges are responsible for the non-Arrhenius temperature dependence of the relaxation time scales below 1 K: as temperature decreases, the diffusion is slowing down due to the modification of defect concentration by the creation of locally bound monopole pairs.

Recently, Bramwell et al. [Bra09] reported on the measurement of the charge and current of magnetic monopoles in spin ice using muon spectroscopy techniques (see section 3.2). In a temperature range from 4.5 K to 0.07 K and for magnetic fields (parallel to [100]) of 1 mT and 2 mT, it was shown that the muon relaxation rate λ is proportional to the magnetic relaxation time scale. With decreasing temperature, λ , i. e. the magnetic relaxation time, is increasing following the expected thermally

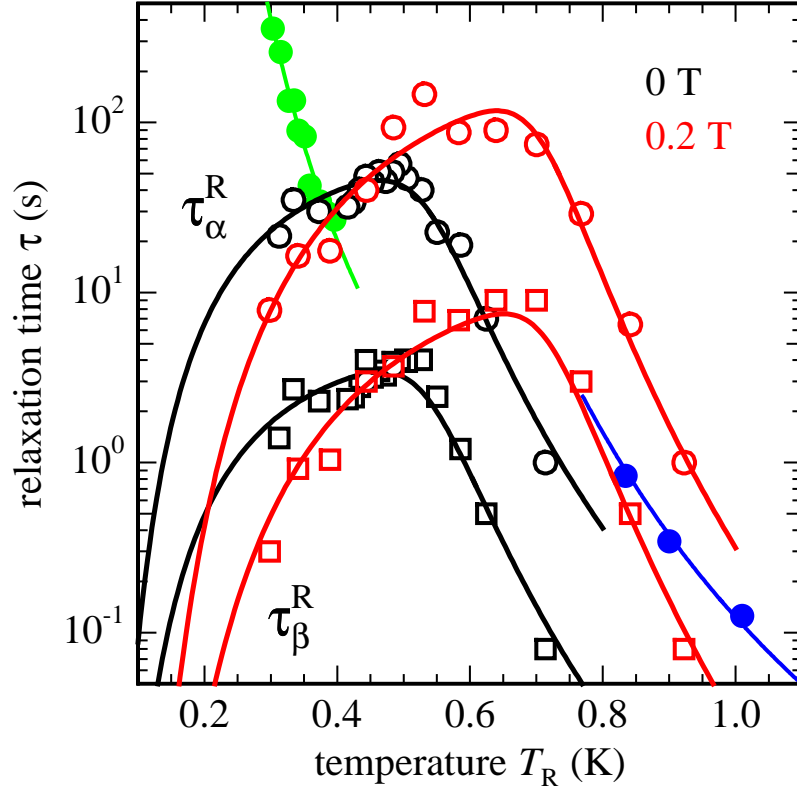


Figure 6.5: Relaxation times of α -excitations (open circles) and β -excitations (open squares) for $B = 0$ T and 0.2 T according to thermodynamic field theory analysis in comparison with relaxation measurements by Snyder et al. [Sny04] (blue circles) and Orendáč et al. [Ore07] (green circles). The corresponding coloured solid lines (blue and green) depict a thermal activated process (see equation (6.5)) which is an adequate description; see text. Solid black (red) lines are best fit to theoretical model for τ_{α}^R and τ_{β}^R at $B = 0$ T (0.2 T); see text. All parameters are shown in table 6.3.

activated behaviour. However, at $T < 0.5$ K, λ decreases with temperature consistent with our observation on τ_{α}^R and τ_{β}^R . Bramwell et al. [Bra09] argue that at very low temperatures, λ is proportional to the monopole concentration and its rapid decrease below 0.5 K marks a crossover from the regime of strong screening to the regime of weak screening of the charges. The crossover from the screened regime to the presumed unscreened regime ($T < 0.3$ K) is determined by the rapid decrease of the degree of dissociation between the numbers of bound pairs and unbound pairs.

In figure 6.5 we present a comparison on the calorimetric thermal relaxation times τ_{α}^R and τ_{β}^R , respectively, the magnetocaloric data (green colour) from Orendáč et al. [Ore07] and the ac-susceptibility data (blue colour) by Snyder et al. [Sny04]. The solid

lines (blue and green) have been fitted according to a thermally activated spin-lattice process (equation (6.5)) where the activation energy ranges between 3.6 K (Orendáč) and 10 K (Snyder). For τ_α^R and τ_β^R the so called attempt frequency b_ν of the thermal activation process has been chosen to be temperature dependent and can be analytically described by:

$$b_\nu(T_R) = \bar{b}_\nu + d_\nu T_R \exp\left(\frac{E_\nu + \epsilon_\nu}{k_B T_R}\right), \quad (6.6)$$

in order to account for the degree of dissociation in a dilute monopole gas according to a decrease of the monopole concentration [Bra09]. Here \bar{b}_ν is the attempt frequency for strong screening of the charges, and the weakening of screening is taken into account by the exponential term with the potential ϵ_ν .

The full black lines ($B = 0$ T) and red lines ($B = 0.2$ T) denote best fits with respect to equation (6.5) and equation (6.6). The activation energies resulting by fitting the low temperature data ($T_R < 1.1$ K) to equation (6.5) and (6.6) are given by $E_\alpha/k_B = E_\beta/k_B = 8.3$ K. In contrast to the paramagnetic state, a thermally generated spin flip in the spin ice state configuration constitutes a pair of topological defects, due to the Bernal-Fowler ice rule. Thus the activation energy should result from the double energy value of the single topological defect and the Coulombic energy to separate the (monopole) charges. In this way, the activation energy can be estimated to give $E_{\alpha(\beta)}/k_B = (2 \cdot 2.65 + 3.06)$ K = 8.36 K [Cas09], in close agreement with the presented experimental results. The potential affecting the screening was determined to be $\epsilon_\alpha/k_B = \epsilon_\beta/k_B \approx 1$ K.

As can be seen in figure 6.5, due to a magnetic field (of 0.2 T) the relaxation times are increased, and the maximum is shifted to higher temperature. This becomes noticeable in an increase of both the activation energy $E_\alpha/k_B = E_\beta/k_B = 15$ K and the potential $\epsilon_\alpha/k_B = \epsilon_\beta/k_B \approx 2$ K. All parameters can be seen in table 6.3.

	\bar{b}_ν (s ⁻¹)	E_ν (K)	d_ν (s ⁻¹ K ⁻¹)	ϵ_ν (K)
τ_α^R ($B = 0$ T)	$77.4 \cdot 10^3$	8.3	$5.15 \cdot 10^{-3}$	1
τ_β^R ($B = 0$ T)	$963.6 \cdot 10^3$	8.3	$69.1 \cdot 10^{-3}$	1
τ_α^R ($B = 0.2$ T)	$9.85 \cdot 10^6$	14.95	$0.537 \cdot 10^{-3}$	2
τ_β^R ($B = 0.2$ T)	$104.4 \cdot 10^6$	14.95	$8.71 \cdot 10^{-3}$	2

Table 6.3: Parameters used for fitting relaxation times τ_α^R and τ_β^R according to equations (6.5) and (6.6).

Having presented for τ_α^R and τ_β^R a satisfying agreement to formerly published slow relaxation times (Snyder) and to recent monopole theory arguments (Jaubert and Holdsworth, Bramwell et al.), respectively, we like to emphasize the successful application of the thermodynamic field theory ansatz which provided the analytical tool to analyse the non-exponential temperature responses recorded from our calorimetric experiments.

6.1.4 Fast-relaxing magnetic specific heat

($T < 1$ K, $B < 0.5$ T)

The γ -excitation – the third system which contributes to the specific heat according to the thermodynamic field theory – has relaxation times much smaller than the time resolution of the specific heat measurements of 0.1 s. Therefore we can not exactly determine the relaxation times τ_γ^R . We estimate $\tau_\gamma^R \leq 1$ ms as an upper limit for the relaxation time, because smaller relaxation times have no influence to the temperature time profile. In figure 6.6 open triangles represents the specific heat $c_{m\gamma}$. For $T_R \gtrsim 1$ K closed circles have been calculated by subtracting $c_{ph}(T_R)$ (equation (6.2)) and the modelled $c_{m\alpha}(T_R, B)$ (equation (6.3)) and $c_{m\beta}(T_R)$ (equation (6.4)) from specific heat c_{total} as measured with single exponential specific heat analysis.

For 0 T and 0.2 T, both datasets for $c_{m\gamma}$ have nearly the same temperature dependence in the overall temperature range from 0.3 K to 10 K. The maximum deviation is around 1 K where $c_{m\gamma}(B = 0.2$ T) is increased by approximately 10 %. In first attempt we compare the $c_{m\gamma}(T_R)$ data with the Debye-Hückel model proposed by Castelnovo et al. [Cas09; Mor09] for a dipolar gas of magnetic monopoles.

The heat capacity per dysprosium spin c_{DH} has been calculated [Cas09] from the free energy $F(T)$:

$$F(T) = N_{DH}k_B \left[\frac{\rho}{2}\Delta - T \frac{S_0}{N_{DH}} + \frac{T\rho}{2} \ln \left(\frac{\rho/2}{1-\rho} \right) + \frac{T}{2} \ln(1-\rho) - \frac{T}{3\sqrt{3}\pi} \left(\frac{\alpha_{DH}^2}{2} - \alpha_{DH} + \ln(1 + \alpha_{DH}) \right) \right] \quad (6.7)$$

$$\text{with } \alpha_{DH} = \sqrt{\frac{3\sqrt{3}\pi E_{nn}}{2}} \sqrt{\frac{\rho}{T}} \quad ,$$

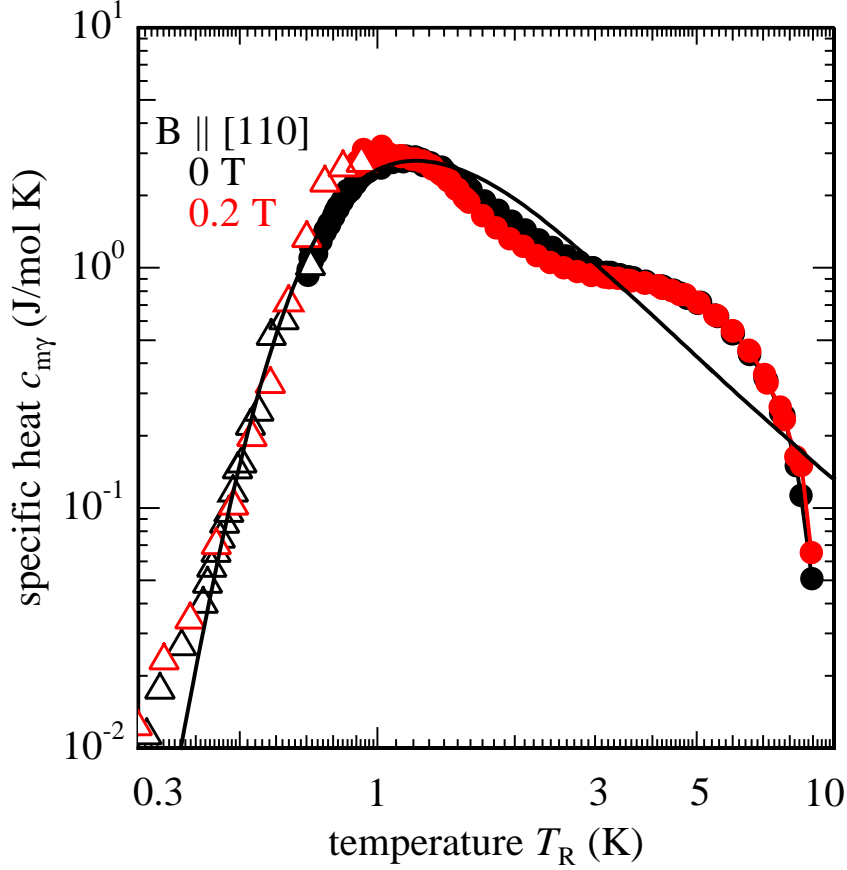


Figure 6.6: Specific heat $c_{m\gamma}$ of the γ -excitations measured for $B = 0$ T and $B = 0.2$ T (open triangles). Closed circles are calculated by subtracting $c_{m\alpha}(T_R, B)$, $c_{m\beta}(T_R)$ and $c_{ph}(T_R)$ from c_{total} measured with common specific heat analysis. The full black line depicts the specific heat from monopole-like excitations according to Debye-Hückel theory [Cas09], equation (6.8), for parameters see table 6.4.

with the energy cost of one isolated monopole $\Delta = 4.35$ K, the energy of two monopoles at nearest neighbour distance $E_{mn} = 3.06$ K, the spin contribution to the system entropy S_0 , and the defect density ρ . N_{DH} is the number of dysprosium spins which contribute to the Debye-Hückel model.

Minimizing equation (6.7) with respect to the defect density ρ one can solve $F_{min}(\rho, T)$ numerically and the heat capacity c_{DH} can be calculated:

$$c_{DH}(T) = -T \frac{\partial^2 F(T)}{\partial T^2} . \quad (6.8)$$

The Debye-Hückel model breaks down when typical length scales (screening length, monopole separation) become of the order of the lattice constant. This happens for $T > 1$ K, where the spin ice state gives way to a more conventional paramagnet, and monopoles cease to be suitable quasiparticles. As shown by the full line in figure 6.6, the Debye-Hückel model works well below $T = 1.5$ K. The discrepancy below 0.4 K could result from the lack in time resolution below 0.1 s and the accordingly large errors on the fitting of the temperature profile according to thermodynamic field theory analysis in this time domain.

magnetic field	Debye-Hückel excitations	
B (T)	$N_{\text{DH}}/N_{\text{A}}$	$T_{\text{DH}}^{\text{max}}$ (K)
0	0.4	1.2
0.2	0.4	1.2

Table 6.4: Parameters used for specific heat model calculations for $c_{\text{DH}}(T)$ according to equation (6.8) for magnetic fields $B \leq 0.2$ T.

As the Debye-Hückel calculation is rather complicated a more simplified fit to the $c_{\text{m}\gamma}$ -data is empirically found by best-fit procedure:

$$c_{\text{m}\gamma}(T) \approx \begin{cases} 6.5 \cdot 10^3 \frac{\text{J}}{\text{mol K}^8} T^7 e^{-(7.8 \text{ K})/T} & \text{for } 0.5 \text{ K} \lesssim T \lesssim 1.4 \text{ K} \\ 1.3 \frac{\text{J}}{\text{mol K}^5} T^4 & \text{for } 0.3 \text{ K} \lesssim T \lesssim 0.5 \text{ K} \end{cases} . \quad (6.9)$$

6.1.5 Heat capacity in the magnetic ordered phase ($B \geq 0.5$ T)

At stronger magnetic fields, i. e. $B = 0.5$ T, 1 T and 1.5 T, and for temperatures below 1.2 K, the non-exponential behaviour of the temperature profiles $\tilde{T}(t)$ remains obvious down to 0.3 K. Due to the Zeemann energy shift $\sim \mu_{\text{B}} B$ (equation (6.3)) the α -contribution has shifted to much higher temperatures (see figure 6.2) and now contributes to single exponential $\tilde{T}(t)$. As the γ -contribution relaxes faster than observable within our experimental time window, the only detectable relaxation time is τ_{β}^{R} as shown in the inset of figure 6.7a. Below 1 K, $\tau_{\beta}^{\text{R}}(T_{\text{R}})$ displays a similar temperature dependence for all three magnetic fields applied: the relaxation process is about constant

in a range from 5 s to 10 s; for $T_R \gtrsim 1$ K, the relaxation time sharply drops beyond 1 s and single-exponential temperature profiles are observed. As can be seen from figure 6.7a, for temperatures below 1 K the $c_{m\beta}$ - and $c_{m\gamma}$ -contribution follow a similar temperature dependence for all three magnetic fields and so does the summarized capacity $c_{\beta+\gamma} = c_{m\beta} + c_{m\gamma}$. For $T \gtrsim 1$ K, the temperature dependence is superimposed by the specific heat from the α -chains $c_{m\alpha}(T_R, B)$ as indicated by the different slopes of the measured specific heat (full circles in figure 6.7a).

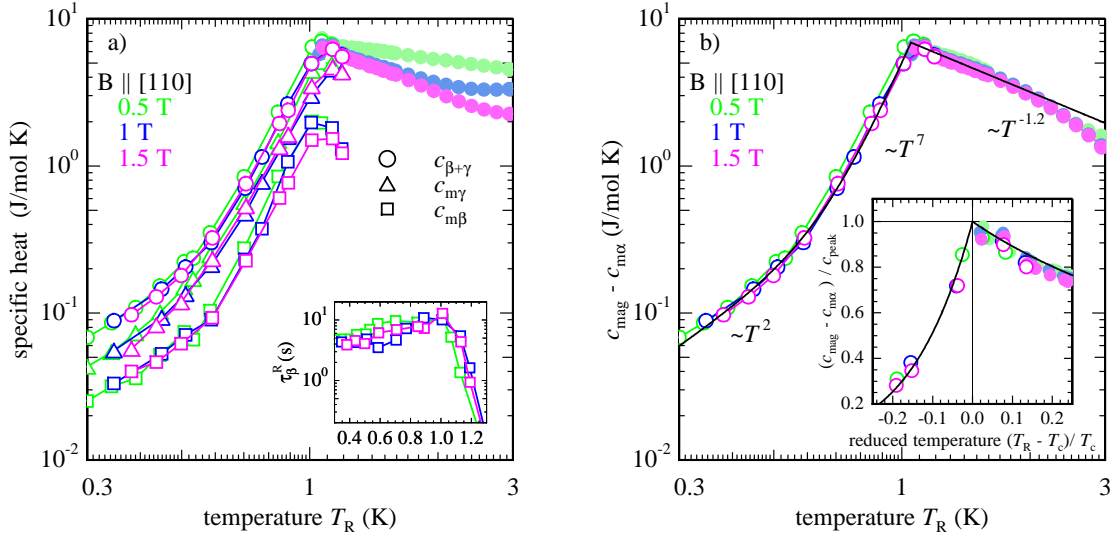


Figure 6.7: Specific heat $c_{m\beta}$ and $c_{m\gamma}$ and the summarized total contribution $c_{\beta+\gamma} = c_{m\beta} + c_{m\gamma} \approx c_{\text{mag}}$ for $B \geq 0.5$ T.

(a) Open symbols denote data from thermodynamic field theory analysis, closed symbols denote specific heat measured with common specific heat analysis; the inset shows the temperature dependence of the β relaxation process.

(b) The paramagnetic contribution $c_{m\alpha}(T_R, B)$ has been subtracted from the raw data shown in (a): the plotted data $c_{\text{mag}} - c_{m\alpha}$ show common temperature dependence for all three magnetic fields $B = 0.5$ T, 1 T and 1.5 T. The black full line depicts the specific heat according to an empirical polynomial function, equation (6.10); parameters are listed in table 6.5. The inset exhibits an expanded view around the critical temperature T_c where $(c_{\text{mag}} - c_{m\alpha})/c_{\text{peak}}$ scales with the reduced temperature $(T_R - T_c)/T_c$ for all three magnetic fields.

In figure 6.7b the common magnetic behaviour as indicated by the raw data in figure 6.7a is underlined by subtracting the paramagnetic contribution of the α -chains $c_{m\alpha}(T_R, B)$. For all fields $B = 0.5$ T, 1 T and 1.5 T the specific heat is nearly the same. The distinctive feature is the sharp peak at a critical temperature $T_c = 1.05$ K and the very steep slope ($c \propto T^7$) for temperatures between 0.4 K and 1.05 K. For temperatures below 0.4 K we observe a T^2 behaviour. For temperatures above 1.05 K the specific heat is proportional to $T^{-1.2}$. The inset of figure 6.7b exhibits an expanded view around

T_c where $(c - c_{m\alpha})/c_{\text{peak}}$ scales with the reduced temperature $(T_R - T_c)/T_c$ for all three magnetic fields.

These temperature and field dependencies of the specific heat already have been reported from the specific heat experiments by Hiroi et al. [Hir03] and subsequent Monte-Carlo studies of Yoshida et al. [Yos04]. From the MC-simulations [Yos04] it was concluded that at $T > T_c$ spins on the α -chains are fixed to the magnetic field (α -F phase), while spins on the β -chains still have random configurations. At $T = T_c$, the spins on the β -chains form β -AF order and a first-order phase transition to a α -F & β -AF configuration takes place.

Here, we characterize our results on $c_{\text{mag}}(T)$ for magnetic fields $B \geq 0.5$ T with power functions of the form:

$$c_{\text{mag}}(T_R, B) = c_{m\alpha}(T_R, B) + \begin{cases} c_1 \left(\frac{T_R}{T_c}\right)^2 + c_2 \left(\frac{T_R}{T_c}\right)^7 & \text{for } T_c < T_R \lesssim 3 \text{ K} \\ (c_1 + c_2) \left(\frac{T_R}{T_c}\right)^{-1.2} & \text{for } 0.3 \text{ K} \lesssim T_R \leq T_c \end{cases} \quad (6.10)$$

with $T_c \approx 1.05$ K.

B (T)	c_1 (J/mol K)	c_2 (J/mol K)	T_c (K)
0.5	0.72	6.5	1.04
1	0.72	6.2	1.05
1.5	0.72	6.2	1.05

Table 6.5: Parameters used for specific heat model calculations for $B \geq 0.5$ T according to equation (6.10).

We have yet no theory to explain the specific heat contributions of the β - and γ -excitations for magnetic fields above 0.5 T. The presentation of our results may give an impulse for others to devise a theoretical model.

6.2 Thermal conductivity at $T = 0.3 - 30$ K and $B = 0 - 1.5$ T

The thermal conductivity $\kappa(T_R, B)$, which will be presented here as a first measurement on $\text{Dy}_2\text{Ti}_2\text{O}_7$, confirms the high quality of the [110] orientated single crystal: the thermal conductivity exhibits a high peak value of 0.1 W/cm K at 12 K followed by a $\kappa \propto T^2$ decrease down to the lowest temperature measured.

In figure 5.10 we present the bare thermal conductivity data are shown with the heat flow and the magnetic field parallel to the [110] axis. In the the overall studied temperature range from 0.3 K to 30 K a surprisingly weak dependence on the magnetic field strength was observed. Within the experimental error of less than $\pm 3\%$ on the relative values of $\kappa(T_R, B)$, around 1 K the thermal conductivity between zero field and 1.5 T decreased only by about 25% . At temperatures above 10 K no magnetic field dependency was observed. Below 2 K and for all magnetic fields measured, a temperature dependence $\kappa \propto T^2$ is dominant.

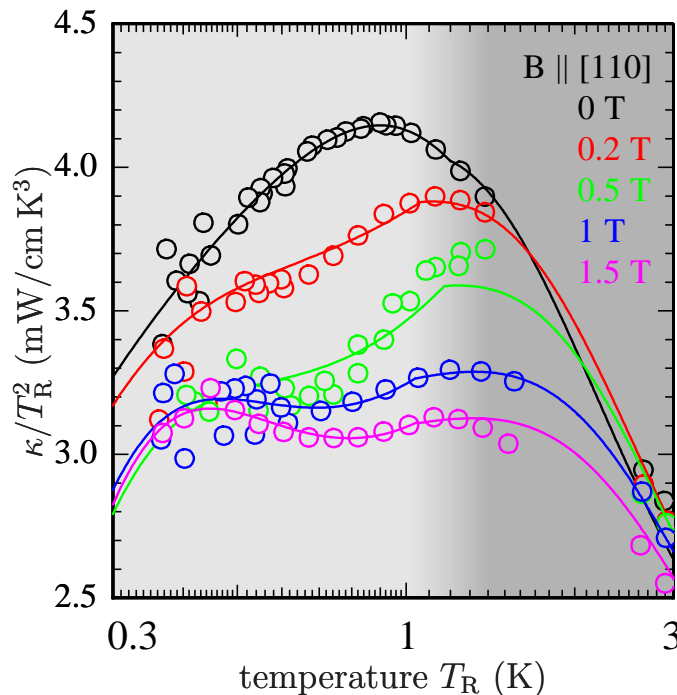


Figure 6.8: Thermal conductivity data plotted as κ/T_R^2 versus temperature (open circles). The solid lines depict the thermal conductivity calculated using the theoretical model according to equations (5.4), (6.5), (6.6) and (6.14) (for parameters see tables 6.6, 6.7 and 6.8). In the two shaded temperature regions below 1 K and above 1.4 K two parameter sets with different values for the thermal conductivity model have been chosen (see text).

More precisely this is shown in figure 6.8 where on a linear scale the low-temperature plot κ/T_{R}^2 exhibit weak, but significant signatures: In the ferromagnetic ordered phase ($B = 1$ T and 1.5 T) the dependence $\kappa/T_{\text{R}}^2 \approx \text{const.}$ holds for temperatures below 2 K whereas in the spin ice phase ($B < 0.5$ T) a weak resonance-like signature seems to be characteristic.

6.2.1 Phonon scattering theory of $\text{Dy}_2\text{Ti}_2\text{O}_7$ lattice

The thermal conductivity κ is directly coupled to the mean free path of phonons ℓ . Via the Debye velocity c_{D} the mean free path of phonons is equivalent to the relaxation time τ of the phonons: $\tau = \ell/c_{\text{D}}$. Using equation (5.4) one can calculate the thermal conductivity on the basis of relaxation times of various lattice related resistive scattering processes τ_{R} and the relaxation times τ_{ν}^{R} of the magnetic subsystems. The following three scattering processes are taken into account for the resistive scattering processes using the Debye-Callaway model with frequency-dependent relaxation times [Cal59] which can be sufficiently determined from the thermal conductivity data for $T > 10$ K.

Boundary scattering

The boundary scattering is described by a constant scattering rate, which is dependent on the smallest characteristic dimension (here: diameter d of the $\text{Dy}_2\text{Ti}_2\text{O}_7$ sample rod) of the material and the Debye velocity:

$$\tau_{\text{bou}}^{-1} = c_{\text{D}}/d \quad . \quad (6.11)$$

Defect scattering

The phonon scattering with defects in the crystal structure can be described by a relaxation time which is proportional to ω^{-4} and therefore proportional to T^4 when we use the dominant phonon approximation:

$$\tau_{\text{def}}^{-1}(T) = a_{\text{def}} \cdot T^4 \quad ; \quad (6.12)$$

the rate a_{def} will be treated as a fitting parameter to the thermal conductivity data above 10 K.

Umklapp processes

Phonon-phonon interactions have been described by normal processes and umklapp processes [Ash05]. Whereas normal processes provide internal thermalization of the moving phonon gas, only the umklapp processes contribute to a resistive behaviour against the propagating heat flow of the phonon system. Umklapp processes are described by a relaxation rate which is temperature and frequency dependent:

$$\tau_{\text{umk}}^{-1}(T) = a_{\text{umk}} \cdot T^4 \cdot \exp\left(-\frac{\alpha \theta_{\text{D}}}{T}\right) . \quad (6.13)$$

The resultant average relaxation rate of the resistive scattering process τ_{R}^{-1} is then given by:

$$\tau_{\text{R}}^{-1} = a_{\text{def}} T_{\text{R}}^4 + a_{\text{umk}} T_{\text{R}}^4 \exp\left(-\frac{\alpha \theta_{\text{D}}}{T_{\text{R}}}\right) + c_{\text{D}}/d . \quad (6.14)$$

In table 6.6 the parameters for the resistive processes are shown that have to be chosen to reproduce the temperature dependence of thermal conductivity in the temperature range $10 \text{ K} < T_{\text{R}} < 30 \text{ K}$. The resistive scattering process is not dependent on the magnetic field and therefore the parameters are constant. The parameter d is roughly comparable with the smallest sample dimension of 2.83 mm. The Debye temperature $\theta_{\text{D}} = 283 \text{ K}$ has been calculated from the specific heat data for $T > 20 \text{ K}$ (see section 6.1).

d (mm)	a_{def} ($\text{s}^{-1}\text{K}^{-4}$)	a_{umk} ($\text{s}^{-1}\text{K}^{-4}$)	α
2.07	$7.90 \cdot 10^4$	$1.19 \cdot 10^5$	0.428

Table 6.6: Parameters for resistive scattering processes used for fitting thermal conductivity data according to equation (5.4). These parameters are independent of magnetic field and temperature.

6.2.2 Scattering by magnetic excitations

In the temperature range below 10 K, the scattering of phonons by magnetic excitations becomes evident and results in a deviation from the cubic temperature dependence of thermal conductivity observed for a perfect dielectric crystal. Instead of the cubic temperature dependence, as expected for boundary scattering in a single crystal, the thermal conductivity varies nearly quadratically with temperature. This characteristic low-temperature behaviour (see figure 6.8) has to be attributed to the scattering

of phonons by magnetic excitations. Because the phonon scattering rates on both the α -excitations and the β -excitations are smaller by orders of magnitude compared to the boundary scattering rate, as explained in section 6.1.3, the low-temperature behaviour of thermal conductivity is exclusively affected by the relaxation of the γ -excitations $\tau_\gamma^R(T_R, B)$. Given this argument, we are able to determine τ_γ^R from the thermal conductivity data using equation (5.4). The result of this calculation is shown in figure 6.9.

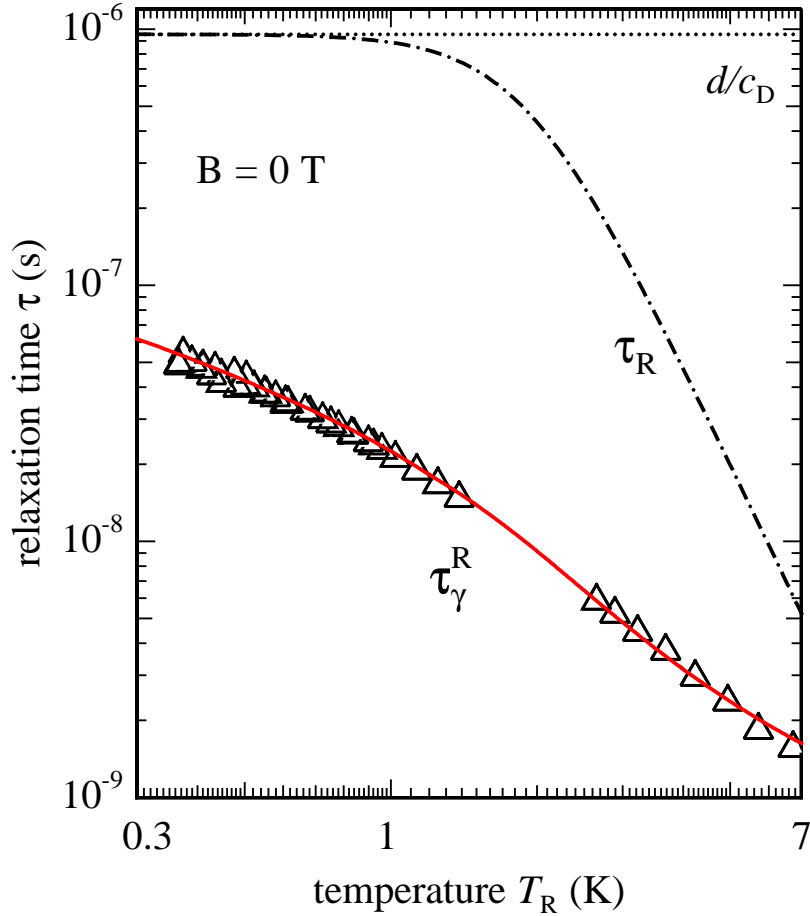


Figure 6.9: Phonon relaxation times calculated from the thermal conductivity data (figure 5.10). Above 10 K, resistive scattering processes, equation (6.14), dominate (dot-dashed line). According to the Debye-Callaway model for low temperatures the relaxation time is limited by boundary scattering processes, which results in a relaxation time of $d/c_D = 9.8 \cdot 10^{-7}$ s. Below 10 K, a much stronger scattering process becomes evident as depicted by the open triangles which have been calculated from equation (5.4). This scattering process is attributed to the magnetic γ -excitations. The solid red line is a best fit to the data (triangles) according to equations (6.5) and (6.6).

The data of relaxation times τ_γ^R as extracted from the thermal conductivity measurements can be well fitted by the equations (6.5) and (6.6) which have been accounted for the temperature dependencies of the α - and β -relaxation process. The activation en-

ergy and the potential resulting from fits to the low temperature data ($T_R < 1$ K) were obtained to be $E_\gamma = 5.3$ K and $\epsilon_\gamma/k_B = 0.1$ K, respectively. In comparison to the parameters for the α - and β -relaxation processes (see table 6.3), these γ -values are smaller, due to the more closely located monopole charges involved in the fast γ -processes: The screening ϵ_γ is diminished by a factor of 10 and the smaller activation energy E_γ results from the doubled energy value of the single topological defect, i. e. two times 2.65 K.

B (T)	$\bar{b}_\gamma (\cdot 10^7 \text{ s}^{-1})$	E_γ (K)	$d_\gamma (\cdot 10^7 \text{ s}^{-1} \text{ K}^{-1})$	ϵ_γ (K)
0	43.9	5.41	3.83	0.10
0.2	3.9	1.04	2.82	0.18
0.5	7.7	0.95	1.65	0.35
1	9.7	1.00	1.47	0.37
1.5	11.3	1.06	1.37	0.4

Table 6.7: Parameters used for the relaxation time τ_γ^R according to the equations (6.5) and (6.6) for temperatures below 1 K.

In figure 6.8 the model calculated thermal conductivity $\kappa(T_R, B)$ according to equations (5.4), (6.5), (6.6) and (6.14) is shown to fit the data nearly perfect. However, for low temperatures ($T_R < 1$ K) and for higher temperatures ($T_R > 1.4$ K) the parameter values differ substantially (see tables 6.7 and 6.8).

B (T)	$\bar{b}_\gamma (\cdot 10^7 \text{ s}^{-1})$	E_γ (K)	$d_\gamma (\cdot 10^7 \text{ s}^{-1} \text{ K}^{-1})$	ϵ_γ (K)
0	92.7	7.30	4.05	0.10
0.2	114	8.76	4.50	0.05
0.5	143	10.1	4.91	0.05
1	144	10.7	5.39	0.05
1.5	145	10.9	5.72	0.04

Table 6.8: Parameters used for the relaxation time τ_γ^R according to the equations (6.5) and (6.6) for temperatures above 1.4 K.

For $B = 0$ T and $T_R > 1.4$ K the value $E_\gamma = 7.3$ K is very similar to $E_\gamma = 5.41$ K (for $T_R < 1$ K). This could mean, that the ice rule is still valid on short-range order in the paramagnetic state. In addition, in the paramagnetic state of $\text{Dy}_2\text{Ti}_2\text{O}_7$ the charges of γ -excitations seems to be more separated from each other.

An answer to the question whether the γ -excitations can be related to fast next neighbour spin-phonon-processes could be given by extending the thermal conductivity measurements to temperatures well below 0.3 K, i. e. $T \rightarrow 0$ K. Within the monopole picture the monopole density decreases rapidly with decreasing temperature. Therefore, below some temperature there would be no magnetic scatterers (monopoles) left and the thermal conductivity should exhibit a typical T^3 dependence due to the boundary scattering only.

Chapter 7

Conclusion and Summary

We studied the pyrochlore crystal $\text{Dy}_2\text{Ti}_2\text{O}_7$ with the method of diffuse neutron diffraction in the temperature range around 1 K and magnetic fields below 0.7 T. Under these thermodynamic parameters the dysprosium spins in $\text{Dy}_2\text{Ti}_2\text{O}_7$ arrange in the so-called spin ice phase where the existence of magnetic monopoles as quasiparticles have been postulated by Castelnovo et al. [Cas08]. In our neutron work we have presented to our knowledge the first direct evidence of Dirac strings.

Based on a thermodynamic field theory for the transport of heat in a dielectric and magnetic solid, the temperature responses obtained in various heat relaxation and thermal transport measurements on single crystalline $\text{Dy}_2\text{Ti}_2\text{O}_7$ has been analysed. We were able to present not only the specific heat $c(T_R, B)$ of the spin ice compound in the temperature range from 0.3 K to 30 K and in magnetic fields up to 1.5 T, but also for the first time to identify the different contributions of magnetic excitations and their corresponding relaxation times in the spin ice phase. Moreover, the thermal conductivity and the related shortest relaxation time from phonon scattering were determined by thermodynamic analysis of steady state heat transport experiments. Finally, we were also able to reproduce the temperature profiles $\tilde{T}(x, t)$ recorded in heat pulse experiments on the basis of the thermodynamic field theory with the previous determined specific heat and thermal conductivity data without additional parameters. Thus, the thermodynamic field theory was proved to be thermodynamically consistent in describing three thermal transport experiments on different time scale, i. e. 10^{-3} s ... 10^3 s. The observed temperature and field dependencies of specific heat contributions and relaxation times indicate the magnetic excitations (α -, β -

and γ -excitations) in the spin ice as thermally activated monopole-antimonopole defects.

These results provide compelling evidence for dissociation of north and south magnetic poles – the splitting of the dipole – and the identification of spin ice as the first fractionalized magnet in three dimensions. The emergence of such striking states is profoundly important in physics both as a manifestation of new and singular properties of matter and routes to potential technologies. Examples of fractionalization are extremely rare and nearly all confined to one and two dimensions, and so the three dimensional pyrochlore lattice provides us with a promising new direction for future exploration both in magnets and exotic metals [Ful02; Bal10]. Our findings are of relevance not only from a fundamental physics aspect – we have evidenced a new set of quasiparticles which have no elementary cousins – but also because it initiates the study of a new type of degree of freedom in magnetism, namely an object with both local (point-like monopole) and extended (tensionless Dirac string) properties. $\text{Dy}_2\text{Ti}_2\text{O}_7$ is an exceptionally clean material, and with the full array of powerful experimental techniques and pulsed fields, equilibrium and non-equilibrium properties can be comprehensively addressed which will present a substantial statistical physics and dynamical systems challenge. This may throw light on other systems where string like objects can appear – for instance in the study of polymers or nanoclusters – but where freezing of solvents and inhomogeneities can restrict access to all the physics. Spin ice then is a remarkable material which promises to open up new and complementary insights on both emergence of fractionalized states and the physics of ensembles of strings in and out of equilibrium.

Bibliography

- [Ash05] N. W. Ashcroft and N. D. Mermin. *Festkörperphysik*. 2nd edition. Oldenbourg Verlag, München, 2005.
- [Bal10] L. Balents. “Spin liquids in frustrated magnets”. *Nature*, **464**, 199 (2010). DOI: doi:10.1038/nature08917.
- [Ber33] J. D. Bernal and R. H. Fowler. “A Theory of Water and Ionic Solution, with Particular Reference to Hydrogen and Hydroxyl Ions”. *Journal of Chemical Physics*, **1**(8), 515 (1933). DOI: 10.1063/1.1749327.
- [Bra01a] S. T. Bramwell, M. J. Harris, B. C. den Hertog, M. J. P. Gingras, J. S. Gardner, D. F. McMorrow, A. R. Wildes, A. L. Cornelius, J. D. M. Champion, R. G. Melko, and T. Fennell. “Spin Correlations in $\text{Ho}_2\text{Ti}_2\text{O}_7$: A Dipolar Spin Ice System”. *Physical Review Letters*, **87**(4), 047205 (2001). DOI: 10.1103/PhysRevLett.87.047205.
- [Bra01b] S. T. Bramwell and M. J. P. Gingras. “Spin Ice State in Frustrated Magnetic Pyrochlore Materials”. *Science*, **294**(5546), 1495 (2001). DOI: 10.1126/science.1064761.
- [Bra04] S. T. Bramwell, M. J. P. Gingras, and P. C. W. Holdsworth. *Frustrated spin systems*. Edited by H. T. Diep. Singapore: World Scientific, 2004, 367.
- [Bra09] S. T. Bramwell, S. R. Giblin, S. Calder, R. Aldus, D. Prabhakaran, and T. Fennell. “Measurement of the charge and current of magnetic monopoles in spin ice”. *Nature*, **461**(7266), 956–959 (2009). DOI: 10.1038/nature08500.
- [Bue42] M. J. Buerger. *X-ray crystallography*. Wiley, New York, 1942.
- [Cab82] B. Cabrera. “First Results from a Superconductive Detector for Moving Magnetic Monopoles”. *Physical Review Letters*, **48**(20), 1378 (1982). DOI: 10.1103/PhysRevLett.48.1378.

- [Cal59] J. Callaway. “Model for Lattice Thermal Conductivity at Low Temperatures”. *Physical Review*, **113**(4), 1046 (1959). DOI: 10.1103/PhysRev.113.1046.
- [Can01] B. Canals and D. A. Garanin. “Spin-liquid phase in the pyrochlore anti-ferromagnet”. *Canadian Journal of Physics*, **79**(11-12), 1323 (2001). DOI: 10.1139/cjp-79-11-12-1323.
- [Car59] H. S. Carslaw and J. C. Jaeger. *Conduction of heat in solids*. 2. ed. Oxford: Clarendon Press, 1959, 276 Equ. 10.10.V.
- [Cas08] C. Castelnovo, R. Moessner, and S. L. Sondhi. “Magnetic monopoles in spin ice”. *Nature*, **451**, 42 (2008). DOI: 10.1038/nature06433.
- [Cas09] C. Castelnovo, R. Moessner, and S. L. Sondhi. “Monopole density and specific heat from Monte Carlo simulations and Debye-Hückel calculations”. *unpublished*, (2009).
- [Cha00] P. M. Chaikin and T. C. Lubensky. *Principles of Condensed Matter Physics*. ISBN: 0 521 43224 3. Cambridge University Press, 2000.
- [Czt08] C. Czternasty. *Thermische und magnetische Untersuchungen an kristallinem Spin-Eis $Dy_2Ti_2O_7$ bei tiefen Temperaturen*. Diplomarbeit, Technische Universität Berlin (2008). 2008.
- [Dir31] P. A. M. Dirac. “Quantised Singularities in the Electromagnetic Field”. *Proceedings of the Royal Society of London. Series A. Mathematical and Physical Sciences*, **133**(821), 60 (1931). DOI: 10.1098/rspa.1931.0130.
- [Ebe71] P. H. Eberhard, R. R. Ross, L. W. Alvarez, and R. D. Watt. “Search for Magnetic Monopoles in Lunar Material”. *Physical Review D: Particles and Fields*, **4**(11), 3260 (1971). DOI: 10.1103/PhysRevD.4.3260.
- [Fen02] T. Fennell, O. A. Petrenko, G. Balakrishnan, S. T. Bramwell, J. D. M. Champion, B. Fåk, M. J. Harris, and D. M. Paul. “Field-induced partial order in the spin ice dysprosium titanate”. *Applied Physics A: Materials Science & Processing*, **74**(Part 1 Suppl. S), S889 (2002). DOI: 10.1007/s003390201638.

- [Fen04] T. Fennell, O. A. Petrenko, B. Fåk, S. T. Bramwell, M. Enjalran, T. Yavors’kii, M. J. P. Gingras, R. G. Melko, and G. Balakrishnan. “Neutron scattering investigation of the spin ice state in $\text{Dy}_2\text{Ti}_2\text{O}_7$ ”. *Physical Review B: Condensed Matter and Materials Physics*, **70**(13), 134408 (2004). DOI: 10.1103/PhysRevB.70.134408.
- [Fen05] T. Fennell, O. A. Petrenko, B. Fåk, J. S. Gardner, S. T. Bramwell, and B. Ouladdiaf. “Neutron scattering studies of the spin ices $\text{Ho}_2\text{Ti}_2\text{O}_7$ and $\text{Dy}_2\text{Ti}_2\text{O}_7$ in applied magnetic field”. *Physical Review B: Condensed Matter and Materials Physics*, **72**(22), 224411 (2005). DOI: 10.1103/PhysRevB.72.224411.
- [Fen07] T. Fennell, S. T. Bramwell, D. F. McMorrow, P. Manuel, and A. R. Wildes. “Pinch points and Kasteleyn transitions in kagome ice”. *Nature Physics*, **3**, 566 (2007). DOI: 10.1038/nphys632.
- [Fen09] T. Fennell, P. P. Deen, A. R. Wildes, K. Schmalzl, D. Prabhakaran, A. T. Boothroyd, R. J. Aldus, D. F. McMorrow, and S. T. Bramwell. “Magnetic Coulomb Phase in the Spin Ice $\text{Ho}_2\text{Ti}_2\text{O}_7$ ”. *Science*, **326**(5951), 415 (2009). DOI: 10.1126/science.1177582.
- [Fle69] R. L. Fleischer, H. R. Hart, I. S. Jacobs, P. B. Price, W. M. Schwarz, and F. Aumento. “Search for Magnetic Monopoles in Deep Ocean Deposits”. *Physical Review*, **184**(5), 1393 (1969). DOI: 10.1103/PhysRev.184.1393.
- [Ful02] P. Fulde, K. Penc, and N. Shannon. “Fractional charges in pyrochlore lattices”. *Annalen der Physik (Leipzig)*, **11**(12), 892 (2002). DOI: 10.1002/1521-3889(200212)11:12<892::AID-ANDP892>3.0.CO.
- [Got58] E. Goto. “On the Observation of Magnetic Poles”. *Journal of the Physical Society of Japan*, **13**, 1413 (1958). DOI: 10.1143/JPSJ.13.1413.
- [Gri08] Crystal grown by S. A. Grigera and R. S. Perry. *isotopically enriched $\text{Dy}_2\text{Ti}_2\text{O}_7$ single crystal (with 95%-98% ^{162}Dy)*. 2008.
- [Har97] M. J. Harris, S. T. Bramwell, D. F. McMorrow, T. Zeiske, and K. W. Godfrey. “Geometrical Frustration in the Ferromagnetic Pyrochlore $\text{Ho}_2\text{Ti}_2\text{O}_7$ ”. *Physical Review Letters*, **79**(13), 2554 (1997). DOI: 10.1103/PhysRevLett.79.2554.

- [Har98] M. J. Harris, S. T. Bramwell, P. C. W. Holdsworth, and J. D. M. Champion. “Liquid-Gas Critical Behavior in a Frustrated Pyrochlore Ferromagnet”. *Physical Review Letters*, **81**(20), 4496 (1998). DOI: 10.1103/PhysRevLett.81.4496.
- [Hig02] R. Higashinaka, H. Fukazawa, D. Yanagishima, and Y. Maeno. “Specific heat of $\text{Dy}_2\text{Ti}_2\text{O}_7$ in magnetic fields: comparison between single-crystalline and polycrystalline data”. *Journal of Physics and Chemistry of Solids*, **63**(6-8), 1043 (2002). DOI: 10.1016/S0022-3697(02)00065-3.
- [Hig03] R. Higashinaka, H. Fukazawa, and Y. Maeno. “Anisotropic release of the residual zero-point entropy in the spin ice compound $\text{Dy}_2\text{Ti}_2\text{O}_7$: Kagome ice behavior”. *Physical Review B: Condensed Matter and Materials Physics*, **68**(1), 014415 (2003). DOI: 10.1103/PhysRevB.68.014415.
- [Hir03] Z. Hiroi, K. Matsuhira, and M. Ogata. “Ferromagnetic Ising Spin Chains Emerging from the Spin Ice under Magnetic Field”. *Journal of the Physical Society of Japan*, **72**, 3045 (2003). DOI: 10.1143/JPSJ.72.3045.
- [Hof10] J.-U. Hoffmann. *privat communication* (2010).
- [Hwa97] J. S. Hwang, K. J. Lin, and C. Tien. “Measurement of heat capacity by fitting the whole temperature response of a heat-pulse calorimeter”. *Review of Scientific Instruments*, **68**, 94 (1997). DOI: 10.1063/1.1147722.
- [Isa04] S. V. Isakov, K. Gregor, R. Moessner, and S. L. Sondhi. “Dipolar Spin Correlations in Classical Pyrochlore Magnets”. *Physical Review Letters*, **93**(16), 167204 (2004). DOI: 10.1103/PhysRevLett.93.167204.
- [Isa05] S. V. Isakov, R. Moessner, and S. L. Sondhi. “Why Spin Ice Obeys the Ice Rules”. *Physical Review Letters*, **95**(21), 217201 (2005). DOI: 10.1103/PhysRevLett.95.217201.
- [Jau08] L. D. C. Jaubert, J. T. Chalker, P. C. W. Holdsworth, and R. Moessner. “Three-Dimensional Kasteleyn Transition: Spin Ice in a [100] Field”. *Physical Review Letters*, **100**(6), 067207 (2008). DOI: 10.1103/PhysRevLett.100.067207.
- [Jau09a] L. D. C. Jaubert and P. C. W. Holdsworth. “Signature of magnetic monopole and Dirac string dynamics in spin ice”. *Nature Physics*, **5**(4), 258 (2009). DOI: 10.1038/NPHYS1227.

- [Jau09b] L. D. C. Jaubert, J. T. Chalker, P. C. W. Holdsworth, and R. Moessner. “The Kasteleyn transition in three dimensions: Spin ice in a [100] field”. *Journal of Physics: Conference Series*, **145**(1), 012024 (2009). DOI: 10.1088/1742-6596/145/1/012024.
- [Kad09] H. Kadowaki, N. Doi, Y. Aoki, Y. Tabata, T. J. Sato, J. W. Lynn, K. Matsuhira, and Z. Hiroi. “Observation of Magnetic Monopoles in Spin Ice”. *Journal of the Physical Society of Japan*, **78**(10), 103706 (2009). DOI: 10.1143/JPSJ.78.103706.
- [Kie04] K. Kiefer. *Kalorimetrische und magnetische Untersuchungen am Spin-Peierls-System CuGeO_3* . Dissertation (Universität des Saarlandes, 2004). 2004.
- [Kob02] V. Kobelev, A. B. Kolomeisky, and M. E. Fisher. “Lattice models of ionic systems”. *Journal of Chemical Physics*, **116**(17), 7589 (2002). DOI: 10.1063/1.1464827.
- [Kov86] J. M. Kovalik and J. L. Kirschvink. “New superconducting-quantum-interference-device-based constraints on the abundance of magnetic monopoles trapped in matter: An investigation of deeply buried rocks”. *Physical Review A: Atomic, Molecular, and Optical Physics*, **33**(2), 1183 (1986). DOI: 10.1103/PhysRevA.33.1183.
- [Kru73] R. Krueger, M. Meißner, J. Mimkes, and A. Tausend. “Specific heat measurements of trigonal and vitreous selenium between 3 and 300 K by a heat pulse method”. *Physica Status Solidi A: Applications and Materials Science*, **17**(2), 471 (1973). DOI: 10.1002/pssa.2210170210.
- [Laka] Lake Shore Cryotronics, Inc. <http://www.lakeshore.com/temp/acc/am.html>.
- [Lakb] Lake Shore Cryotronics, Inc. <http://www.lakeshore.com/temp/sen/crtdts.html>.
- [Lev02] Y. Levin. “Electrostatic correlations: from plasma to biology”. *Reports on Progress in Physics*, **65**(11), 1577 (2002). DOI: 10.1088/0034-4885/65/11/201.
- [Mat02] K. Matsuhira, Z. Hiroi, T. Tayama, S. Takagi, and T. Sakakibara. “A new macroscopically degenerate ground state in the spin ice compound $\text{Dy}_2\text{Ti}_2\text{O}_7$ under a magnetic field”. *Journal of Physics: Condensed Matter*, **14**(29), L559 (2002). DOI: 10.1088/0953-8984/14/29/L059.

- [Mei00] M. Meißner. *Usage of Sample Environment at BENSC, Technical Handbook*. Helmholtz-Zentrum Berlin. June 2000.
- [Mei04] M. Meißner and P. Strehlow. “Low Temperature Heat Capacity of High Purity Silica Glasses in Magnetic Field”. *Journal of Low Temperature Physics*, **137**, 355 (2004). DOI: 10.1023/B:JOLT.0000049062.85203.82.
- [Mei96] M. Meißner, N. Sampat, and P. Strehlow. “Wave-like and diffusive heat transport in a-SiO₂ below 1 K”. *Physica B: Condensed Matter*, **219-220**, 302 (1996). DOI: DOI:10.1016/0921-4526(95)00727-X.
- [Mel04] R. G. Melko and M. J. P. Gingras. “Monte Carlo studies of the dipolar spin ice model”. *Journal of Physics: Condensed Matter*, **16**(43), R1277 (2004). DOI: 10.1088/0953-8984/16/43/R02.
- [Mor09] D. J. P. Morris, D. A. Tennant, S. A. Grigera, B. Klemke, C. Castelnovo, R. Moessner, C. Czternasty, M. Meissner, K. C. Rule, J.-U. Hoffmann, K. Kiefer, S. Gerischer, D. Slobinsky, and R. S. Perry. “Dirac Strings and Magnetic Monopoles in the Spin Ice Dy₂Ti₂O₇”. *Science*, **326**, 411 (2009). DOI: 10.1126/science.1178868.
- [Neu10] S. Neubert. *Zur thermodynamischen Beschreibung des Wärmetransports im Spin-Eis Dy₂Ti₂O₇*. Diplomarbeit, Technische Universität Berlin (2010). 2010.
- [Ons34] L. Onsager. “Deviations from Ohm’s Law in Weak Electrolytes”. *Journal of Chemical Physics*, **2**(9), 599 (1934). DOI: 10.1063/1.1749541.
- [Orb61] R. Orbach. “Spin-Lattice Relaxation in Rare-Earth Salts”. *Proceedings of the Royal Society of London. Series A. Mathematical and Physical Sciences*, **264**(1319), 458 (1961). DOI: 10.1098/rspa.1961.0211.
- [Ore07] M. Orendáč, J. Hanko, E. Čížmár, A. Orendáčová, M. Shirai, and S. T. Bramwell. “Magnetocaloric study of spin relaxation in dipolar spin ice Dy₂Ti₂O₇”. *Physical Review B: Condensed Matter and Materials Physics*, **75**(10), 104425 (2007). DOI: 10.1103/PhysRevB.75.104425.
- [Oxf] Oxford Instruments plc. <http://www.oxford-instruments.com/products/low-temperature/3he-refrigerators/helioxvl/Pages/helioxvl.aspx>. HelioxVL.

- [Pau35] L. Pauling. “The Structure and Entropy of Ice and of Other Crystals with Some Randomness of Atomic Arrangement”. *Journal of the American Chemical Society*, **57**(12), 2680 (1935). DOI: 10.1021/ja01315a102.
- [Poh82] R. O. Pohl and B. Stritzker. “Phonon scattering at crystal surfaces”. *Physical Review B: Condensed Matter and Materials Physics*, **25**(6), 3608 (1982). DOI: 10.1103/PhysRevB.25.3608.
- [Ram99] A. P. Ramirez, A. Hayashi, R. J. Cava, R. Siddharthan, and B. S. Shastri. “Zero-point entropy in ‘spin ice’”. *Nature*, **399**, 333 (1999). DOI: 10.1038/20619.
- [Ruf05] J. P. C. Ruff, R. G. Melko, and M. J. P. Gingras. “Finite-Temperature Transitions in Dipolar Spin Ice in a Large Magnetic Field”. *Physical Review Letters*, **95**(9), 097202 (2005). DOI: 10.1103/PhysRevLett.95.097202.
- [Ruf10] J. P. C. Ruff, Z. Islam, J. P. Clancy, K. A. Ross, H. Nojiri, Y. H. Matsuda, H. A. Dabkowska, A. D. Dabkowski, and B. D. Gaulin. “Magnetoelectrics of a Spin Liquid: X-Ray Diffraction Studies of $Tb_2Ti_2O_7$ in Pulsed Magnetic Fields”. *Physical Review Letters*, **105**(7), 077203 (2010). DOI: 10.1103/PhysRevLett.105.077203.
- [Sai05] M. Saito, R. Higashinaka, and Y. Maeno. “Magnetodielectric response of the spin-ice $Dy_2Ti_2O_7$ ”. *Physical Review B: Condensed Matter and Materials Physics*, **72**(14), 144422 (2005). DOI: 10.1103/PhysRevB.72.144422.
- [Sak03] T. Sakakibara, T. Tayama, Z. Hiroi, K. Matsuhira, and S. Takagi. “Observation of a liquid-gas-type Transition in the pyrochlore spin ice compound $Dy_2Ti_2O_7$ in a magnetic field”. *Physical Review Letters*, **90**(20), 207205 (2003). DOI: 10.1103/PhysRevLett.90.207205.
- [She85] J. P. Shepherd. “Analysis of the lumped τ_2 effect in relaxation calorimetry”. *Review of Scientific Instruments*, **56**, 273 (1985). DOI: 10.1063/1.1138343.
- [Sny01] J. Snyder, J. S. Slusky, R. J. Cava, and P. Schiffer. “How ‘spin ice’ freezes”. *Nature*, **413**, 48 (2001). DOI: 10.1038/35092516.
- [Sny04] J. Snyder, B. G. Ueland, J. S. Slusky, H. Karunadasa, R. J. Cava, and P. Schiffer. “Low-temperature spin freezing in the $Dy_2Ti_2O_7$ spin ice”. *Physical Review B: Condensed Matter and Materials Physics*, **69**(6), 064414 (2004). DOI: 10.1103/PhysRevB.69.064414.

- [Str94] P. Strehlow and W. Dreyer. “Heat propagation in glasses”. *Physica B: Condensed Matter*, **194-196**(Part 1), 485 (1994). DOI: DOI:10.1016/0921-4526(94)90572-X.
- [Str97] P. Strehlow. *Habilitationsschrift: Quantenthermodynamik von Gläsern*. Fachbereich Thermodynamik, Technische Universität Berlin (1997). 1997.
- [Tas65] L. Tassie. “Dirac magnetic monopoles and superconductivity”. *Il Nuovo Cimento (1955-1965)*, **38**, 1935 (1965). DOI: 10.1007/BF02750116.
- [Uem10] Y. J. Uemura. “Did μ SR detect magnetic monopoles in spin ice?” In: *Meeting of Advanced Working Group on Monopoles in Spin Ice*, Royal Holloway, University of London. October 2010.
- [VH68] L. L. Vant-Hull. “Experimental Upper Limit on the Magnetic Monopole Moment of Electrons, Protons, and Neutrons, Utilizing a Superconducting Quantum Interferometer”. *Physical Review*, **173**(5), 1412 (1968). DOI: 10.1103/PhysRev.173.1412.
- [Wie07] C. Wiebe and H. Zhou. “Persistent spin dynamics in ‘stuffed’ spin ice”. *Mag Lab Reports*, **14**(4), 4 (2007).
- [Yav08] T. Yavors’kii, T. Fennell, M. J. P. Gingras, and S. T. Bramwell. “ $\text{Dy}_2\text{Ti}_2\text{O}_7$ Spin Ice: A Test Case for Emergent Clusters in a Frustrated Magnet”. *Physical Review Letters*, **101**(3), 037204 (2008). DOI: 10.1103/PhysRevLett.101.037204.
- [Yos04] S.-i. Yoshida, K. Nemoto, and K. Wada. “Ordered Phase of Dipolar Spin Ice under [110] Magnetic Field”. *Journal of the Physical Society of Japan*, **73**, 1619 (2004). DOI: 10.1143/JPSJ.73.1619.
- [Zim72] J. M. Ziman. *Principles of the Theory of Solids*. 2nd edition. Cambridge University Press, 1972, p353.

List of Figures

1.1	Specific heat of $\text{Dy}_2\text{Ti}_2\text{O}_7$ in the spin ice state ($B = 0$ T)	4
2.1	Example for frustrated lattices	8
2.2	Equivalence of water ice and spin ice	9
2.3	$\text{Dy}_2\text{Ti}_2\text{O}_7$ pyrochlore lattice	10
2.4	Different orientations of $\text{Dy}_2\text{Ti}_2\text{O}_7$ crystal	11
2.5	Specific heat and entropy at 0 T	13
2.6	Candidate monopole event	15
2.7	Magnetic monopoles: spin and dumbbell picture	16
2.8	Pair of separated monopoles	17
2.9	Pyrochlore lattice with separated magnetic monopoles ($B \parallel [001]$)	19
2.10	Magnetization with magnetic field applied along $[001]$	21
3.1	Instrument picture of the E2 flat cone diffractometer	23
3.2	Cryomagnet VM-4	24
3.3	Pinch-point in E2 neutron diffraction data	25
3.4	Dipolar correlations in reciprocal space of spin ice at 0.7 K	26
3.5	Kasteleyn transition field	27
3.6	Diffuse neutron scattering with field along the $[001]$ direction	28
3.7	Biased random walks in tilted field	29
3.8	Correlation length ξ_{ice}	32
3.9	Temperature dependence of the muon relaxation rate	33
3.10	Specific heat measured under $[111]$ magnetic field	34
4.1	Temperature increase in a relaxation type calorimeter	39
4.2	Typical temperature profile for glasses at low temperature	40
5.1	Schematic plot of α - and β -chains in the pyrochlore lattice	46

5.2	Magnetic field - temperature phase diagram for $B \parallel [110]$	47
5.3	Set-up of relaxation calorimeter used for heat capacity measurements . . .	49
5.4	Temperature profile at $T_R = 530$ mK	52
5.5	Temperature profiles below 1 K at 0 T	53
5.6	Specific heat for magnetic fields $B = 0 - 0.2$ T	55
5.7	Specific heat for magnetic fields $B = 0.5 - 1.5$ T	56
5.8	Heat capacity data (CM-14.5T)	57
5.9	Set-up for the thermal conductivity measurements	59
5.10	Thermal conductivity (magnetic field and heat flow $\parallel [110]$ axis)	62
5.11	Temperature transients $\tilde{T}(x, t)$ for $T_R = 1.1$ K and $T_R = 0.37$ K	65
6.1	Magnetic heat capacity compared with theory	70
6.2	Specific heat $c_{m\alpha}$ of the α -excitations	72
6.3	Specific heat $c_{m\beta}$ of the β -excitations for $B < 0.5$ T	74
6.4	Relaxation times of α - and β -excitations for $B = 0$ T	76
6.5	Relaxation times of α - and β -excitations for $B = 0$ T and 0.2 T	78
6.6	Specific heat $c_{m\gamma}$ of the γ -excitations for $B < 0.5$ T	81
6.7	Specific heat $c_{m\beta}$ and $c_{m\gamma}$ for $B \geq 0.5$ T	83
6.8	Thermal conductivity data compared with theoretical model	85
6.9	Relaxation time of γ -excitations derived from thermal conductivity data	88

List of Tables

5.1	Parameters used for standard diffusion heat transport model	66
6.1	Parameters used for specific heat model calculations for $c_{m\alpha}(T, B)$	73
6.2	Parameters used for specific heat model calculations for $c_{m\beta}(T, B)$	75
6.3	Parameters for relaxation times τ_{α}^R and τ_{β}^R	79
6.4	Parameters used for specific heat model calculations for $c_{m\gamma}(T)$	82
6.5	Parameters used for specific heat model calculations for $B \geq 0.5$ T	84
6.6	Parameters for resistive scattering processes	87
6.7	Parameters for relaxation time τ_{γ}^R ($T < 1$ K)	89
6.8	Parameters for relaxation time τ_{γ}^R ($T > 1.4$ K)	89

Acknowledgement

Foremost, I would like to express my sincere gratitude to my supervisor Prof. Dr. Alan Tennant for the continuous support of my doctoral thesis and the possibility to perform my thesis at the Helmholtz-Zentrum Berlin.

I am deeply grateful to my supervisor, Prof. Dr. Michael Meißner for his patience, motivation, enthusiasm and immense knowledge. His guidance helped me in all the time of research and writing of this thesis.

I owe my most sincere gratitude to Prof. Dr. Peter Strehlow, PTB Berlin, who initiated me into the mysteries of advanced thermodynamics and devised the thermodynamic field theory.

I warmly thank Dr. Klaus Kiefer for his valuable advice and friendly help. His extensive discussions around my work and interesting explorations into analogue and digital electronics have been very helpful for this study.

I would like to thank Dr. Jonatan Morris, Hanjo Ryll and Clemens Czternasty for fruitful discussions and a lot of experimental help.

During this work I have collaborated with many colleagues for whom I have great regard, and I wish to extend my warmest thanks to all those who have helped me with my work. Especially, I would like to thank the whole team of the *Sample Environment Group* at the Helmholtz-Zentrum Berlin, which gave me great support.

I owe my loving thanks to Susanna and my family. Without their encouragement and understanding it would have been impossible for me to finish this work.